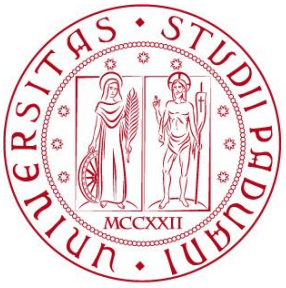

UNIVERSITÀ DEGLI STUDI DI PADOVA

UNIVERSITY OF PADOVA
Department of Management and Engineering

Doctoral School in Mechatronics and Product Innovation Engineering
XXXI CYCLE

PERFORMANCE EVALUATION AND SAFETY IMPROVEMENT OF CABLE DRIVEN ROBOTS

A dissertation submitted in partial fulfillment of the requirements for the degree of Doctor of Philosophy in Mechatronics and Product Innovation Engineering

Supervisor : Prof. Giovanni Boschetti

Ph.D. Candidate: CHIARA PASSARINI

To my Family

Families are the compass that guides us. They are the inspiration to reach great heights, and our comfort when we occasionally falter

— Brad Henry

ABSTRACT

Cable Driven Robots are a new class of parallel manipulators in which rigid links are replaced by cables. They are widely suggested for applications involving wide workspaces and high payloads. Moreover, their simple and light design makes them inexpensive and reconfigurable. However, besides all these advantages, only few examples of successful applications are present outside research laboratories. The most well known one is the cable suspended camera system in stadiums and arenas. Even if these devices are widely employed in public and crowded areas, close to or even in contact with humans, an emergency stop in case of failure or cable breakage is not yet available. Indeed, managing safety in cable driven robots is more difficult than in conventional manipulators with rigid links. In particular, an abrupt brake of the actuated joints is not a sufficient condition to ensure the arrest of the end effector.

The objective of this thesis is to investigate safety issues in cable driven robots and propose recovery approaches to apply in case of failure. The need of safety is proven by many examples of malfunctions or accidents involving cable camera systems around the world. By studying the performance of cable driven robots before and after failure, new algorithms are proposed to deal with cable breakage and keep the end effector under control in emergency conditions.

The first part of the thesis presents an overview of cable driven robots, including classification, modeling and performance evaluation. The second part focuses on after failure recovery approaches. Two different strategies are proposed to lead the end effector towards a safe configuration following a feasible path and avoiding further damages. The proposed strategies are tested on a real prototype to prove their effectiveness and the experimental results are discussed in the last part of this dissertation.

Keywords: Cable Driven Robots, motion planning, safety, performance evaluation, failure, emergency stop

SOMMARIO

I robot a cavi sono una classe di manipolatori innovativa nell'ambito della robotica. Risultano particolarmente vantaggiosi nei campi in cui si richiede un ampio spazio di lavoro o la capacità di sollevare carichi ingenti. Il loro design semplice e leggero li rende notevolmente economici e facilmente riconfigurabili. Nonostante gli innegabili vantaggi, i robot a cavi sono ancora scarsamente diffusi in applicazioni che esulano dalla ricerca. L'applicazione più nota e di maggior successo è probabilmente quella delle telecamere sospese, impiegate in stadi e palazzetti. Nonostante l'uso intensivo di questa tecnologia in aree pubbliche ed affollate, non è ancora presente un efficiente sistema di emergenza. Infatti, un improvviso blocco dei motori non assicura l'arresto del dispositivo, come invece accade per i robot tradizionali a membri rigidi.

Lo scopo di questa tesi è quello di analizzare le problematiche legate alla sicurezza nei robot a cavi e proporre nuove soluzioni da attuare in caso di malfunzionamento per assicurare l'arresto dell'organo terminale. La necessità di un'efficiente strategia per gestire i guasti è provata dai numerosi incidenti riguardanti le telecamere sospese avvenuti in tutto il mondo.

La prima parte della tesi presenta una panoramica sui robot a cavi, considerando classificazione, modellazione e valutazione delle prestazioni. Successivamente, la tesi presenta due diverse possibili strategie da attuare in caso di rottura di uno o più cavi per garantire l'arresto in sicurezza dell'organo terminale mentendo la tensione su tutti i cavi rimanenti. Le strategie verrano quindi testate considerando un prototipo di robot a cavi sospeso e planare. Seguiranno poi i risultati sperimentali nella parte finale della tesi dove verranno discusse fattibilità ed affidabilità di entrambe le strategie.

CONTENTS

1 INTRODUCTION

Robotics is in continuous improvement and new challenges arise every day. Robots are widely present in our lives, not only in industries but also in domestic environments and services. The search of more efficient structures led to the introduction of parallel robots in opposition with the heavy structure of serial ones.

Nowadays, researches continues to look for cheaper/more efficient and flexible solutions. Under this lead, cable robots have been proposed as a promising alternative to classic parallel robots. Cable Driven Parallel Robots (CDPRs) are indeed a special class of parallel manipulators in which rigid links are replaced by cables. Each cable is wound around an actuated pulley that extends or retracts the cable to manipulate the end effector. A schematic representation is shown in Fig.1.1

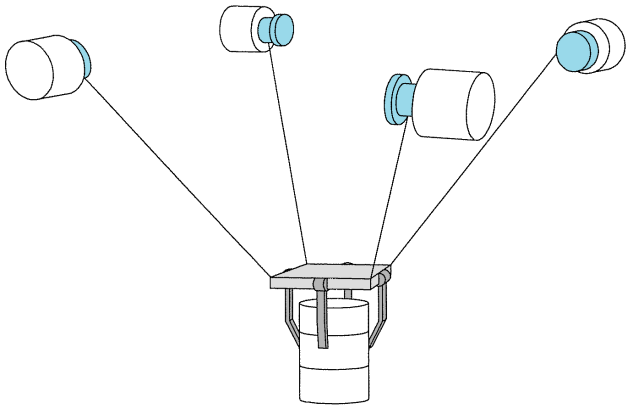

Figure 1.1: Schematic representation of a generic cable robot

This design introduces several advantages over conventional parallel robots, such as:

- wide workspace: by simply lengthening the cables, it is possible to cover a very large area with a very low investment increase. Hence, they are suitable for big structures such as ships, hangars, harbors and stadiums.
- high payload ratio, comparable to the one of construction cranes.
- low moving masses: in contrast with conventional cable robots, the structure is significantly lighter and can be considered negligible if compared to the actual load.

- high speed motions: thanks to their light design, the involved inertia is significantly reduced and hence the robot can reach higher speeds and accelerations.
- economically efficient: thanks to their simple design both at the design and maintenance stage, cable robots represents an inexpensive investment.
- transportable and reconfigurable: the light and simple design makes it easy to move the robot between difference locations and to adapt the structure by adding/removing cable pretty easily.

Pioneers applications on such mechanisms are are the National Institute of Standards and Technology (NIST) Robocrane [3] and the Skycam [21], shown in Fig. 1.2 and 1.3 respectively.

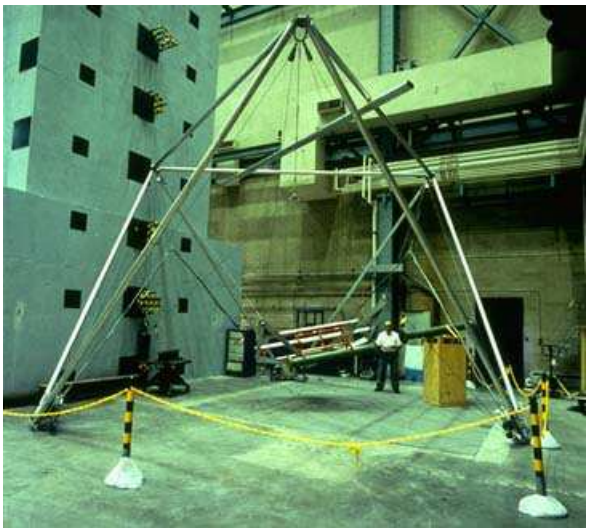

Figure 1.2: NIST robocrane prototype

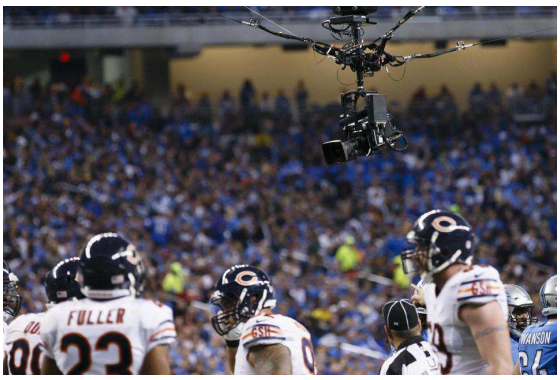

Figure 1.3: Cable Camera in action during a football field

Thanks to their promising advantages, further prototypes investigated other possible implementations in different fields such as in-

dustrial applications [4, 52], and rehabilitation [55, 60, 68]. Fig. 1.4 shows the IPAnema cable robot for fast pick and place operations developed at Fraunhofer Institute of Technology.

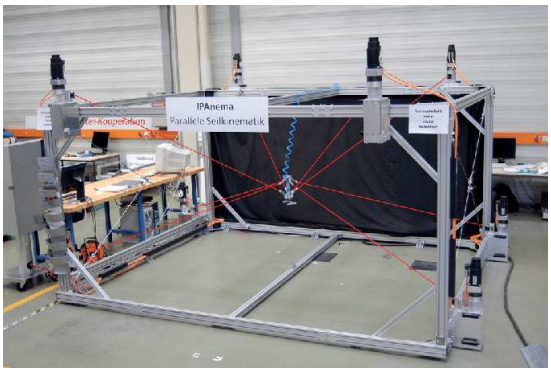

Figure 1.4: IPAnema prototype at Fraunhofer Insitute of Technology

Cable robots have been widely suggested for rehabilitation purposes. NeReBot (NEuro REhabilitation roBOT) [24] is a cable-suspended device for upper limb rehabilitation of post-stroke patients and was developed at Padova University (Fig. 1.5). This device was designed to target post-stroke patients in a very early stage (a few days after the stroke) and can be operated both at bed side or with wheelchaired patients. Three nylon wires convert the rotating motion of three motors into a 3D trajectory of patient's arm. A real-time software performs both on-line point by point acquisition and repetition of the 3D trajectory obtained by interpolating the acquired points. The evolution of NeReBot is MariBot (MARIsa roBOT), a 5 DOF cable-suspended robot for neurorehabilitation [58]. This robot is designed for post-stroke upper limb rehabilitation in the post-acute phase. Three nylon wires are used to sustain the forearm of the patient and produce motion in the vertical plane, while two additional actuators move the overhead structure to adjust the cable configuration in the horizontal plane.

Figure 1.5: NeReBot prototype at Padova University for upper arm rehabilitation

More recently, researchers at Columbia university presented the prototype of a novel tethered pelvic assist device (T-PAD) [65] that consists of springs and cables (Fig. 1.6). Thanks to the ability of applying force in any direction, T-PAD provides pelvic support and in addition its tethers can also be configured to apply asymmetric forces on the pelvis. An evolution of such device can be found in C-ALEX [38] (Fig.1.7) which employs the "assist-as-needed" control strategy to help the ankle center move along a prescribed path.

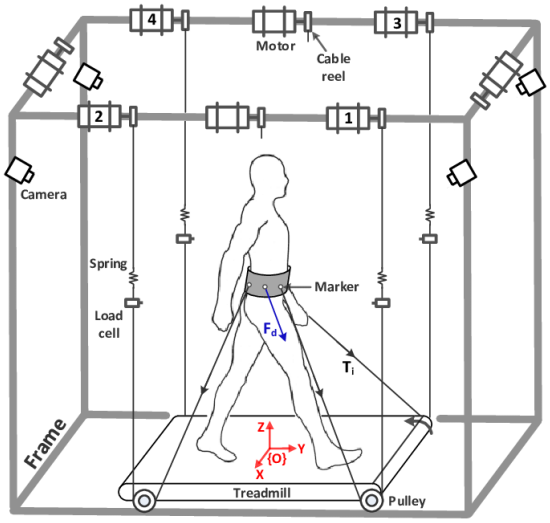

Figure 1.6: Design of T-PAD prototype at Columbia University

Finally, at University of Cassino and Southern Lazio an assisting device for applications in human upper limb exercising and rehabilitation has been proposed [40]. The prototype called Lawex is shown in Fig.1.8: it is composed by a rigid structure and a mobile platform as end effector that guides the arm during the rehabilitation exercises.

Figure 1.7: Design of C-ALEX prototype at Columbia University

Figure 1.8: Lawex prototype at Cassino University

Cable robots have been proposed also in field involving heavy loads, such as the system proposed by Holland and Cannon [34]. It represents the first patented suspended cable robot system for precisely manipulate shipping containers over large workspaces (Fig. 1.9).

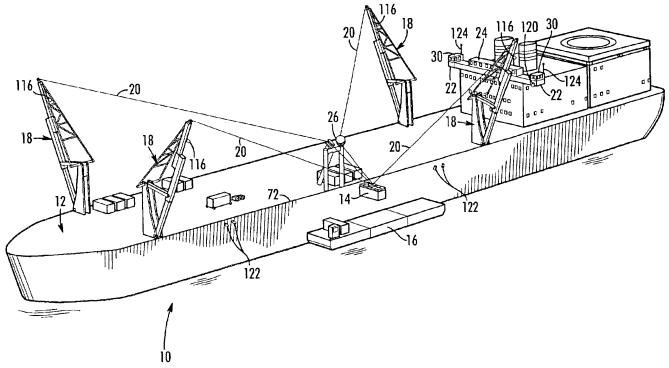

Figure 1.9: Cable robot for container shipping

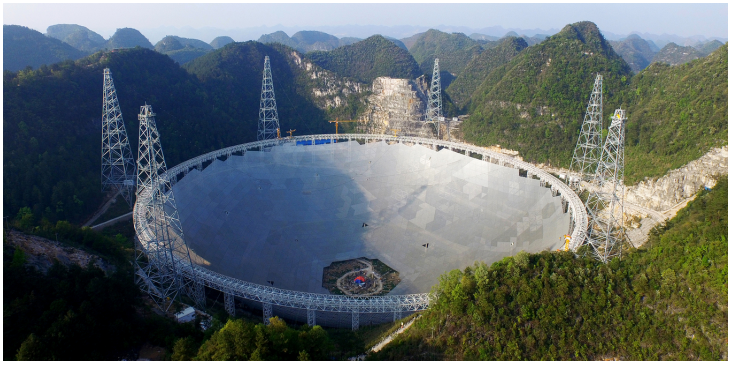

Figure 1.10: FAST telescope

Figure 1.11: Atlas

Other interesting application are exploiting the possibility of having large workspaces and payloads. An example is the so called FAST telescope [45] which is an unconstrained six-cable-suspended robot (Fig. 1.10). Another example is the prototype of fully-constrained CDPR proposed by Pott et.al [51] for a large-scale process like the assembly of parabolic reflector panels (Fig. 1.11)

1.1 STATE OF THE ART

All the reported applications are perfect examples of how cable robots are exploited in different fields thanks to their peculiar characteristics.

However, besides the undeniable advantages of these devices and all the promising prototypes, some trade-offs arise. Indeed, cables can only exert tensile forces and hence they can only pull and not push the end effector. Hence, they operates properly only when cable tensions are kept positive during the whole task execution. Such a constraint makes trajectory planning and motion control particularly challenging [62].

Several contributions proposed in literature have dealt with the issue developing control schemes [49, 64, 66] or trajectory planning strategies [7] able to ensure positive cable tension during the motion. Other approaches involve predicting the cable tensions in order to ensure a priori a feasible motion [54]. Such techniques rely on redundant cables or on the on-line solution of optimization problems to guarantee positive cable tensions. Both the approaches however have major limitations: given the higher number of wires and actuators, redundant CDDRs are often more difficult to design (due to possible cable-interference) and more expensive than non-redundant CDDRs. On the other hand, the on-line solution of optimization problems makes computation time a critical issue: processing time is generally much grater than motion time, which makes these approaches unsuitable for real time implementation.

An attempt to overcome these limitations, and to specifically deal with the peculiar bilateral tensile cable force constraints (i.e. slackness and excessive tension in cables), can be found in [62]. In such work, an off-line trajectory planning method addressing underconstrained translational planar cable robots is presented to ensure a-priori positive and bounded cable tensions.

Recent studies have investigated motion planning strategies for CDPRs that enable feasible trajectories that extend beyond a device's workspace. A dynamic trajectory planning approach for a planar cable-suspended robot with point-mass end-effector was proposed in [31] and extended to a spatial robot in [29]. This methodology takes into account the cable tensions constraints at the trajectory planning stage by substituting continuous periodic Cartesian trajectories into cable constraints. Global conditions are then obtained to ensure that positive tensions are maintained in all cables along those trajectories, without the need for time discretization. In [30], the same group studied point-to-point motions of a two-DoF cable-suspended robot. Both polynomial and trigonometric trajectories were investigated and a system of time-independent inequalities was proposed to derive feasible trajectories that extend beyond the *WCW*. The approach was extended to a planar three-DoF robot in [36] and to a spatial point-mass robot in [37]. In [23], the same authors further investigated static-to-dynamic transitions for two specific designs of planar and spatial point-mass cable-suspended robots, and in [44], they also proposed a new method to perform static-to-dynamic transitions to spatial elliptical trajectories, which they applied to a three-cable cable-suspended robot with point-mass end effector. An extension of this work was presented in [43], where the authors studied the feasible range of motion frequencies and the transitions between different periodic trajectories for spatial 3-DoF suspended manipulators.

The peculiar unilateral force exertion capability of cable robots introduce new issues when dealing with performance evaluation. Indeed, their performance are highly directional and pose dependent when compared to the one of a conventional parallel manipulator. This is a direct consequence of the fact that the actuated winches exertion forces are not symmetrical. It follows that performance indexes introduced in the past for parallel manipulators ar not straightforwardly applicable.

One peculiar highly pose dependent characteristic of a manipulator is the wrench capability, which is defined as the maximum force/moment that can be exerted on its moving platform. Such capability not only depends on the actual position of the end-effector, but it varies significantly with the direction of motion.

Several studies have been carried out to define and characterize the wrench capability of a parallel manipulator. In [46] the authors define the maximum force that an n-DoF manipulator can apply on the moving platform as the boundary of a polytope. Such polytope describes the available force set in the n-dimensional space. The force polytope was generated by computing the maximum force in any given direction with an optimization-based algorithm. Thereafter, many authors proposed several methods to define the available wrench set (i.e., the wrench polytope) for parallel manipulators. In [69] Zibil et al. proposed an explicit method based on scaling-factors to define the wrench polytope with improved accuracy and efficiency. Other studies that make use of the wrench polytope to describe the robot capabilities can be found in [25] and [26].

However, as introduced before, cables can only exert tensile forces and hence the minimum acceptable tension in each cable must be strictly positive. Local performance indexes based on the wrench polytope have been used in [56] in the context of adaptive cable-driven robots. The proposed method, which was formalized in [57] for a generic local index and experimentally validated in [68], allows designers to derive the optimal trajectories of the cable attachment points that guarantee a target level of the performance index within a given workspace.

In [18] a new method to define the wrench polytope of cable driven parallel manipulators was presented. Such method takes into account the unilateral force exertion capability of cables and proposes a non-iterative algorithm to obtain the *H-representation* of the polytope. In [22] the authors proposed a new method to identify vertexes, edges, and faces of the wrench polytope with the aim of exploring the relationship between the polytope and the cable robot structure. Moreover, convex analysis is exploited in [41] to perform the force-closure and workspace analysis of cable driven manipulators.

Another important open issue regarding cable driven robots is how to manage emergency situations due to failures. Indeed, managing safety in cable driven robots is more difficult than in conventional manipulators with rigid links. In such robots, for example, an abrupt emergency stop of the end effector can be obtained by dropping motor voltage and braking the actuated joints. This is usually enough to stop a traditional robots promptly but does not represent a strategy that can be used with cable robots: in particular braking motors is not a sufficient condition to make the end effector reach a static equilibrium configuration. Moreover, planning a recovery strategy is particularly challenging since all tensions has to be kept positive in order to maintain control over the manipulator. Additional challenges arise from the fact that the robot configuration might change due to a cable failure: for example an over constrained configuration could result in an fully contained one or the failure can cause a fully constrained configuration to become an under constrained one. In this case, not all the initial degrees of freedom of the end effector are controllable. Moreover, failure can cause a reduction of force exertion capabilities. As a consequence, the initially planned motion could be unfeasible; a tool to appraise the residual force exertion capability is required in order to plan a feasible motion after failure. Finally, the workspace may change and could be smaller if compared to the previous one. Hence, it can happen that, at the failure instant, the end effector lies outside the residual workspace. In case of failure, the objective would be to promptly drive the end effector inside the residual workspace.

In cable robots, failures may occur when one or more cables are slack or broken (zero tension), jammed (constant length) or are providing a different force (zero, contestant or limited) due to actuating mechanism malfunctions [47]. If the tensions of cables differ from the planned ones, unwanted wrenches are applied to the end effector, which may prevent controlling the manipulator. Moreover, the failure of a cable suddenly modifies the topology and consequently the workspace of a cable robot. In real scenarios, a cable breakage can always be detected, possibly with a small time delay, by taking advantage of the kinematic redundancy of the system. For example, a consistency check can be run on the different solutions of the forward kinematics, each obtained by neglecting one cable and computing the intersection of spheres centered on the attachment points of the remaining cables, each having a known radius given by the length of the corresponding cable.

Regardless of the application, the increasing need of direct interaction with humans [1, 57] makes safety a major concern and a primary research issue.The need for safety is also shown by the increased number of accidents in suspended camera applications. Cable-suspended camera systems represent one of the most common applications of

CDPRs in the market. Despite the widespread use of such devices in crowded public areas such as stadiums and arenas, the reliability of this kind of manipulator remains an issue [2]. In fact, no emergency stop strategy is currently available in these systems. The first significant failure of a Skycam camera occurred during a 2007 Sunday night NFL football game between New Orleans and Seattle, but the company reported that the camera followed a controlled descent to the field. Another accident took place during the Insight Bowl between Iowa and Oklahoma on December 30 2011, when the camera crashed into the field, almost hitting a player and forcing several others to crouch down. In 2013 another cable-based camera fell into the spectators during the Charlotte World 600, injuring ten fans, sending three people to the hospital and damaging several race cars. The most recent episode occurred during the the 2016 Olympic games in Rio de Janeiro when an overhead television camera suspended by cables crashed to the ground in the Olympic Park, injuring seven people. After the failure, the camera fell down from an height of approximately 20 meters. These examples prove that safety is a major concern for cable driven robots, especially for applications requiring close operations with human agents.

A very basic approach which can be followed at the design stage to improve safety in case of cable failure, consists in increasing the number of cables far beyond the minimum needed number. Indeed, cable robots with many degrees of redundancy can better cope with cable failures and in particular, with a broken cable. However, this approach has some major limitations: first of all, it is expensive, and additionally cables tend to obstruct the workspace and sometimes cable interference can be difficult to avoid. Therefore, it is interesting investigating how a cable robot should be moved to assure safety in case of cable failure, without introducing excessive cable redundancy.

Failures of cable driven robots were first investigated in [54] by studying how removing a cable from the robot effects its ability to achieve static equilibrium. In [16] different types of failures were classified with respect to the so called wrench-feasible workspace, dividing failures due to exceeding upper tension bounds, from failures due to slack cables (i.e. with tensions below the lower bound). In [47] classification of the possible failure modes is discussed and a methodology to recover the lost wrench is proposed in [48]. Finally, in [28] a preliminary evaluation of the failure consequences is presented. Such a work studies an optimal robot design minimizing the differences in cable tensions before and after failure.

1.2 AIM OF THE THESIS

The aim of this dissertation is to investigate two important aspects arising from the peculiar unilateral exertion capability of cable driven

robots: performance evaluation and safety improvement. The two topics are related because in order to plan a feasible after failure motion, it is important to appraise the residual capabilities of the manipulator immediately after failure. For this reason, the first part of this work deals with the analysis of a new approach to evaluate the force exertion capability of cable driven robots.

As previously introduced, performance indexes for classic parallel manipulator can not be applied straightforwardly to cable driven robots. In particular, a new approach for performance evaluation firstly presented in [13] is here deeper analyzed. Based on the computation of the maximum exertable force in a given direction, this approach can be applied to any redundant cable robot. Following that study, a novel index for cable robots called WEC (Wrench Exertion Capability) was presented in [14], and extended to underactuated cable robots. This index describes the maximum wrench that can be exerted along a given direction d while keeping null all the other wrench components.

In this dissertation, a novel geometry-based approach to compute the *WEC* index is presented for its implementation in real-time applications. Compared to iterative algorithms, geometry-based algorithms can generate the wrench polytope in a more efficient way. The importance of having efficient algorithms that can be implemented in real-time applications is also underlined in [10] and [42]. The new efficient method to compute the *WEC* index will be discussed in Chapter 3.

The second part focuses on improving safety for cable driven robots. Indeed, nowadays no emergency stop is available. In this work, two different approaches to deal with cable failure are proposed. The first one suggests a linear trajectory while the second approach involves periodic trajectories.

The first approach main focus is to lead the end effector to a safe configuration with a simple motion to be performed in a minimum time. However, usually a straight line path can not be planned immediately after failure; for this reason a connecting path is firstly performed to change the direction of motion of the end effector and make it point the desired safe location. This strategy exploits the usage of the already introduced *WEC* index to apprise the after failure performance of the cable robot in real-time and ensure a feasible path.

The second approach is based on periodic motions and takes advantages of planning approaches already proposed in literature by Gosselin et al. regarding trajectories extending beyond a device's workspace ([23, 31, 43]). Such trajectories are proven to be feasible for any amplitudes when a particular frequency of motion if chosen. In this work, taking advantage of the intrinsic feasibility of such trajectories, a new approach to lead the end effector towards a safe ending

location is proposed. The after failure trajectory is addressed in particular to suspended redundant cable robots.

Both approaches will be discussed in this work (Chapter 4 and 5). The main advantages and limitation of each approach will be investigated in order to understand in which field one approach is more suitable then the other and *vice-versa*.

2

CLASSIFICATION AND MATHEMATICAL MODELS

In this chapter cable driven robots are discussed more thoroughly. Firstly, a general classification is given with respect to the ratio between number of degrees of freedom and number of cables. Such classification highlights the characteristics of different configurations. Moreover, the kinematic and dynamic analysis of a generic cable robot is provided.

As already stated in Section 1, cable robots are parallel manipulators in which rigid links are replaced by cables. Even if they are widely known as promising devices, a single classification universally recognized is not available in literature. Furthermore, not even the terminology adopted is unified and different approaches are proposed.

A first differentiation can be done between planar and spatial robots. In the first case, the robot is forced to move in a specific plane of motion, while in the spatial case the workspace is three dimensional.

Both planar and spatial cable robots can be called translational if no rotation can be imposed on the end-effector.

Depending on the ratio between the number of cables and the number of degrees of freedom, different topologies can be identified. Similarly to parallel manipulators, cable robots are said to be fully actuated if the number of active cables, and hence of motors, is equal to the number of degrees of freedom. If the number of cables exceeds the number of degrees of freedom, the cable robot is said to be redundant or redundantly actuated. Conversely, if the number of cables is lower than the degrees of freedom, the cable robot is considered under-actuated.

If the focus is the ability of actually restrain the end effector, it is possible to distinguish between under-constraint and fully-constraints configuration. As a matter of fact, in order to obtain a fully-constraint configuration a number of cables greater than the number of degrees of freedom is usually necessary [63]. Generally speaking, a cable robot is fully constrained if, assuming unbounded cable tensions, it can maintain equilibrium against all external wrenches. It is important to notice that the previous condition is sufficient but not necessary; indeed, a cable robot can be under-constraint even if the number of cables is greater than the number of degrees of freedom: this happens for examples in suspended configuration where the robot must rely on gravity to maintain equilibrium. Conversely, it is always true that a number of cables less or equal to the number of degrees of

freedom leads to under-constraints configurations.

After a general overlook of possible configurations has been presented, let us consider a cable robot with m cables controlling n degrees of freedom. In Fig. 2.1 each $\mathbf{A}_i$ represents a pulley anchor point while $\mathbf{B}_i$ represents the attachment point on the moving platform. The origin of the reference frame Σ_{Oxyz} is indicated with **O** while barycenter of the moving platform with **G**.

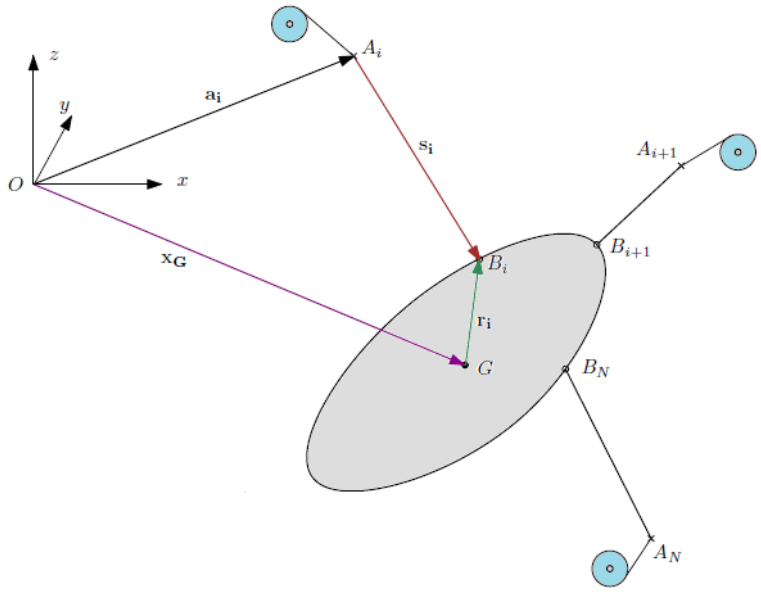

Figure 2.1: Scheme of a generic cable robot

2.1 KINEMATIC ANALYSIS

2.1.1 *Position*

The inverse kinematic problem consists in computing the the length L_i of the *i-th* cable starting from the known position of the center of mass $\mathbf{x}_G$. Each L_i an be found by solving the following equation:

$$\|\mathbf{x}_G + \mathbf{r}_i - \mathbf{a}_i\|^2 = \|\mathbf{s}_i\|^2 = L_i^2 \tag{2.1}$$

The counterpart problem consists in finding the position of **G** from knowns cable lengths.

The direct kinematic problem solution depends on the cable robot configuration, i.e. under or over actuated. In case of redundancy, the solution can be simply found by solving a system formed by each combination of n equations in (2.1). However, different combinations can lead to different solutions. If the solution is not unique, the one to

consider is the one describing a point inside the workspace. In case of point-mass end effector, the solution coincides with the intersections of circumferences having center in $\mathbf{A}_i$ and radius L_i. An example is given for a planar cable robot in Fig.2.2.

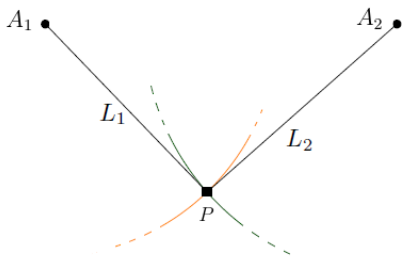

Figure 2.2: Intersection of circumferences for m=n=2

If the robot is under-actuated (m<n), the problem is more challenging. Indeed, each combination of fixed lengths L_i leads to infinite configurations of the end effector. In these particular cases, some geometry-static equations can be used to solve the direct kinematic problem as in [9, 19, 20, 35].

2.1.2 *Velocity*

The kinematic velocity analysis describes the relationship between the velocity of the end effector and the velocity at which cables are reeled of retracted. However, it is often more useful to find the relation between the velocity of the end effector and the velocity of the pulleys $\dot{\beta}_i$.

The velocity at which the pulley rotates results positive if the cable is retracted and negative if the cable is released and can be found by means of the following equations:

$$\beta_i = \frac{L_{i0} - L_i}{r} \quad i = 1, ..., N \tag{2.2a}$$

$$\dot{\beta}_i = -\frac{\dot{L}_i}{r} \quad i = 1, ..., N \tag{2.2b}$$

where r is the radius of the pulley, L_{i0} is the initial length of the *i-th* cable and β_i is the angular position of the corresponding pulley.

Given $\boldsymbol{\beta}$ and $\dot{\boldsymbol{\beta}}$, the vectors of angular positions and velocities of each pulley respectively, it is possible to write the following relation:

$$\dot{\boldsymbol{\beta}} = \frac{\partial \boldsymbol{\beta}}{\partial \mathbf{x}} \dot{\mathbf{x}} = \mathbf{J} \dot{\mathbf{x}} \tag{2.3}$$

where $\mathbf{x}$ and $\dot{\mathbf{x}}$ are the vectors of position and velocity generalized coordinates of the end effector, and the matrix $\mathbf{J} \in \mathbb{R}^{n \times m}$, called Jacobian matrix, is defined as follows:

$$\mathbf{J} = \begin{bmatrix} \frac{\partial \beta_1}{\partial x_1} & \frac{\partial \beta_1}{\partial x_2} & \cdots & \frac{\partial \beta_1}{\partial x_n} \\ \frac{\partial \beta_2}{\partial x_1} & \frac{\partial \beta_2}{\partial x_2} & \cdots & \frac{\partial \beta_2}{\partial x_n} \\ \cdots & \vdots & \cdots & \vdots \\ \frac{\partial \beta_m}{\partial x_1} & \frac{\partial \beta_m}{\partial x_2} & \cdots & \frac{\partial \beta_m}{\partial x_n} \end{bmatrix} \tag{2.4}$$

Solving the direct kinematic problem is more challenging than in conventional parallel robots. Indeed, usually a higher number of cables than degrees of freedom are required. For these configurations , the matrix $\mathbf{J}$ is not squared and the inverse problem written usually as $\dot{\mathbf{x}} = \mathbf{J}^{-1} \dot{\boldsymbol{\beta}}$ is not solvable straightforwardly.

In this case the so called pseudo-inverse matrix of $\mathbf{J}$ named $\mathbf{J}^*$ can be used to find one solution of the inverse kinematic problem.

The matrix J^* can have the following formulation depending on the cable robot configuration:

- $\mathbf{J}^* = \left(\mathbf{J}^T \mathbf{J}\right)^{-1} \mathbf{J}^T$, if m>n.
- $\mathbf{J}^* = \mathbf{J}^T \left(\mathbf{J}\, \mathbf{J}^T\right)^{-1}$, if n>m.
- $\mathbf{J}^* = \mathbf{J}^{-1}$, if m=n.

2.2 DYNAMIC ANALYSIS

In this section the dynamic analysis is presented. It represents the starting point of trajectory planning and hence it is the key issue when dealing with motion control and safety strategies. As already seen for the kinematic problem, the dynamic analysis can be direct or inverse. In the direct dynamic problem, the focus is to retrieve the motion low knowing the external and inertial forces of the system. The solution of the direct kinematic problem requires the integration of a differential equations system.

However, what is actually interesting when dealing with motion control, is the inverse kinematic problem. Solving the inverse dynamic allows finding the forces required to generate a desired motion low. To solve this problem, Newton approach is applied first to the end effector system and then to the pulley system. By considering the

two sub-systems together, the generic dynamic equilibrium equation for cable robots can be found.

2.2.1 *End-effector*

Let us consider the sum of forces $\mathbf{f}$ and moments $\mathbf{m}$ acting on the end-effector as the so called wrench vector $\mathbf{w} = \left[\mathbf{f}^T,\ \mathbf{m}^T\right]^T$. The dynamic equilibrium equation of the end effector, with respect to its center of mass, is given by:

$$\mathbf{M}\ddot{\mathbf{x}} = \mathbf{w} \tag{2.5}$$

where $\mathbf{M}$ is the matrix resulting by the combination of the mass matrix $\mathbf{M}_e$ and Inertia matrix $\mathbf{I}_e$ as:

$$\mathbf{M} = \begin{bmatrix} \mathbf{M}_e & 0 \\ 0 & \mathbf{I}_e \end{bmatrix} \tag{2.6}$$

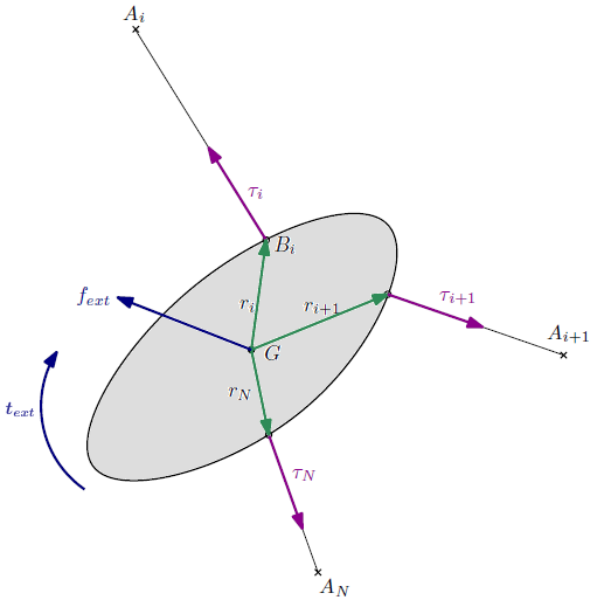

Figure 2.3: Schematic representation of the end effector

The vector $\mathbf{w}$ represents the sum of the external wrench applied on the end effector $\mathbf{w}_{ext}$ and the forces exerted by cables $\mathbf{w}_c$. The relation between $\mathbf{w}_c$ and the cables forces $\boldsymbol{\tau} = [\tau_1, \tau_2, \ldots \tau_m]^T$ can be expressed as:

$$\mathbf{w}_c = \mathbf{S}\boldsymbol{\tau} \tag{2.7}$$

where $\mathbf{S}$ is the so called structure matrix which projects the cable tensions along the Cartesian axes. Usually it takes the following form:

$$\mathbf{S} = \begin{bmatrix} \mathbf{u}_1 & \mathbf{u}_2 & \dots & \mathbf{u}_m \\ \mathbf{r}_1 \times \mathbf{u}_1 & \mathbf{r}_2 \times \mathbf{u}_2 & \dots & \mathbf{r}_m \times \mathbf{u}_m \end{bmatrix} \tag{2.8}$$

where:

- $\mathbf{u}_i$ is the unit vector from the attachment point on the base platform towards the *i-th* pulley.
- $\mathbf{r}_i$ is the vector from the center of mass towards the *i-yh* attachment point.

The meaning of $\mathbf{u}_i$ and $\mathbf{r}_i$ are clarified in Fig.2.4.

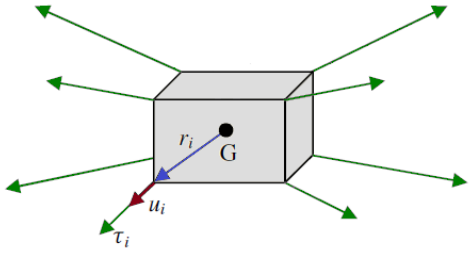

Figure 2.4: Schematic representation of the vectors $\mathbf{u}_i$, $\mathbf{r}_i$ e τ_i

When considering the vector $\boldsymbol{\tau}$, it is worth noticing that each of its component τ_i must be kept positive, possible between a minimum value τ_{min} and under a maximum value, namely τ_{max}. Such constraints must be satisfied during the whole trajectory in order to avoid slack or broken cables (causing loss of control of the manipulator).

By combing (2.7) and (2.5), it is possible to write the overall dynamic equilibrium equation of the end-effector as:

$$\mathbf{M}\ddot{\mathbf{x}} = \mathbf{S}\boldsymbol{\tau} + \mathbf{w}_{ext} \tag{2.9}$$

2.2.2 *Pulleys*

The forces acting on the *i-th* pulley are depicted in Fig. 6.4

The vector containing the motor torque $\mathbf{T} = [T_1,\ T_2 \dots T_m]$ is related to the corresponding cable tension through the following relation:

$$\mathbf{T} = \mathbf{I}_m\ddot{\boldsymbol{\beta}} + \mathbf{C}_m\dot{\boldsymbol{\beta}} + \boldsymbol{\tau}r \tag{2.10}$$

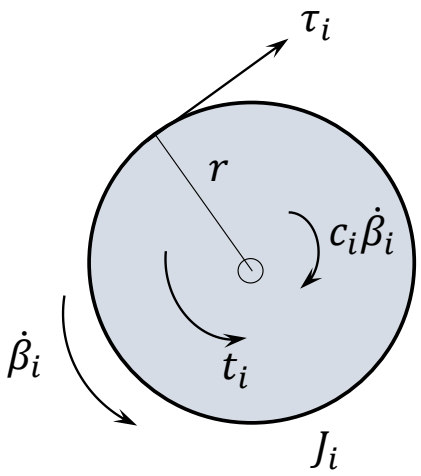

Figure 2.5: Scheme of a generic actuated pulley

which represents the dynamic equilibrium of the actuated pulley.

In (2.10), $\mathbf{C}_m$ and $\mathbf{I}_m$ are diagonal matrices having rotational inertia and rotational viscous damping coefficients on the respective diagonals.

The angular acceleration of the pulley can be easily found by computing the time derivative of (2.3):

$$\ddot{\boldsymbol{\beta}} = \frac{d}{dt}\frac{\partial \boldsymbol{\beta}}{\partial \mathbf{x}}\dot{\mathbf{x}} + \frac{\partial \boldsymbol{\beta}}{\partial \mathbf{x}}\ddot{\mathbf{x}} \tag{2.11}$$

The overall system dynamic can be found by substituting (2.3) and (2.11) into (2.10) as follows:

$$\mathbf{T} = \mathbf{I}_m\left(\frac{d}{dt}\frac{\partial \boldsymbol{\beta}}{\partial \mathbf{x}}\dot{\mathbf{x}} + \frac{\partial \boldsymbol{\beta}}{\partial \mathbf{x}}\ddot{\mathbf{x}}\right) + \mathbf{C}_m\frac{\partial \boldsymbol{\beta}}{\partial \mathbf{x}}\dot{\mathbf{x}} + \boldsymbol{\tau} r \tag{2.12}$$

which can be rewritten as:

$$\boldsymbol{\tau} = \frac{1}{r}\left(\mathbf{T} - \mathbf{I}_m\left(\frac{d}{dt}\frac{\partial \boldsymbol{\beta}}{\partial \mathbf{x}}\dot{\mathbf{x}} + \frac{\partial \boldsymbol{\beta}}{\partial \mathbf{x}}\ddot{\mathbf{x}}\right) - \mathbf{C}_m\frac{\partial \boldsymbol{\beta}}{\partial \mathbf{x}}\dot{\mathbf{x}}\right) \tag{2.13}$$

2.2.3 *Dynamic equilibrium equation of the robot*

It is now possible to substitute $\boldsymbol{\tau}$ as expressed in (2.13) in the Cartesian dynamic equilibrium of the end-effector in (2.9) as follows:

$$r\mathbf{M}\ddot{\mathbf{x}} = \mathbf{S}\mathbf{T} - \mathbf{S}\mathbf{I}_m\left(\frac{d}{dt}\frac{\partial \boldsymbol{\beta}}{\partial \mathbf{x}}\dot{\mathbf{x}}\right) - \mathbf{S}\left(\frac{\partial \boldsymbol{\beta}}{\partial \mathbf{x}}\ddot{\mathbf{x}}\right) - \mathbf{S}\left(\mathbf{C}_m\frac{\partial \boldsymbol{\beta}}{\partial \mathbf{x}}\dot{\mathbf{x}}\right) + r\mathbf{w}_{ext} \tag{2.14}$$

which can be rewritten as:

$$r\mathbf{M}\ddot{\mathbf{x}} + \mathbf{S}\mathbf{I}_m \frac{\partial \boldsymbol{\beta}}{\partial \mathbf{x}} \ddot{\mathbf{x}} + \mathbf{S}\left(\mathbf{I}_m \frac{d}{dt} \frac{\partial \boldsymbol{\beta}}{\partial \mathbf{x}} \dot{\mathbf{x}}\right) = \mathbf{S}\mathbf{T} + r\mathbf{w}_{ext} \tag{2.15}$$

The previous formulation can be rewritten in a standard Cartesian form for Cable Driven Robots as:

$$\mathbf{M}_{eq}(\mathbf{x})\ddot{\mathbf{x}} + \mathbf{N}(\mathbf{x}, \dot{\mathbf{x}}) = \mathbf{S}\mathbf{T} + r\mathbf{w}_{ext} \tag{2.16}$$

where:

$$\mathbf{M}_{eq}(\mathbf{x}) = r\mathbf{M} + \mathbf{S}\mathbf{I}_m \frac{\partial \boldsymbol{\beta}}{\partial \mathbf{x}} \tag{2.17}$$

and

$$\mathbf{N}(\mathbf{x}, \dot{\mathbf{x}}) = \mathbf{S}\left(\mathbf{I}_m \frac{d}{dt} \frac{\partial \boldsymbol{\beta}}{\partial \mathbf{x}} \dot{\mathbf{x}} + \mathbf{C}_m \frac{\partial \boldsymbol{\beta}}{\partial \mathbf{x}} \dot{\mathbf{x}}\right). \tag{2.18}$$

2.3 SUMMARY

This Chapter presented an overall classification of cable driven robots by giving an overview on the most common terminology in the field. Afterwards, the kinematic and dynamic analysis of a generic cable robot is presented in order to provide some useful hints that will be employed in the next Chapters to study the performance and safety issues of these devices.

3

PERFORMANCE EVALUATION

In this Chapter, the performance of cable driven robots are investigated. Firstly, an overview of the manipulator workspace possible definitions is given. After, classic indexes for parallel manipulator are analyzed in order to find similarities with the one proposed for cable driven robots. In particular, a local performance index is reported and a new efficient way to exploit such index in real-time motion planning is presented.

In section 1 the challenging issue of cable driven robot performance investigation has been introduced.

Clearly, such study cannot neglect the peculiarities arising from the need of keeping bounded cable tensions. As a result, even if cable driven robots are basically parallel robots, the performance indexes conceived for rigid links manipulators cannot be employed straightforwardly.

The performances of a parallel manipulator can be studied globally, in terms of workspace volume, or locally, in terms of available wrench set for a given pose.

The workspace evaluation is an essential preliminary activity in the design of a robot. Several definitions of workspace have been proposed in cable robotics. Among all, it is worth recalling the most commonly used:

- *Static Equilibrium Workspace*. The *SEW* is the set of poses of the end-effector at which equilibrium can be maintained while keeping positive tensions in all cables. An example of *SEW* analysis can be found in [53] for a six-degrees-of-freedom cable robot with constant orientation moving platform.

- *Wrench Closure Workspace*. By adding to the previous definition an external wrench one obtain the *WCW*, which can be defined as the set of poses for which any wrench can be generated at the end effector while maintaining tension in all cables [32].

- *Wrench Feasible Workspace*. The *WFW* is a more practical definition of *WCW* where both external wrenches and cable tensions are bounded [17].

- *Statically Feasible Workspace*. A special case of *WFW* is presented in [63] by considering just the gravity wrench: in the *SFW*, static equilibrium can be maintained against gravity with positive and bounded cable tensions.

All the previous workspace determination are based on the static equilibrium of the moving platform. However, by dynamically controlling cable robots, their workspace can be extended beyond the region of the set of platform poses for which static equilibrium can be obtained. This leads to the concept of dynamic workspace [6], which is peculiar to cable robots.

Besides the workspace evaluation, a few studies have been carried out in order to properly apply classic indexes based on the Jacobian Matrix to cable driven robots. Some examples are:

- *Manipulability*. Manipulability is a widely adopted index as a measure of the performance of a robotic system in the force domain, usually described by means of an ellipsoid or polytopes. The kinematic manipulability purpose is to help quantify the manipulator's velocity transmission capabilities or, equivalently, the dexterity of the robot. In 1985 Yoshikawa introduced the manipulability index for serial robots [67].

  In [27] a proper evolution of the Yoshikawa manipulability has been proposed for cable driven robots.

- *Condition Number*. The condition number is often used as an index to describe first the accuracy/dexterity of a robot and, second, the closeness of a pose to a singularity. It has the important advantage of being a single number for describing the overall kinematic behavior of a robot. In [53] the condition number is applied as is to a cable driven robot, by restricting the analysis to a specific workspace.

- *Isotropy Index*. An attempt to measure the level of isotropy behaviour of a manipulator is presented in [61] as The "Global Isotropy Index". Such isotropy measures is based on the robot behavior in the entire workspace. It is defined as the ratio of the minimum singular value of robot's Jacobian matrix to the maximum one obtained throughout the whole workspace not just at a single point. An interesting evolution of the isotropy index for cable robots, called tension factor, has been proposed in [50]. Such index is defined in the joint space by evaluating the ratio between maximum and minimum cable tensions. Another isotropy index has been defined in [59] for investigating the inertial properties of two rehabilitation cable robots. The index describes the maximum isotropic force that can be exerted in any direction. Such index has been then extended in [57] for application to reconfigurable cable robots with one or more moving pulley blocks.

A novel approach for local performance evaluation of cable driven robots has been introduced in [13]. Such approach has been further in-

vestigated and formalized in [15] as *Wrench Exertion Capability* index. Such index describes, for a given pose, the maximum exertable force/-torque in a particular direction while keeping positive and bounded cable tensions. This index is particularly useful when dealing with motion planning. Indeed, the maximum exertable force in a desired direction can be straightforwardly translated into a dynamic performance specification in terms of maximum linear acceleration of the platform along such direction. This approach can be exploited in case of cable failure to understand the residual force exertion capability in order to perform a feasible after failure motion. The employment of such an index as a base of recovery trajectories will be described in Chapter 4.

Since such index will be intensively employed in this dissertation, a background regarding the *WEC* is provided in the following Section.

3.1 WRENCH EXERTION CAPABILITY INDEX

In its initial formulation, the *WEC* index provides an evaluation of the performances of a robot along a direction of interest in terms of force or torque exertion capabilities. It is computed by solving a linear optimization problem involving the structure matrix $\mathbf{S}$ introduced in (2.8) and cable tension limits.

First a direction of interested is identified. Then, a new reference frame is defined having the *x-axis* aligned with the desired direction of motion. The relation between the absolute reference frame and the new one is described by a rotation matrix $\mathbf{R}$ (which is, in general, a function of two rotations α and β about independent axes). The the symbol d identifies the direction of interest while the two orthogonal direction are referred as o_1 and o_2 respectively. The structure matrix ca be divide into two parts: the first related to exerted forces, $\mathbf{S}_f$ and a second part related to exerted torques $\mathbf{S}_t$ such that $\mathbf{S} = [\mathbf{S}_f; \mathbf{S}_t]$.

By means of the matrix $\mathbf{R}$, it is possible to rotate these matrices to refer them to the new reference frame as follows:

$$\mathbf{R}^T\mathbf{S}_f := \begin{bmatrix} \mathbf{S}_{f,d} \\ \mathbf{S}_{f,o_1} \\ \mathbf{S}_{f,o_2} \end{bmatrix} \quad ; \quad \mathbf{R}^T\mathbf{S}_t := \begin{bmatrix} \mathbf{S}_{t,d} \\ \mathbf{S}_{t,o_1} \\ \mathbf{S}_{t,o_2} \end{bmatrix} \tag{3.1}$$

Then, the maximum exertable force in the direction of interest ($w_{f,d}$) can be found by solving the following linear programming problem:

$$\begin{aligned} &\text{maximize} \quad w_{f,d} = \mathbf{S}_{f,d}\boldsymbol{\tau} \\ &\text{s.t.} := \begin{cases} \begin{bmatrix} \mathbf{S}_{f,o_1} \\ \mathbf{S}_{f,o_2} \\ \mathbf{S}_{t,d} \\ \mathbf{S}_{t,o_1} \\ \mathbf{S}_{t,o_2} \end{bmatrix} \boldsymbol{\tau} = \mathbf{A}\boldsymbol{\tau} = \mathbf{0} \\ \boldsymbol{\tau}_{min} \preceq \boldsymbol{\tau} \preceq \boldsymbol{\tau}_{max} \end{cases} \end{aligned} \tag{3.2}$$

where $\boldsymbol{\tau}_{max}$ and $\boldsymbol{\tau}_{min}$ represent the vectors of upper and lower tension limits.

3.2 A NOVEL ALGORITHM FOR WEC INDEX COMPUTATION

Starting from its initial formulation, the *WEC* index has been reviewed and a novel computational approach has been investigated. Indeed, the original *WEC* formulation requires solving a linear programming problem. This does not represent an issue if the index is used at the design stage, i.e. off-line. However, limitations arise if the index is employed in real-time scenarios.

For example, one of the possible applications of the *WEC* index is to appraise immediately after failure the residual force exertion capability of a cable robot. Indeed, as proposed in [12], such index can be exploited to find the force, and hence acceleration, limits when facing the motion planning problem. However, due to its iterative nature, linear programming is not suitable to be used on-line.

The novel approach presented in this Section involves a geometry-based algorithm to overcome the problems related to the original numerical method. Compared to iterative algorithms, geometric algorithms are generally more efficient. Indeed, optimization-based methods are time expensive in terms of computation and hard to implement in real-time control because of their iterative nature [39]. Consequently, a deterministic non-iterative method is highly preferable. The new geometry-based approach is more suitable than the recursive linear programming method proposed initially in [13], enabling the use of the *WEC* index in real-time applications.

As previously introduced, the wrench exerted on the moving platform by cables can be referred to a new rotated reference frame hav-

ing the *x-axis* along the direction of interest. Hence, it is possible to define the wrench $\mathbf{w}_d$ by means of the following expressions:

$$\mathbf{w}_d = \begin{bmatrix} \mathbf{R}^T & \mathbf{o} \\ \mathbf{o} & \mathbf{R}^T \end{bmatrix} \begin{bmatrix} \mathbf{S}_f \\ \mathbf{S}_t \end{bmatrix} \boldsymbol{\tau} = \mathbf{S}_d \boldsymbol{\tau} \tag{3.3}$$

From a geometric point of view, the structure matrix $\mathbf{S}$ describes an affine transformation Γ from the m-dimensional tension space onto the n-dimensional wrench space, as depicted in Fig. 3.1 for a cable robots having 3 cables and 2 translational degrees of freedom.

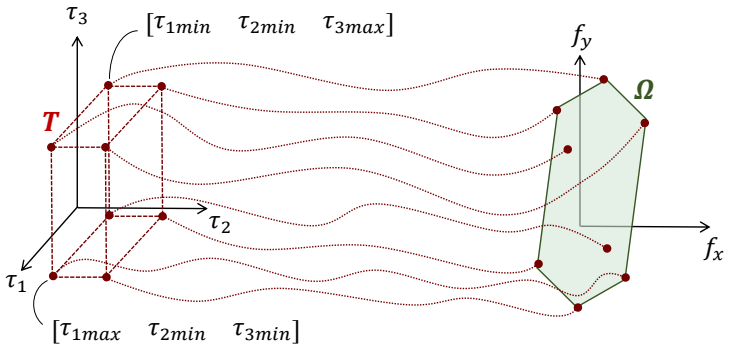

Figure 3.1: Tension and wrench polytopes for a m=3 n=2 cable robot

In the m-dimensional space, the bounded region of acceptable cable tensions can be defined as an orthotope $\mathbf{T}$:

$$\mathbf{T} = \left\{ \boldsymbol{\tau} | \boldsymbol{\tau} = [\tau_1 ... \tau_m]^T \in \mathbf{R}^m \text{ s.t. } \tau_i \in [\tau_{min}, \tau_{max}] \right\} \tag{3.4}$$

It can be noticed that, if τ_{min} and τ_{max} are fixed for all cables, then the orthotope is actually a hypercube. The hypercube $\mathbf{T}$ has 2^m vertexes $\boldsymbol{V}_j$, each corresponding to a particular tension configuration $\boldsymbol{\tau}_j = \left[\tau_{j_1} ... \tau_{j_m}\right]^T$, where all the components τ_i take either their maximum or their minimum value (i.e., $\tau_{j_i} \in \{\tau_{min}; \tau_{max}\}$).

All the vertexes $\boldsymbol{V}_j$ are projected onto the n-dimensional wrench space by the affine transformation Γ to obtain 2^m characteristic points $\boldsymbol{U}_j$ such that $\boldsymbol{U}_j = \Gamma(\boldsymbol{V}_j)$. The convex hull defined by the points $\boldsymbol{W}_h$ that encloses all the characteristics points $\boldsymbol{U}_j$ is the available wrench set $\boldsymbol{\Omega}$ for the given pose:

$$\boldsymbol{\Omega} = \{\mathbf{w}_d \in \mathbf{R}^n | \mathbf{w}_d = \mathbf{S}_d \boldsymbol{\tau}, \text{s.t.} \boldsymbol{\tau} \in \mathbf{T}\} \tag{3.5}$$

It follows that $\boldsymbol{W}_h$ are the vertexes of the wrench polytope $\boldsymbol{\Omega}$. If n=m, all the characteristic points $\boldsymbol{U}_j$ are vertexes of $\boldsymbol{\Omega}$; however, in the more general case n <m, only some $\boldsymbol{U}_j$ are vertexes while others

lie inside $\mathbf{\Omega}$ or on its surface [22]. An example is given in Fig. 3.2 for a simple planar point-mass robot with three cables controlling two degrees of freedom. The example describes the available force set in terms of F_d and F_o defined as $\begin{bmatrix} F_d & F_o \end{bmatrix}^T = \mathbf{S}_d \begin{bmatrix} \tau_1 & \tau_2 & \tau_3 \end{bmatrix}^T$. Matrix $\mathbf{S}_d$ is defined in equation (3.3) for $d = \pi/6$ (depicted with an orange arrow in Fig. 3.2). The manipulator layout is depicted on the left: the point-mass end effector is connected to the fixed frame through three cables attached to the points **A**(-1, -1)m, **B**(0, 1)m and **C**(1, -1)m. On the right, the cube represents **T** in the 3-dimensional tension space (axes τ_1 , τ_2 and τ_3); tension limits for this example are set to $\tau_{min} = 10$N and $\tau_{max} = 70$N. The eight vertexes of the cube are projected onto the 2-dimensional force space (axes F_d and F_o) to form the force polygon $\mathbf{\Omega}$. The projections of two of these vertexes lie inside the polygon proving that, in general, not all the projections of $\mathbf{V}_j$ represent a vertex of $\mathbf{\Omega}$.

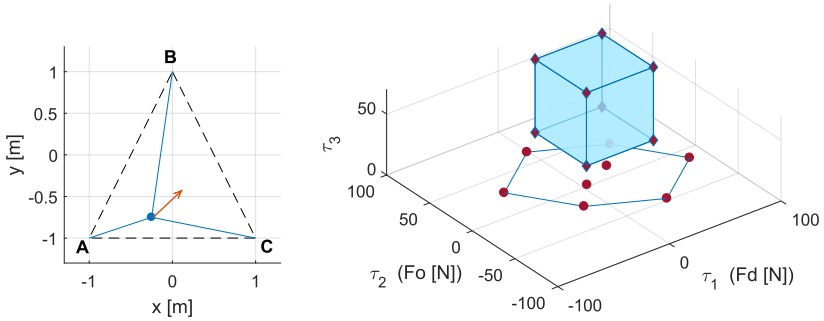

Figure 3.2: Example of a cable robots with m=3 n=2 (left) and its tension and wrench polytope (right)

It can be proved that **T** and $\mathbf{\Omega}$ are both convex polytopes [18].

Hence, it is possible to describe $\mathbf{\Omega}$ as Convex Hull, defined by its vertexes (*V-representation*) or as a bounded intersection of half-spaces, defined by hyperplanes supporting its faces (*H-representation*) [33]. The *V-representation* requires an iterative algorithm such as quickhull [5] to identify which characteristic points are actually vertexes. Even if quickhull is usually fast, a non-iterative algorithm is more desirable for real-time applications. Hence, in this work we exploit the hyperplane-shifting method proposed in [18] to get the *H-representation* of the wrench polytope. In its *H-representation*, the available wrench set $\mathbf{\Omega}$ is defined as a bounded intersection of closed half-spaces

$$\mathbf{\Omega} = \{\mathbf{w}_d \in \mathbf{R}^n | \mathbf{N}\mathbf{w}_d \preceq \mathbf{\delta}\} \tag{3.6}$$

where :

-**N** is a matrix having in each row the transpose of a unit vector $\mathbf{n}_i$ which is normal to the hyperplane supporting a face, directed away from the polytope (outer unit normal vector).

- δ is a vector whose element δ_i can be expressed using a known point $\mathbf{w}_{i0}$ belonging to the hyperplane, such that $\delta_i = \mathbf{n}_i^T \mathbf{w}_{i0}$.

A detailed description on how to determine the points $\mathbf{w}_{i0}$ can be found in [18] and will be briefly discussed here.

In [18] it is shown that the wrench set is a zonotope in which every face has at least one other face parallel to it. Consequently, for each vector $\mathbf{n}_i$ orthogonal to one face, there is another vector $-\mathbf{n}_i$ orthogonal to the corresponding parallel face.

Once that the normal vector $\mathbf{n}_i$ has been identified, the initial plane is shifted in the direction $\mathbf{n}_i$ and $-\mathbf{n}_i$ in order to identify completely the 2 parallel supporting hyperplanes. To do so, it is necessary to find two independent points $\mathbf{p}_i^+$ and $\mathbf{p}_i^-$ belonging to the supporting hyperplanes. The points $\mathbf{p}_i^+$ and $\mathbf{p}_i^-$ can be defined as a distance along $\mathbf{n}_i$. Such distances are called h_i^+ and h_i^- respectively and represent the projection of the vertexes inside the two faces on vector $\mathbf{n}_i$. The first step is to take l_j, the individual projections of the $\mathbf{w}_i$ on $\mathbf{n}_i$ using the dot product:

$$l_j = \mathbf{w}_j^T \mathbf{n}_i \tag{3.7}$$

Since all the vertexes represents a combination in which all the tensions are at their maximum τ_{max} or minimum τ_{min}, the $\mathbf{w}_j$ are weighted by 0 or $\Delta\tau$. For this reason, the two distances will be the maximum and minimum combinations of the lj weighted by 0 or $\Delta\tau$:

$$\begin{aligned} h_i^+ &= \max\left(\sum_{j=1}^{m-(n-1)} \alpha_j l_j \Delta\tau, \alpha_j = \{0,1\}\right) \\ h_i^- &= \min\left(\sum_{j=1}^{m-(n-1)} \alpha_j l_j \Delta\tau, \alpha_j = \{0,1\}\right) \end{aligned} \tag{3.8}$$

where m is the number of cables and n is the number of degrees of freedom.

The supporting hyperplane having $\mathbf{n}_i$ as outpointing normal vector will include the point:

$$\mathbf{p}_i^+ = h_i^+ \mathbf{n}_i + \mathbf{S}\boldsymbol{\tau} \tag{3.9}$$

The same reasoning can be applied to find the point belonging to the hyperplane having $-\mathbf{n}_i$ as normal outpointing vector:

$$\mathbf{p}_i^- = h_i^- \mathbf{n}_i + \mathbf{S}\boldsymbol{\tau} \tag{3.10}$$

The normal vector $\mathbf{n}_i$ and the corresponding point $\mathbf{w}_{i0}$ (i.e., $\mathbf{p}_i^+$ or $\mathbf{p}_i^-$) define an hyperplane $\boldsymbol{\Pi}_i \in \mathbf{R}^{n-1}$ supporting a face of the wrench polytope.

To identify $\mathbf{n}_i$, the hyperplane shifting method [18] consists in taking a set of *n-1* linearly independent unit wrenches $\mathbf{s}_i$ from the matrix $\mathbf{S}_d$. A normal vector $\mathbf{n}_i$ is then obtained by the normalization of the generalized cross product among these *n-1* vectors. This step must be repeated for all the feasible permutations of *n-1* unit wrenches. From combinatorics, the total number of permutations is $\frac{m!}{k!(n-1)!}$,where *k=m-n+1*. However, only the permutations involving *n-1* linearly independent vectors generate hyperplanes. Hence, if n_p indicates the number of hyperplanes, this process leads to a total of $2n_p$ normal vectors, the first n_p are the vectors $\mathbf{n}_i$, followed by their opposite $-\mathbf{n}_i$.

The matrix $\mathbf{N} \in \mathbf{R}^{(2n_p \times n)}$ can be written as:

$$\mathbf{N} = \begin{bmatrix} \mathbf{n}_1 & \mathbf{n}_2 & \cdots & \mathbf{n}_{n_p} & -\mathbf{n}_1 & -\mathbf{n}_2 & \cdots & -\mathbf{n}_{n_p} \end{bmatrix}^T \tag{3.11}$$

3.2.1 *Determination of the maximum exertable wrench*

Once all the hyperplanes have been identified, it is possible to analyse the boundaries of the polytope to find the maximum exertable force in the desired direction.
Two characteristics can be exploited to find the extreme wrench $\mathbf{w}_{max}$ (the same reasoning is valid for $\mathbf{w}_{min}$).

1. $\mathbf{w}_{max}$ lies in the hull of the wrench polytope, i.e., it belongs to at least one of its faces. Hence, for at least one of the $2n_p$ inequalities $\mathbf{N}\mathbf{w}_d \preceq \delta$, the expression $\mathbf{n}_j^T \mathbf{w}_{max}$ will reach its maximum value, such that $\nu n_j^T \mathbf{w}_{max} = \delta_j$. In other words, $\mathbf{w}_{max} \in \mathbf{\Pi}_j$, where $\mathbf{\Pi}_j$ is the hyperplane identified by $\mathbf{n}_j$.

2. Since $\mathbf{w}_{max}$ has all null wrench components except for the one in the direction of interest, it belongs to the straight line defined as $r = \lambda \mathbf{e}_1$, where $\lambda \in \mathbf{R}$ and $\mathbf{e}_1$ is the first column of the identity matrix $\mathbf{I}_n$: $\mathbf{w}_{max} = \lambda_j \mathbf{e}_1$.

For a generic wrench $\mathbf{w}_i \in \mathbf{R}^n$ that satisfies the above conditions, it is true that

$$\begin{cases} n_{i_1} * \lambda_i \leqslant \delta_i, \quad \forall i \in [1, 2n_p] \\ \exists j \in [1, 2n_p] \quad \text{s.t.} \quad n_{j_1} * \lambda_j = \delta_j \end{cases} \tag{3.12}$$

where n_{i_1} is the projection of $\mathbf{n}_i$ along $\mathbf{e}_1$.
Let us consider the set $\mathbf{I} = \{i \in [1, 2n_p]\}$; such a set can be divided into three subsets: $\mathbf{P} = \{i \in [i, 2n_p] \mid n_{i_1} > 0\}$, $\mathbf{Q} = \{i \in [i, 2n_p] \mid n_{i_1} < 0\}$ and $\mathbf{S} = \{i \in [i, 2n_p] \mid n_{i_1} = 0\}$.

For the following analysis to be valid, it is necessary to remove from $\mathbf{N}$ the faces whose normal vector is orthogonal to *r* (that is, those identified by the set of indexes $\mathbf{S}$); indeed, such faces cannot intersect

the straight-line r and hence can be excluded *a priori*.
Equation (3.12) can be therefore rewritten as:

$$\begin{cases} \lambda_i \leqslant \dfrac{\delta_i}{n_{i_1}}, \ \forall i \in \mathbf{P} \\ \lambda_i \geqslant \dfrac{\delta_i}{n_{i_1}}, \ \forall i \in \mathbf{Q} \\ \exists j \in [1, 2n_p] \setminus \mathbf{S} \ \text{ s.t. } \ n_{j_1} * \lambda_j = \delta_j \end{cases} \tag{3.13}$$

where the first two inequalities are equivalent to: $\max_{i \in Q} \left(\frac{\delta_i}{n_{i_1}} \right) \leqslant \lambda_i \leqslant \min_{i \in P} \left(\frac{\delta_i}{n_{i_1}} \right)$.
By adding the third condition, the previous inequalities can be further rewritten as: $\max_{i \in Q} \left(\frac{\delta_i}{n_{i_1}} \right) \leqslant \frac{\delta_j}{n_{j_1}} \leqslant \min_{i \in P} \left(\frac{\delta_i}{n_{i_1}} \right)$ from which one can infer that

$$\lambda_{j_{1,2}} = \max_{i \in \mathbf{Q}} \left\{ \frac{\delta_i}{n_{i_1}} \right\}, \min_{i \in \mathbf{P}} \left\{ \frac{\delta_i}{n_{i_1}} \right\} \tag{3.14}$$

are two solutions of (3.13) and therefore must be the two desired intersection points (i.e., the maximum and minimum exertable wrench in the desired direction).

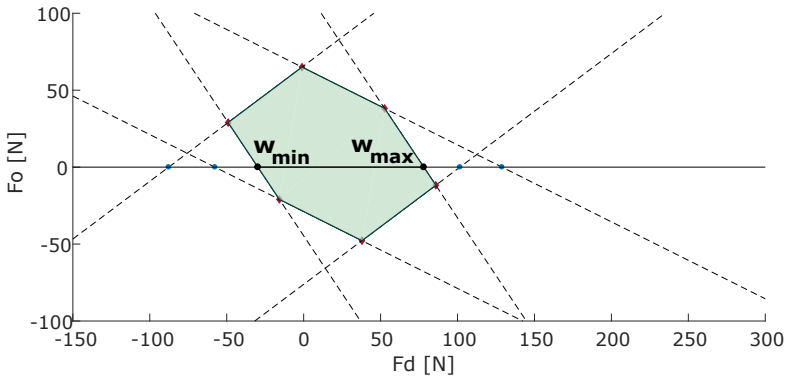

Figure 3.3: Tension and wrench polytopes for a m=3 n=2 cable robot

In other words, $\mathbf{R} = \{\mathbf{w}_i \mid \mathbf{w}_i = \lambda_i * \mathbf{e}_1, \forall i \in \mathbf{P} \cup \mathbf{Q}\}$ is the set of intersection points $\mathbf{w}_i$ between the $2n_p$ supporting hyperplanes $\mathbf{\Pi}_i$; only two of these points represent feasible wrenches (i.e., $\mathbf{w}_{max}$ and $\mathbf{w}_{min}$) while the others are points outside $\mathbf{\Omega}$.
The example in Fig. 3.3 shows the intersection points $\mathbf{w}_{max}$ and $\mathbf{w}_{min}$ corresponding to the cable robot and the desired direction shown in Fig. 3.2. The wrench space is actually a 2-dimensional force space, and the polytope $\mathbf{\Omega}$ is a polygon with six edges corresponding to six straight-lines (dashed-lines). The straight-line r coincides with the x-axis, and intersects the polygon $\mathbf{\Omega}$ in the two points $\mathbf{w}_{max}$ and

$\mathbf{w}_{min}$. The black line between these two points represents the feasible range for a force directed along $d = \frac{\pi}{6}$. The points $\mathbf{w}_i$, i.e., the intersections between the dashed lines and the x-axis, are depicted with blue circles.

The method can be applied even in presence of external loading such as, for example, the gravity force. Due to this external wrench, the zonotope is shifted in the wrench space. The direction of each supporting hyperplane does not change, while the point identifying the hyperplane position is shifted such that $\mathbf{w}'_{i0} = \mathbf{w}_{i0} + \mathbf{w}_e$.

3.2.2 *Determination of the tension configuration*

Once that the maximum exertable force or torque has been computed, it might be useful to find a feasible set of cable tensions corresponding to the local *WEC*, in addition to the *WEC* index. Because all the points on the hull of the zonotope are images of points that belong to the hull of the hypercube, the tension configuration corresponding to the extreme wrenches $\mathbf{w}_{max}$ and $\mathbf{w}_{min}$ has to be sought in the hull of the tension hypercube $\mathbf{T}$.

Indeed, each vertex $\mathbf{W}_h \in \mathbf{\Omega}$ is the projection of at least one vertex $\mathbf{V}_j \in \mathbf{T}$. Each $\mathbf{V}_j$ is directly connected to other m vertexes to form m edges. Moving along one edge of $\mathbf{T}$, the value of one tension force changes linearly from τ_{min} to τ_{max}. Similarly, the edges of the wrench zonotope are the projections of some of the edges of the tension hypercube. Hence, the wrenches of one edge are the result of the same tension configuration, except for one tension value: this value is τ_{min} in one vertex and τ_{max} in the other. It should be noted that this is not true when two or more vertexes of the wrench zonotope overlap and hence more than two $\mathbf{W}_h$ belongs to one edge of $\mathbf{\Omega}$. Therefore, in the following we exclude these special cases and assume that each vertex of the wrench polytope is the image of a single vertex of the tension hypercube.

The pre-images $\mathbf{V}_j$ of the vertexes $\mathbf{W}_h$ that delimit one face of the wrench polytope, have *m-n+1* common tension values; for all wrenches lying on the face, these values remain constant while the other *n-1* values change.

The normal vector that identifies each supporting hyperplane describes which tension values are fixed and common to the whole face (i.e., the ones related to the *m-n+1* unit wrenches that define the position of the face, in terms of distance along $\vec{n}_i$ between such face and the initial parallel hyperplane passing through the origin). Consequently, the values of the remaining *n-1* tensions corresponding to the desired wrench have to be determined.

Let us indicate the WEC index value as w_{max} (i.e., $\mathbf{w}_{max} = w_{max} * \mathbf{e}_1$). Moreover, let $\mathbf{n}_{max}$ be the vector normal to the hyperplane $\mathbf{\Pi}_{max}$, i.e., the one supporting the face to which $\mathbf{w}_{max}$ belongs. The contri-

bution of each unit wrench to $\mathbf{w}_{max}$ can be highlighted by rewriting (1) as:

$$\mathbf{w}_{max} = \mathbf{s}_1\tau_1 + \mathbf{s}_2\tau_2 + \cdots + \mathbf{s}_m\tau_m \tag{3.15}$$

where $\mathbf{s}_i$ is the *i-th* column of the structure matrix $\mathbf{S}$. Starting from $\mathbf{n}_{max}$, it is possible to trace back which are the unknown tensions that have to be calculated (i.e., $\boldsymbol{\tau}_u \in \mathbf{R}^{n-1}$) by looking at the specific permutation of *n-1* linearly independent unit wrenches $\mathbf{s}_i$ used to generate $\mathbf{n}_{max}$. The remaining *m-n+1* tensions represent the known vector $\boldsymbol{\tau}_k \in \mathbf{R}^{m-n+1}$.

Hence, the contributions to the exerted wrench are divided into two parts:

$$\mathbf{w}_{max} = \mathbf{S}_k\boldsymbol{\tau}_k + \mathbf{S}_u\boldsymbol{\tau}_u \tag{3.16}$$

where $\mathbf{S}_k \in \mathbf{R}^{n\times m-n+1}$ is the matrix obtained from $\mathbf{S}_d$ by selecting only the columns related to $\boldsymbol{\tau}_k$, and similarly $\mathbf{S}_u \in \mathbf{R}^{n\times n-1}$ is the matrix obtained by $\mathbf{S}_d$ by selecting only the columns related to $\boldsymbol{\tau}_u$. The objective is then to find $\boldsymbol{\tau}_u$, such that:

$$\mathbf{S}_u\boldsymbol{\tau}_u = \mathbf{w}_{max} - \mathbf{S}_k\boldsymbol{\tau}_k \tag{3.17}$$

Eq. (3.17) represents an overdetermined linear system of n equations with *n-1* unknowns. Such a linear system has a feasible solution because $\mathbf{w}_{max}$ lies inside the available wrench set. The overdetermined system can be easily solved by applying numerical methods such as Gaussian Elimination.

3.2.3 *Simulation and Results*

To show the efficiency of the new approach, the geometry-based algorithm is here applied to three different examples. The chosen topologies have $n \leqslant 3$ degrees of freedom to allow the visualization of the wrench zonotope. All the examples aim at finding the maximum and minimum exertable force in the direction of interest d. Such direction is depicted with an orange arrow in Fig. 3.4, 3.6 and 3.7.

The forces $\mathbf{F}$ and torques $\mathbf{M}$ exerted on the moving platform are rewritten in a more suitable reference frame as follows

$$\mathbf{w}_d = \begin{bmatrix} F_d & F_{o1} & F_{o2} & M_d & M_{o1} & M_{o2} \end{bmatrix}^T = \mathbf{R}^T\mathbf{S}_d\boldsymbol{\tau} \tag{3.18}$$

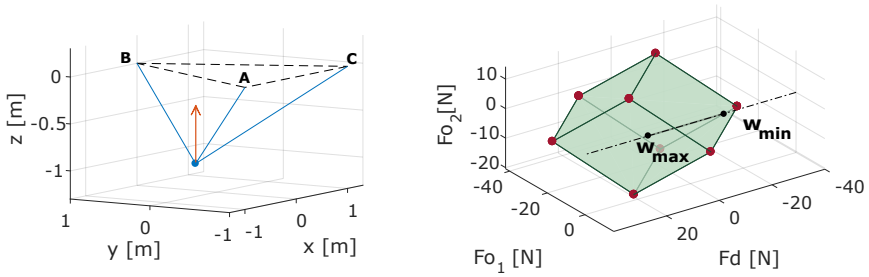

Figure 3.4: m=3 n=3 robot configuration(left) and available wrench set (right)

1. *Cable suspended configuration*
   Fig. 3.4 shows the cable robot configuration on the left and the corresponding wrench zonotope for the given pose on the right.

   The three degrees of freedom of the point-mass end effector are controlled by three cables attached to the points **A** (-1;1;0)m, **B** (0;1;0)m and **C** (1;-1;0)m. The direction of interest *d*is aligned with the *z*-axis. The green parallelepiped identifies the available wrench set in the 3-dimensional space. The dash-dotted line is the straight-line *r*; the intersection between *r* and $\mathbf{\Omega}$, depicted as a black segment, is the feasible range for a force exerted along *d*. Hence, it is possible to identify the two points $\mathbf{w}_{max} = [16\text{N}, 0, 0]^T$ and $\mathbf{w}_{min} = [-12\text{N}, 0, 0]^T$ on the surface of $\mathbf{\Omega}$.

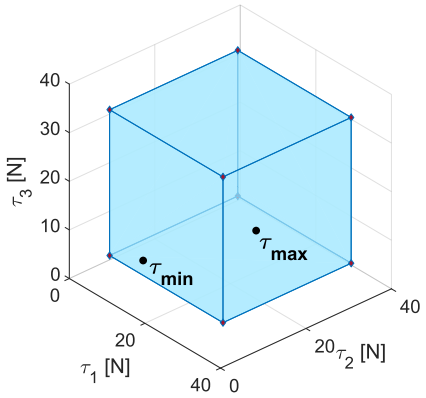

Figure 3.5: Tension cube

As for the tension configurations associated with the extreme wrenches $\mathbf{w}_{min}$ and $\mathbf{w}_{max}$, they belong to the tension hypercube hull, and have *m-n+1* tensions at their maximum or minimum values, i.e., $\boldsymbol{\tau}_k$.

For the cable suspended configuration showed in Fig. 3.4, $\boldsymbol{\tau}_k$ is actually a scalar value. In particular, the tension configuration

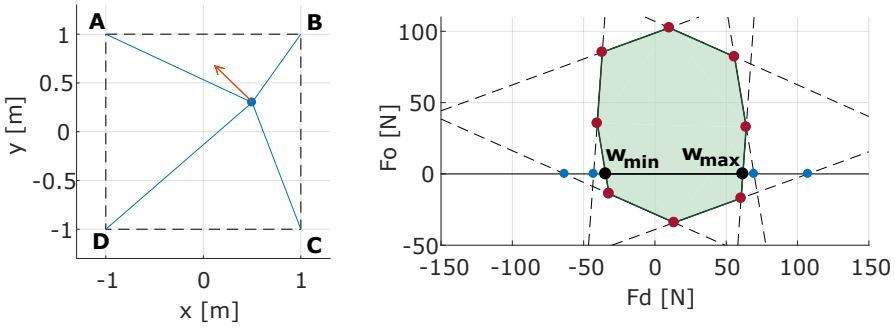

Figure 3.6: m=4 n=2 point mass cable robot

$\boldsymbol{\tau}_{max}$ exerting the wrench $\mathbf{w}_{max}$ belongs to the face $\tau_1 = \tau_{max}$, while the tension configuration $\boldsymbol{\tau}_{min}$ exerting the wrench $\mathbf{w}_{min}$ belongs to the face $\tau_2 = \tau_{min}$.

Fig. 3.5 shows the cube $\mathbf{T}$ in the 3-dimensional tension space; in this simulation the tension limits are chosen as: $\tau_{min} = 5\text{N}$ and $\tau_{max} = 35\text{N}$. The points $\boldsymbol{\tau}_{max} = [\tau_{max}, 13\text{N}, 20.5\text{N}]^T$ and $\boldsymbol{\tau}_{min} = [13.5\text{N}, \tau_{min}, 7.9\text{N}]^T$ can be easily identified on the cube surface.

2. *Over-constrained configuration*
The second example considers a planar point-mass manipulator controlled by four cables. Fig. 3.6 shows a schematic representation of the robot layout on the left and the available wrench set for the given pose on the right.

The four cables are attached to the vertexes of a square with side length of 2m; the origin of the fixed reference frame is located in the centroid of the square. The available wrench set is computed with reference to a direction of interest $\theta = \frac{3}{4}\pi$ (depicted with an orange arrow). In this case, $\boldsymbol{\Omega}$ is the octagon depicted with a green area in Fig. 3.6.

Again, the intersection between the x-axis (i.e., the straight line r) and the green area is a segment whose extreme points are $\mathbf{w}_{max} = [61.7\text{N}, 0]^T$ and $\mathbf{w}_{min} = [-34.5\text{N}, 0]^T$. Again, the straight-lines supporting the edges of the polygon are depicted with dashed lines intersecting r in the points $\mathbf{p}_i$.

Looking at the corresponding tension configurations, the hypercube $\mathbf{T}$ belongs to the 4-dimensional tension space. For the point-mass cable robot, the known tensions vector $\boldsymbol{\tau}_k$ belongs to $\mathbf{R}^3$; specifically, for the given pose $P = [0.5, 0.3]^T\text{m}$, the tension configurations exerting the maximum and the minimum force in the direction of interest are respectively $\boldsymbol{\tau}_{max} = [\tau_{max}, \tau_{max}, \tau_{min}, 37\text{N}]^T$ and the $\boldsymbol{\tau}_{min} = [\tau_{min}, 56\text{N}, \tau_{max}, \tau_{min}]^T$, where $\tau_{min} = 20\text{N}$ and $\tau_{max} = 70\text{N}$.

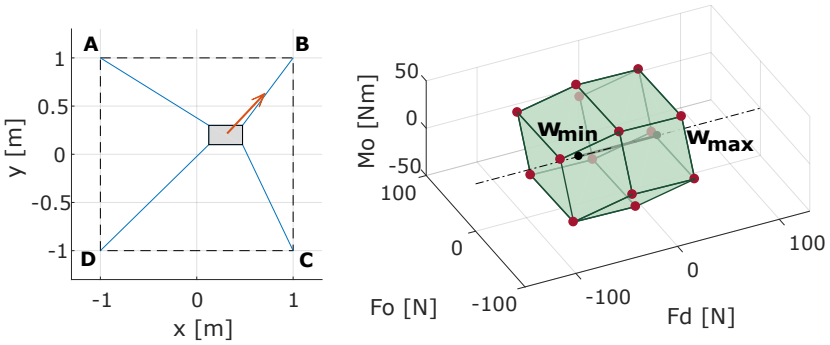

Figure 3.7: m=4 n=2 point mass cable robot

3. *Fully-constrained configuration*
   The third example refers to a planar cable robot having a moving platform controlled by four cables. The cable output points are located at the vertexes of a square whose size is the same as in Fig. 3.6. The moving platform is rectangular, with height 0.2m and width 0.35m. The orange arrow indicates the direction of interest (i.e., $\theta = \pi/4$) along which the platform should exert the maximum force while keeping constant its orientation. The available wrench set is a 3-dimensional figure, describing two translational and one rotational degrees of freedom. It is possible to identify the two intersection points $\mathbf{w}_{max} = [28.8\text{N}, 0, 0]^T$ and $\mathbf{w}_{min} = [-48.4\text{N}, 0, 0]^T$ between the straight line r and $\mathbf{\Omega}$. In this case, the vector of known tensions has $m - n + 1 = 2$ elements. Specifically, for the given pose $P = [0.3, 0.2]^T\text{m}$, the results are $\boldsymbol{\tau}_{max} = [60.9\text{N}, \tau_{max}, 66.5\text{N}, \tau_{min}]^T$ and the $\boldsymbol{\tau}_{min} = [\tau_{min}, 27.7\text{N}, 14.9\text{N}, \tau_{max}]^T$, with $\tau_{min} = 10\text{N}$ and $\tau_{max} = 70\text{N}$.

For each example, the computational time in case of the old linear programming approach and the new geometry-based approach are reported in Table 1.

Table 1: Computational Time

Case	Linear Programming	Geometry-based Algorithm
Suspended	100 ms	18 ms
Over Constrained	200 ms	19 ms
Fully Constrained	120 ms	18 ms

3.3 SUMMARY

This Chapter focused on the performance evaluation of cable driven robots. After an overview of existing approaches, a new and efficient geometry-based algorithm to determine the maximum exertable wrench in a given direction was presented. The proposed algorithm takes advantage of the *H-representation* of the wrench polytope and is not iterative. A method to obtain the set of cable tensions yielding the desired maximum wrench was also presented. Some representative examples have been investigated in order to show the improvement in computational time reached thanks to the new method.

4

RECOVERY STRATEGY BASED ON LINEAR TRAJECTORY

In this Chapter , a novel approach to deal with cable failure is presented. The need of an efficient after failure motion strategy has been widely discussed in Chapter 1. Here, a novel motion planning strategy is introduced for leading the end effector of a cable robot to a safe position of the workspace in case one or more cables brake or become slack during the motion. The strategy can be applied to any cable robot topology (i.e. to under actuated, fully actuated or redundant cable robots) in presence of any number of broken cables, provided that a not-null SEW is available after failure.

The proposed after failure recovery algorithm takes into account the modification of the *SEW* induced by cable failure, identifies a "safe pose" where static equilibrium can be achieved and then plans a feasible motion aimed at leading the end effector toward the safe pose and stopping it there. The motion is split into two parts addressing different motion requirements. Such an algorithm takes advantage of the *WEC* index introduced and discussed in Chapter 3.

4.1 GENERAL FORMULATION

The after failure real-time motion strategy proposed in this Chapter consists in promptly driving the end-effector to a pre-computed safe pose (actually a "safe point" in the case of a point-mass cable robot) where the robot can be stopped, in a time that should be kept to a minimum. The safe point can be chosen arbitrarily, depending on some special needs (i.e. to move the end effector far from human operators) or desired after failure performances (i.e. to stop as quick as possible). In absence of specific needs or expected performances, a reasonable choice for the safe point could be the point with the maximum isotropy in terms of exertable force in the after-failure SEW. Indeed, such a point is expected to offer the best performance in terms of end-effector braking capacity irrespective from the direction of motion of the end-effector before failure.

In order to simplify the task of minimizing the time needed to reach the safe point while keeping always positive and bounded cable tensions, it is essential to plan the motion along a geometrically simple path: a reasonable choice would obviously be a straight line path from the position where failure takes place toward the safe point. However, in general, such a straight path cannot be followed immediately after

failure, since the initial (i.e. after failure) conditions of the end-effector would prevent tracking such a path. Hence, a short connecting path is needed between the point where failure takes place and a point, identified dynamically, from which a precise straight line path toward the safe point can be planned and accurately tracked (referred here as CP).

In the following Sections the proposed after failure strategy is applied to planar and spatial configurations.

The strategy is divided between the connecting path and the straight line path. As previously introduced, the strategy takes advantage of the *WEC* index introduced in Chapter 3. Such index should be used in real-time immediately after failure to apply a suitable and feasible force on the end-effector, and it is has been widely discussed how numerically based algorithms are too time expansive to be used in this scenario. Below, different techniques to cope with this issue are proposed, depending on the available controller and on the desired final performance.

- *Off-line approach.* A real-time compatible geometry based algorithm was proposed in Chapter 3. However, a different approach can be adopted for planar cable robot based on off-line computation of look-up tables. This approach allows having a ready-to-use force interval that describes the residual force exertion capability of the manipulator. Such force interval can be use to actually plan a linear motion law from the place where the failure takes place to the safe point, provided that the required force profile satisfies the precomputed bounds.

- *Real-time approach.* A second approach is proposed based on the on-line computation of the *WEC* index. Such approach is based on exerting the maximum exertable braking force once that the end effector has completed the connecting path and its velocity is directed towards the safe point. This approach is simpler from a controlling point of view, but does not ensure a smooth trajectory as the one obtained using precomputed force bounds. Moreover, on-line computations are actually required. Hence, the off-line approach could also be a good choice in case the focus is keeping the on-line computation to a minimum and rely on ready-to-use information. Finally, the off-line approach is hardly applicable to spatial configuration, and hence the on-line approach is more suitable when not planar cable robots are involved.

The strategy is here presented for planar and spatial configurations. In order to avoid repetitions, the off-line approach is discussed for the planar configuration, while the on-line approach based on the geometric algorithm is presented for the spatial case. As already stated, the on-line approach can be easily scaled to the planar case, while the

off-line approach would actually be efficient only for planar configurations.

4.2 PLANAR CONFIGURATION

In its first formulation, the strategy is presented by referring to a point-mass, translational, planar and redundant cable robot and assuming that just a single cable brakes. This condition leads to a fully constrained and with a single degree of redundancy configuration after failure. Such a configuration gives the possibility of computing the position, velocity and acceleration of the end-effector, without using a separate metrology system, but merely exploiting the known angular positions of the winch actuators. Nonetheless, the method could be adopted also in less restrictive conditions provided that a suitable metrology system was available for measuring the end-effector position, and that a SEW existed after failure.

For what concern the straight path, it is worth mentioning that it takes advantage of the *WEC* index . Due to its iterative nature, the use of the WEC for this purpose may take long computational times. It is always possible to take advantage of the new geometry-based approach introduced in Chapter 3. However, if the controller is very basic or to keep the after failure strategy simpler, it is possible to perform an off-line analysis, considering each possible failure scenario. Such analysis is presented in the following section.

4.2.1 *The off-line analysis*

As already stated above, the after failure straight line path is not known a priori. Indeed, it depends on the connecting path which in turn depends on the failure conditions. To perform a feasible linear motion low, it is essential to know the force bounds along the whole path a-priori. However, the aforementioned analysis cannot be executed on-line, because it is likely to be very time consuming and not compatible with a real-time use of the strategy. One way to overcome such an issue, is to perform an off-line analysis by means of the *WEC*. Such analysis is undertaken a-priori for a sheaf of straight lines through each pre-computed safe point of the SEW. In this way, force bounds can be computed for each failure scenario and then for each possible path. The analysis can also be performed outside the SEW, in the so called dynamic equilibrium workspace and therefore it can support the whole motion of the end-effector after failure. It is important stressing that, by the *WEC* it is possible to plan a feasible motion along a straight line, always keeping positive and bounded tensions in all the cables.

The main goal of the off-line analysis consists in detect all the possible scenarios that may occur after the failure of one or more cables.

For each scenario the off-line analysis identifies a safe pose/point. As mentioned above, the safe point can be chosen arbitrarily: indeed, depending on some special needs or desired after failure performances, each point defined inside the after failure SEW can be adopted as safe point. Finally, this analysis takes into account the corresponding residual force exertion capability throughout the workspace for each safe point. The maximum and the minimum exertable forces towards the safe point are computed by means of WEC in the direction pointing the safe point.

Since the robot behavior may significantly differ throughout the workspace, the force bounds can be over conservative and hence too long lasting. Therefore, it is here suggested to split the workspace into radial sectors centered in the chosen safe points. Then, following the reasoning stated above, force limits can be computed for each sector, and just the limits of the sector of interest should be considered when planning the straight line path. In this way, a more accurate description of the residual exertion capability can be achieved. The off-line analysis can be summarized as follows:

- Identify all the possible failure scenario
- For each failure scenario, define the position of the corresponding safe point
- Divide the workspace into sectors centered in the safe point (optional)
- For each sector, define the precautionary force bounds along a straight line path towards the safe point.

4.2.2 *Connecting Path*

As previously mentioned, in order to reach a desired safe point through a linear path, an initial connecting path must be generated from the point where the failure took place (*FP*) to a point from which a straight line path can actually be planned and tracked (*CP*). When the end effector reaches such a point, its velocity has to be aligned with the desired direction of motion, i.e. a straight line ending in the safe point. Along such a connecting path, a new and ever changing tension configuration of the cables is applied to the end-effector in order to change its direction of motion and make it point the safe point. Suppose that the starting condition at the failure instant is described in Fig.4.1. Henceforth, the unit vector r will be used to describe the desired direction of motion corresponding to the straight line connecting, at each time instant, the end-effector EE with the chosen safe SP: r keeps changing along the connecting path. Let us introduce a moving reference frame identified by the unit vectors r and t as depicted in Fig.4.1 left by means of orange arrows. The direction of motion keeps

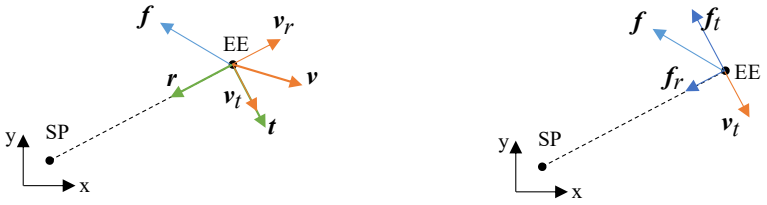

Figure 4.1: The end-effector velocity (left) and force (right) configuration at the failure instant

changing during this phase as well as the new reference frame. The vector $\mathbf{v}$ identifies the velocity of the end-effector at the failure instant while v_r and v_t represent its projections along the moving reference frame axes. A connecting path is generated as long as the tangential velocity component v_t differs from zero considerably. Afterwards, the straight line motion along the direction r can be planned. To this purpose, a suitable force $\mathbf{f}$ must be exerted by the unbroken cables. The force vector $\mathbf{f}$ and its projections f_r and f_t along r and t are depicted in Fig.4.1 right with blue arrows. Let us denote with $\mathbf{R}$ the rotation matrix that describes the orientation of the moving reference frame with respect to the absolute reference frame. The translational velocity $\mathbf{v}$ of the end-effector and the exerted force $\mathbf{f}$ can be expressed in the moving reference frame by means of the following relations:

$$\begin{bmatrix} v_r \\ v_t \\ 0 \end{bmatrix} = \mathbf{R}^T \begin{bmatrix} v_x \\ v_y \\ 0 \end{bmatrix} = \mathbf{R}^T \mathbf{S} \boldsymbol{\tau} = \begin{bmatrix} \mathbf{s}_r^T \\ \mathbf{s}_t^T \\ 0 \end{bmatrix} \boldsymbol{\tau} \tag{4.1}$$

The main goal along the connecting path is minimizing v_t to a small value v_t* close to zero (i.e. achieving $|v_t| < v_t*$). At each time step, a new cable tension distribution must therefore be sought maximizing ft in order to promptly reduce v_t.

Such a tension distribution can be found by solving the following linear programming (LP) problem:

$$\begin{aligned} &maximize(-sgn(v_t) * f_t) = -sgn(v_t) * \mathbf{s}_t^T \boldsymbol{\tau} \\ &\text{s.t.} \begin{cases} \mathbf{s}_r^T \boldsymbol{\tau} \geqslant 0 \\ \boldsymbol{\tau}_{min} \preceq \boldsymbol{\tau} \preceq \boldsymbol{\tau}_{max} \\ \tau_f = 0 \end{cases} \end{aligned} \tag{4.2}$$

The first constraint ensures that the force exerted is directed toward the chosen safe point. The other constraints refers to cable tensions to ensure that they are kept positive and bounded in all cables apart

from the broken one, which tension (τ_f) is set to zero. The LP problem is iterated until $|v_t| \geqslant v_t*$.

This phase can be summarized as follows:

- identify the position of the end-effector (EE) when a cable fails.
- identify the corresponding safe point (and the sector if defined).
- compute and apply the tension distribution to perform the connecting path.
- Iterate until $|v_t|$ reaches a suitable small value.

4.2.3 *Straight Line Path*

Once v_t has reached a suitable small value, it is possible to plan a safe and feasible motion along a straight line toward the safe point. Feasibility implies positive and bounded tensions in all the unbroken cables. Theoretically, by using the *WEC* index, it is possible to compute the maximum and minimum exertable forces (i.e. the force bounds) for each point of the desired straight path. However, it is suggested to split the workspace into radial sectors centered in the chosen safe point. Then, precautionary force bounds can be computed for each sector, and just the limits of the sector of interest should be considered when planning the straight line path. In this way, less restrictive bounds of the force exertion capability can be considered. Indeed, the robot behavior may significantly differ throughout the workspace. Once the force bounds are available, a conservative choice consists in planning a trajectory respecting the most restrictive limits of the corresponding sector. Such a condition ensures planning a certainly feasible trajectory regardless of the chosen motion law [4]. Without lack of generality, in this work the trajectory will be planned using polynomial functions [11].

This phase can be summarized as follows:

- Identify the sector to which CP belongs
- Consider the corresponding force bounds
- Plan a feasible linear motion from CP toward the safe point SP.

An overview of the proposed strategy can be found in the flow chart in Fig.4.2. When a failure occurs, a connecting path is generated by iterating the algorithm described in the previous section. When the tangential velocity v_t reaches a suitable small value, a straight line path can be planned by exploiting the force bounds limits previously computed in the off-line analysis. The straight line motion is planned from the point at the end of the connecting path CP to the safe point SP.

Figure 4.2 presents a flow chart of the overall recovery strategy in case the off-line analysis is chosen.

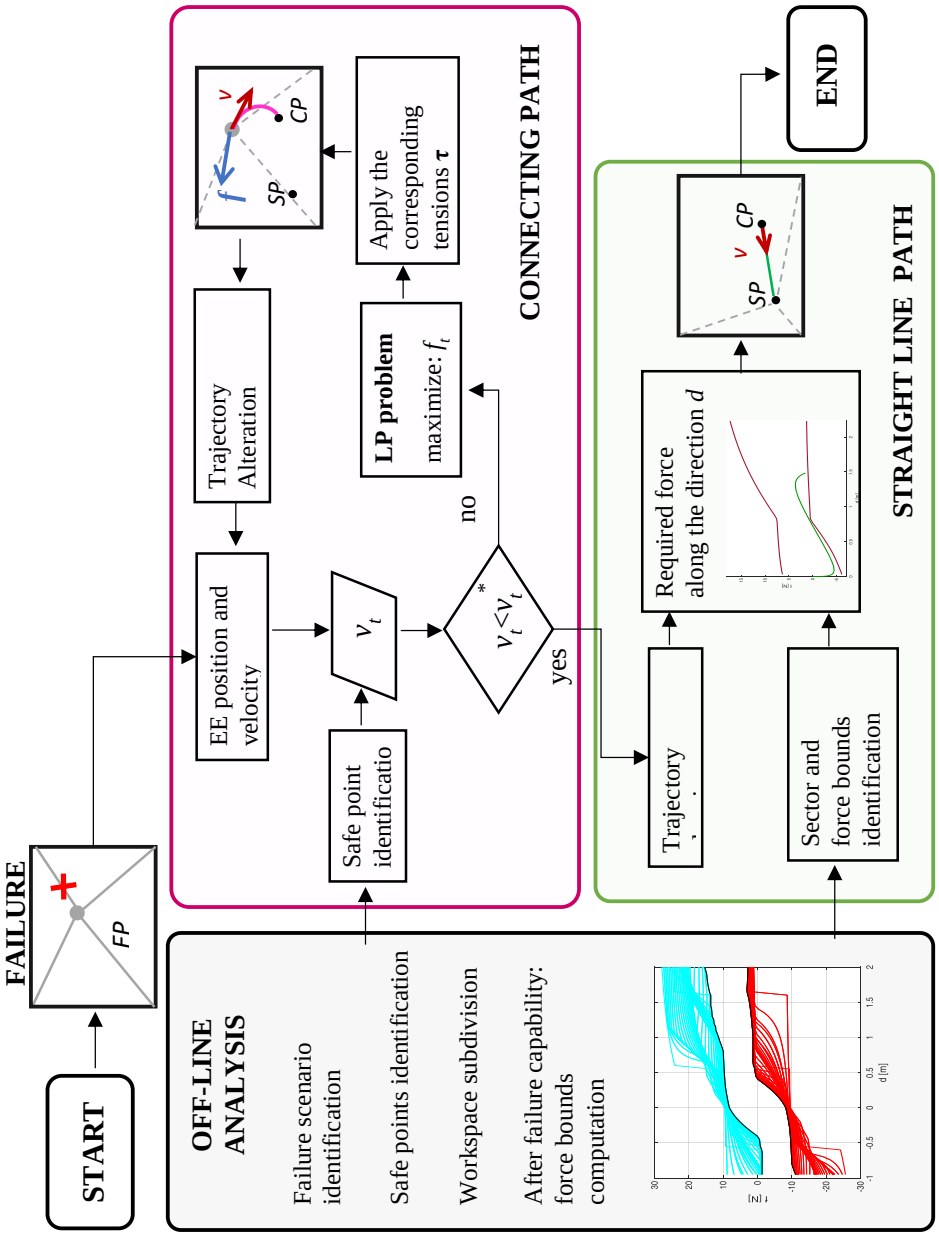

Figure 4.2: After failure strategy flow chart

4.2.4 *Simulations*

The strategy described above is here applied to a point-mass planar cable robot, with four cables and two translational degrees of freedom.

The initial SEW of the robot is a square with 2 m side length. The origin of the reference frame is located in the centroid of the square. The workspace vertexes coincide with the cable anchor points. In this analysis it will be assumed that a single cable brakes. Four reasonable safe points have been identified: SP=($\pm\sqrt{3}/3$m, $\pm\sqrt{3}/3$m). The sign of the coordinates is related to the broken cable. For example if the failed cable is the one attached to vertex B, then the SP is the point with the maximum isotropy in the 3rd quadrant, since the SEW after failure coincides with the triangle A-D-C. Maximum and minimum tension limits have been set equal, respectively, to 10 N and 0.5 N, while the mass of the end-effector has been set equal to 3 kg. In order to prevent excessive cable stresses, the maximum tension limit has been reduced to 7.5 N for after failure motion planning (safety bound).

Suppose that the cable attached to vertex B breaks; the corresponding residual force exertion capability throughout the original (square) SEW is is computed referring to the direction of the Safe Point. In practice, the original SEW of the robot has been discretized through a regular and thick grid. Subsequently, by means of a linear interpolation, the isolines of the maximum and minimum exertable forces that can be exerted along the direction toward the safe point have been computed and plotted in Fig.4.3. Negative values refer to the outward radial direction. In both the figures the forces take the lower values nearby the SP, and increase significantly when moving radially from this point. Clearly, only in the subspace where negative lower bounds are available it is possible to decelerate the EE.

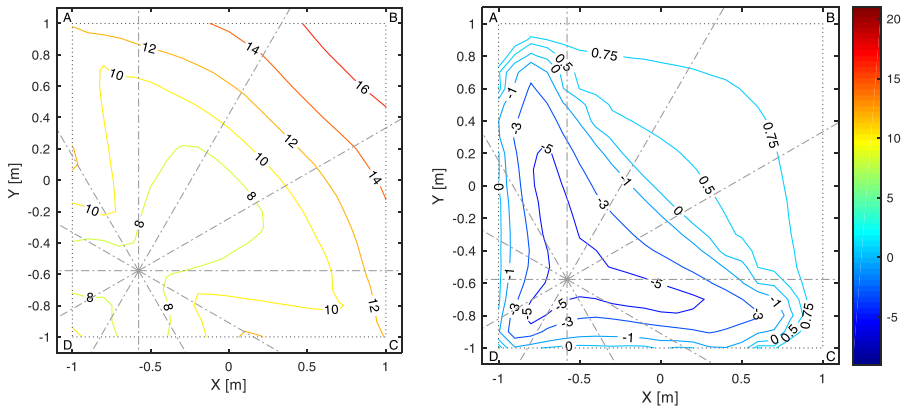

Figure 4.3: Maximum and Minimum exertable forces along the directions toward the SP

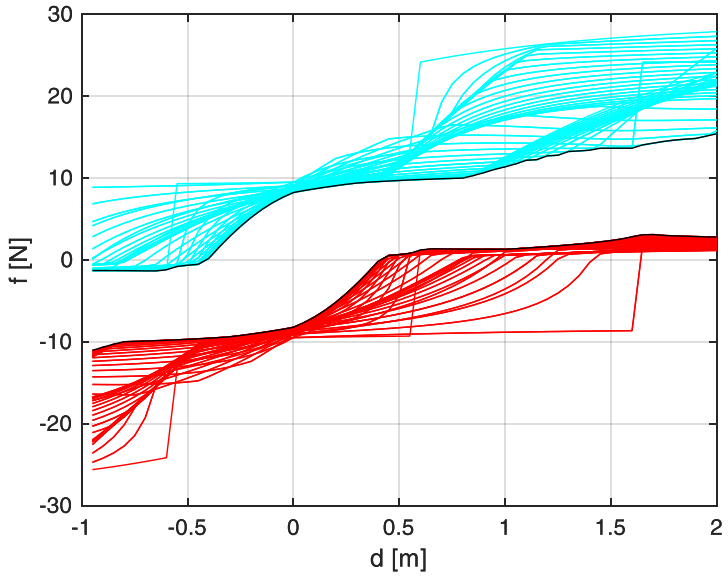

Figure 4.4: Maximum (cyan) and Minimum (red) exertable forces along the directions toward the SP from any point of the workspace.

In Fig.4.4, the maximum and the minimum exertable forces along the directions toward the safe point from any point of the workspace are plotted. The value d along the x-axis represents the radial distance from the safe point. Ideally, the objective is to perform a straight path from the point at the end of the connecting path (CP) to the safe point (SP). However, it can happen that a feasible linear motion along this segment does not exist (i.e. it is not possible to find a corresponding force profile fitting the pre-computed force bounds). In this case, it might be necessary to go beyond the safe point before being able to stop the end-effector. When this condition occurs, the radial distance d referred to any desired direction of motion is considered negative.

Since the robot behavior significantly differs throughout the workspace, the resulting force bounds result to be too conservative. Therefore, it is suggested to split the workspace into radial sectors centered in the chosen safe point. It has been chosen to split the square SEW into twelve sectors about the SP. The sectors are delimited by grey dash-dotted lines in Fig.4.3.

A cable breakage has been simulated. The failure is assumed to take place at time t_f along a linear path. Table 1 summarizes the position and the velocity of the end effector (EE) at t_f. The same table also shows the EE position and velocity achieved at the end of the connecting path (i.e. at the time t_c). In this simulation v_t^* was set equal to 10^{-3} m/s. In particular, the distance d from the SP and the velocity v_r at t_c represent the inputs for straight line trajectory planning.

	t_f	t_c
x[m]	0.378	0.424
y[m]	0.125	0.192
d[m]	1.186	1.263
v_r[m/s]	-0.411	0.32
v_t[m/s]	-0.613	$0.7 * 10^{-3}$

Table 2: position and velocity at different instances of the strategy

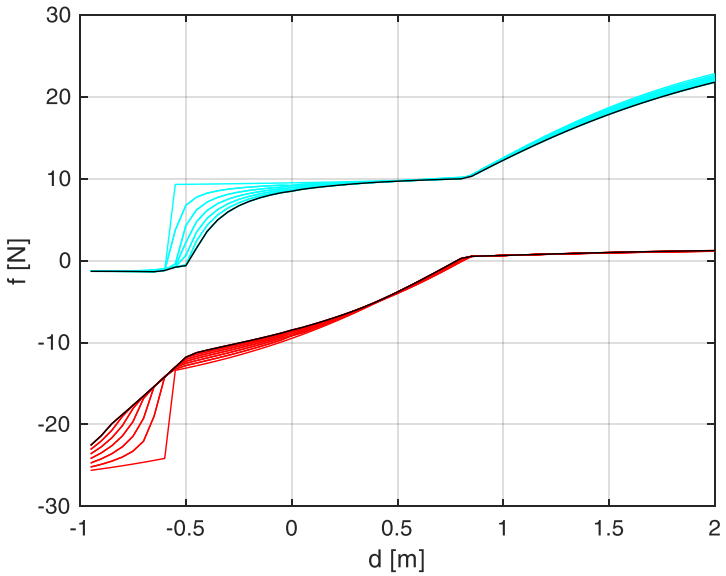

Figure 4.5: Maximum (cyan) and Minimum (red) exertable forces along the directions toward the SP from any point in the sector of interest

At time t_c, the EE is located in the central sector of the first quadrant. The force bounds computed off-line for this sector are depicted with black lines in Fig.4.5 they represent the most conservative choice considering the maximum (red lines) and minimum (cyan lines) bounds computed for each possible straight line paths belonging to this sector (computed using steps of 10°).

As defined above, $d(t_c)$ and $v_r(t_c)$ are respectively the distance of the end-effector from the safe point at the end of the connecting path and the velocity at the same instant, while and $a_r(t_c)$ is the defined initial acceleration (induced by the cable forces) of the new motion low. The chosen trajectory is plotted in Fig.4.6 in terms of distance from the SP, modulus of the velocity v_r and of the acceleration a_r. The x-axis represent the time between the instant t_c, i.e. the instant characterizing the end of the connecting path, and the instant in which the end effector reaches the safe point. Then the force exerted to perform such a trajectory is depicted in green line in Fig.4.7 proving that it satisfies the force bounds.

In Fig.4.8 the whole path traversed by the end-effector is depicted. The path before failure (1), the connecting path (2) and the straight line path to the SP (3) are plotted in different colors. The triangular SEW holding after failure is highlighted too. Finally, the cable ten-

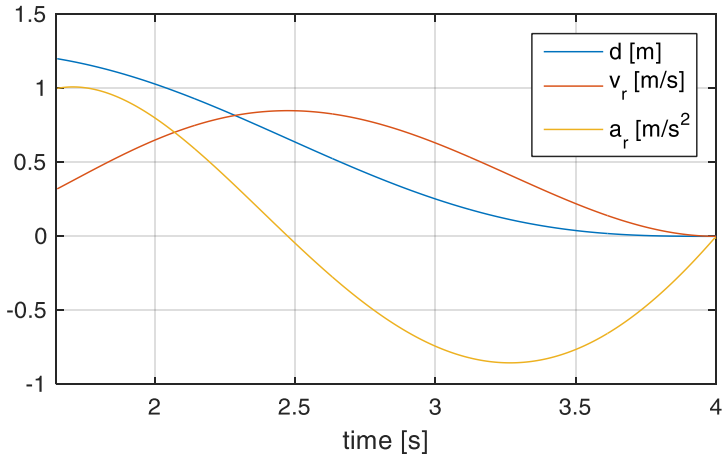

Figure 4.6: The motion law of the straight trajectory

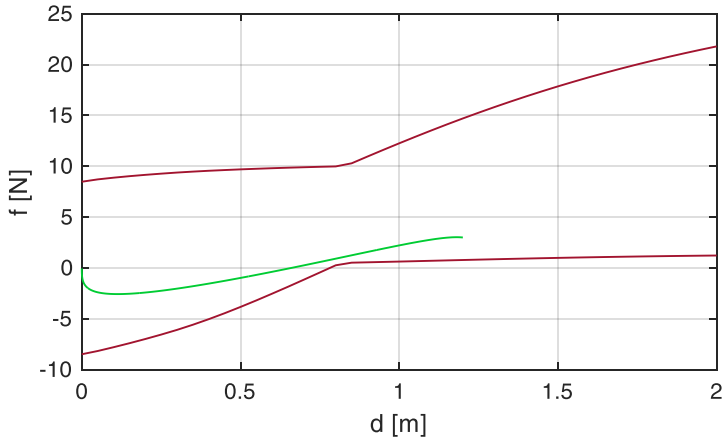

Figure 4.7: The exerted force of the straight trajectory and its bounds

sion distributions during the whole path are plotted in Fig.4.9 : it is proved that tensions are always kept within the bounds. Roughly intuitively, it is possible to recognize the three motion phases mentioned above: phase 2 represents the outcome of the LP maximization aimed at minimizing the tangential velocity v_t. The consequence of such a tension distribution is the magenta connecting path. It is worth observing that in this phase the tension of cable 1 (the one attached to the vertex A) reaches the maximum allowable value (decreased to 7,5N), while cable 2 and 3 (corresponding respectively to the vertexes C and D) assume the minimum value. Obviously, the tension of the broken cable turns into zero at the failure instant. Conversely, phases 1 and 3 are tension distributions required to obtain a given motion law (i.e. to the blue and green paths in Fig.4.8)

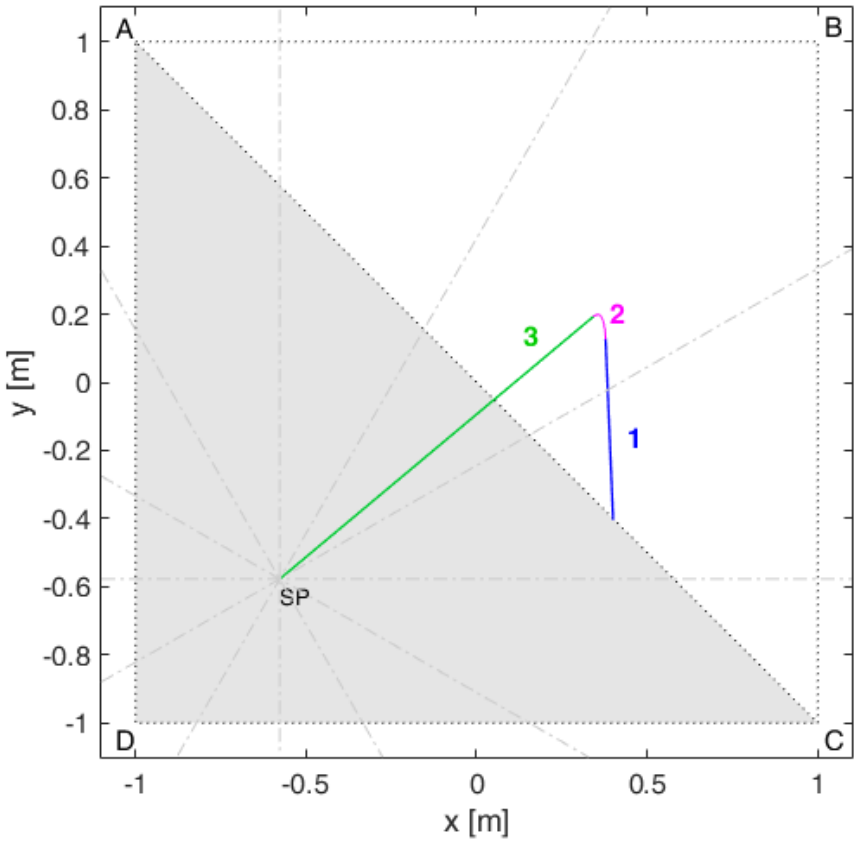

Figure 4.8: Path during the whole motion

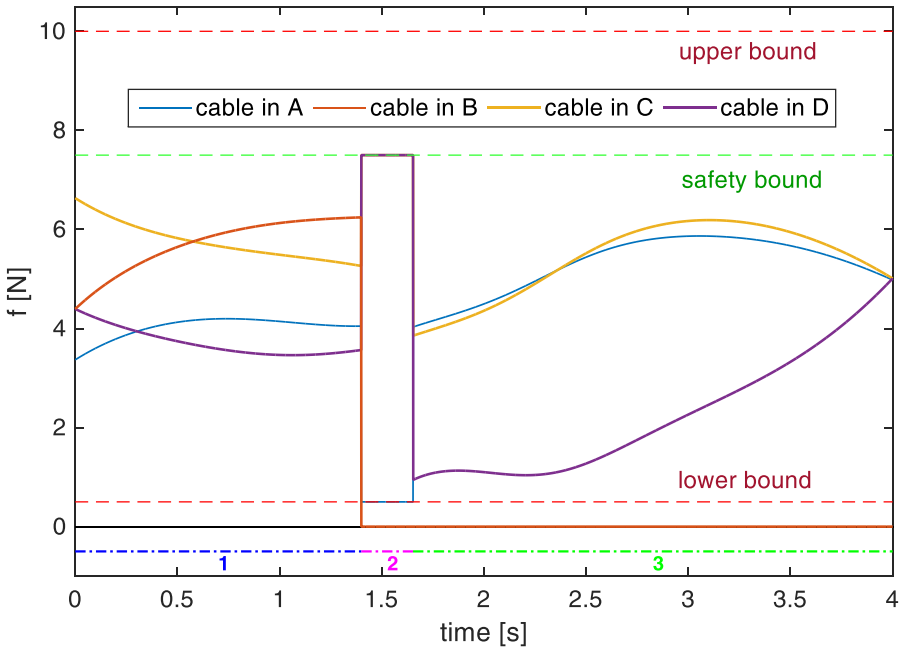

Figure 4.9: Cable tensions during the whole motion

4.3 SPATIAL CONFIGURATION

In this section the strategy is applied to a spatial cable robot. We refer here to a point-mass cable robot, focusing on the translational DoF. Indeed, controlling the position of the end effector represents the main issue in case of failure. In cable robots, the overall wrench $\mathbf{w}$ applied on the end effector (in terms of forces f and torques t) is the combined effect of cables forces $\boldsymbol{w}_c$ and external loading $\boldsymbol{w}_e$ (such as the gravitational force). The reasoning can be extended to the planar case for an external force different from the gravitational one if the plane is horizontal. Having assumed a point-mass end effector, no rotation can be imposed. Hence, for m cables and n degrees of freedom, the structure matrix $\mathbf{S}$ can be written as:

$$\mathbf{S}^{n\times m} = [\mathbf{u}_1, \mathbf{u}_2, \dots \mathbf{u}_m] \tag{4.3}$$

An aggregate formulation [14] of the dynamic equilibrium can be obtained by include the external wrench $\mathbf{w}_e$ in the structure matrix $\mathbf{S}$ as follows:

$$\mathbf{w} = \mathbf{w}_e + \mathbf{w}_e = \mathbf{w}_e + \mathbf{S}\boldsymbol{\tau} = [\mathbf{S}\mathbf{w}_e]\{\boldsymbol{\tau}; 1\} = \mathbf{S}_a\boldsymbol{\tau}_a \tag{4.4}$$

4.3.1 *Connecting Path*

The first step of the recovery strategy consists in changing the direction of motion of the end effector. In order to do so, the velocity component orthogonal to the desired direction of motion r (i.e., directed towards the safe point) must be reduced to a suitably small value. For simplicity, it is convenient to define a second ever-changing reference frame having the x-axis aligned with the direction of interest r. This new reference frame is described by a rotational matrix $\mathbf{R}_I(\alpha, \beta) = \mathbf{R}_z(\alpha)\mathbf{R}_y(\beta)$. It is now possible to refer the velocity vector to the second reference frame as:

$$\mathbf{v}' = [v'_x\ v'_y\ v'_z]^T = \mathbf{R}_I^T\mathbf{v} \tag{4.5}$$

A third rotation matrix $\mathbf{R}_{II}$ is applied such that the undesired velocity component lies along the y-axis. This third reference frame is described by the rotational matrix: $\mathbf{R}_{II} = \mathbf{R}_I(\alpha, \beta)\mathbf{R}_x(\gamma)$ where $where\ \gamma = atan\left(\frac{v'_z}{v'_y}\right)$

The velocity vector $v''$and the exerted force f'' in this new reference can be expressed as:

$$\mathbf{v}'' = \mathbf{R}_{II}^{T}\mathbf{v} = \begin{bmatrix} v_x'' \\ v_y'' \\ 0 \end{bmatrix}$$

$$\mathbf{f}'' = \begin{bmatrix} f_x'' \\ f_y'' \\ f_z'' \end{bmatrix} = \mathbf{R}_{II}^{T} \begin{bmatrix} f_x \\ f_y \\ f_z \end{bmatrix} = \mathbf{R}_{II}^{T}\mathbf{W}\boldsymbol{\tau}_w = \mathbf{W}_R\boldsymbol{\tau}_w = \begin{bmatrix} \mathbf{w}_{Rx}^{T} \\ \mathbf{w}_{Ry}^{T} \\ \mathbf{w}_{Rz}^{T} \end{bmatrix} \boldsymbol{\tau}_w \tag{4.6}$$

Fig. 4.10 shows in black the absolute reference frame and in blue the rotated one. The plane x''-y''(highlighted in yellow in Fig. 4.10) represents the plain in which the whole motion takes place. Such plane is identified by the velocity vector at the failure instant and the chosen Safe Point (XS). The plane of motion is pictured in Fig. 4.10 left where the velocity vector and the exerted force (with their projections on the Cartesian axes) are depicted with red and green arrows, respectively. In order to align the velocity vector with the desired direction of motion, v_y'' has to be reduced to a suitable small value. The maximum braking effect can be found by solving the optimization problem defined as follows:

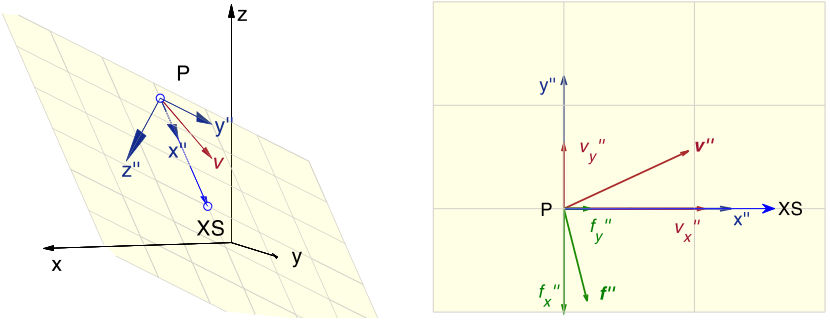

Figure 4.10: Plane of motion in the 3D space (left) and in the 2D space (right)

$$\begin{aligned} &maximize(-sgn(v_t) * f_t) = -sgn(v_t) * \mathbf{s}_t^{T}\boldsymbol{\tau} \\ &\text{s.t.} \begin{cases} \mathbf{s}_{Rx}^{T}\boldsymbol{\tau} \geqslant 0 \\ \mathbf{s}_{Rz}^{T}\boldsymbol{\tau} = 0 \\ \boldsymbol{\tau}_{min} \preceq \boldsymbol{\tau} \preceq \boldsymbol{\tau}_{max} \\ \tau_f = 0 \end{cases} \end{aligned} \tag{4.7}$$

where τ_f is the broken cable and $\boldsymbol{\tau}_{min}$ and $\boldsymbol{\tau}_{max}$ are the vectors containing the lower and upper bound for each cable tension. At each step, a new tension configuration is computed to generate the maxi-

mum braking effect on v_y'' until $|v_y''|$ reaches a suitable small value. When this condition holds, the velocity vector is directed towards the safe point and it is possible to perform a straight-line path along the desired direction of motion d.

4.3.2 *Straight Line Path*

Once the connecting path has been performed, it is possible to follow a straight-line path towards the safe point. This trajectory cannot be planned in advance since the initial position and velocity (i.e. motion status of the end-effector at the end of the connecting path) are not know a priori. The off-line analysis proposed for the planar manipulator is not easily expendable for the spatial case. However, the *WEC* index introduced in Chapter 3 can be exploited in order to find a range of feasible forces along the desired straight-line path. To minimize the computational time, the geometry based algorithm introduced in Chapter 3 can be implemented.

By finding the minimum exertable force in the direction defined by $\mathbf{v}$, it is possible to apply the maximum braking force aimed at stopping the end effector. If the end effector lies outside the residual SEW at the end of the connecting path, it may be possible that a braking force cannot be exerted; in this case, the minimum exertable force in the direction defined by $\mathbf{v}$ is the one that generates the minimum acceleration to lead the end effector towards the Safe Point. Once the end effector enters the residual SEW (i.e., it is possible to generate a force in any direction), an actual braking force can be exerted in order to arrest the end-effector. It is worth noticing that the end effector will not stop exactly in the Safe Point; in fact, the Safe Point is intended to identify a direction of motion not an exact landing location. The end effector will stop along the straight-line of motion, before or after the Safe Point depending on the velocity modulus and the force exertion capability in that configuration.

4.3.3 *Simulations*

The strategy described above is here applied to a point-mass suspended cable robot, with 4 cables and 3 translational degrees of freedom. The initial SEW is a cube with side dimension a = 2 m. The pulleys are located in the upper vertexes at height H=m. In this simulation it is assumed that a single cable brakes. Fig.4.11 (right) shows the top view of the workspace after failure, where the residual SEW is highlighted in gray. The origin of the reference frame is located in the vertex directly opposite from the one to which the failed cable is attached. In this simulation, the cable attached to vertex D fails, and hence the origin of the reference frame is located in B. In this scenario, the ordinates of the anchor points are: A (0;-a;0)

m, B(0;0;0)m, C(a;0;0)m and D (a;-a;0)m . The safe point has been chosen to obtain the maximum isotropy in terms of force exertion capability in the xy plane. Once that the xy coordinates are fixed ($x_S = 1 - \frac{\sqrt{3}}{3}, y_S = -1 + \frac{\sqrt{3}}{3}$), the z coordinate can be computed by maximizing the minimum guaranteed force in every direction. The results are depicted on the right of Fig.4.11 (right), where the minimum guaranteed force is plotted along the z axes, showing a maximum performance in z=-1.169m. Without lack of generality, the mass of the end-effector has been set to 1 kg and the lower and upper bounds for each cable tension have been set to 0.5N and 10N respectively.

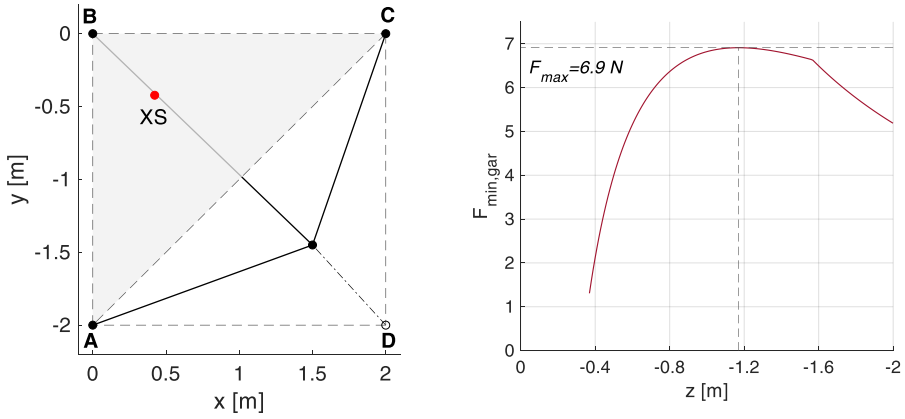

Figure 4.11: Top view of the residual SEW (left) and best z coordinate for XS (right)

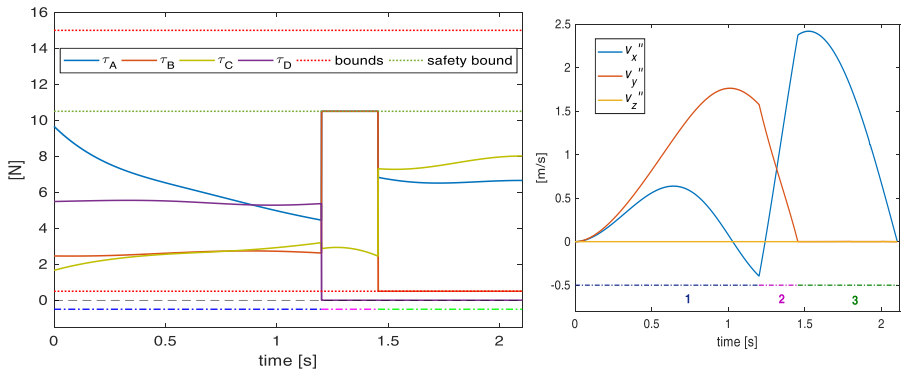

Figure 4.12: Cable tensions (left) and velocity vector in the rotate reference frame (right)

The failure is assumed to take place during a linear trajectory from the point $X_i = (0.4; -0.8; -0.5)m$ to the point $X_f = (1.7; -1; -1.6)m$ with a total trajectory time equal to T=1s. The cable attached to D is assumed to brake at time $t_f = 60\%T$. In this simulation, the condition to determine the end of the connecting path has been set equal to $v_y'' = 10^{-3} m/s$. Fig.4.12 (right) shows the components of $\mathbf{v}''$: it is worth noticing how the component v_y'' decreases during the connecting path. The overall path is shown in Fig.4.13, while the corre-

sponding tensions are plotted on the left of Fig.4.12 (left), showing that cable tensions are maintained positive and bounded during the whole trajectory. In both figures, the three motion phases are shown: the trajectory before failure (blue), the connecting path (magenta) and the straight-line path (green). Moreover, the plane of motion is highlighted in yellow in Fig.4.13.

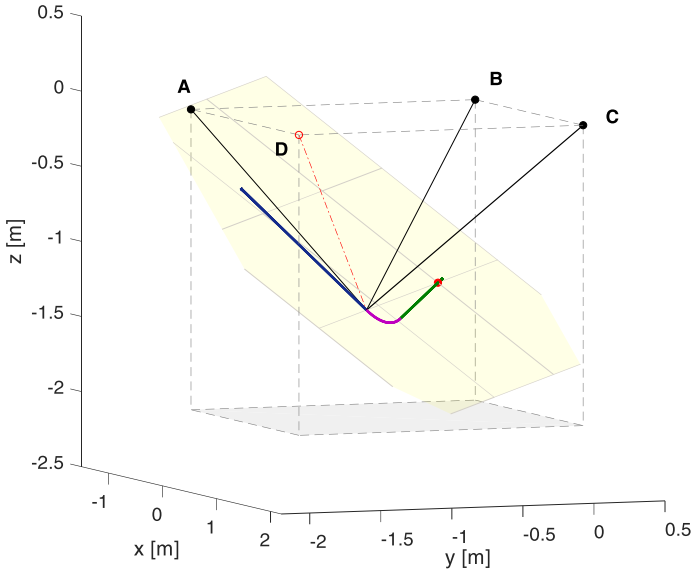

Figure 4.13: Path followed by the end effector

4.4 SUMMARY

This Chapter presented a novel approach to deal with cable failure. The strategy aims at leading the end effector towards a pre-computed safe point in a minimum time. In order to keep the path simple, the after failure trajectory is thought to be a straight line from the point where the failure take place to the chosen safe point. However, a connecting path is usually necessary to change the direction of motion of the end effector to align the velocity of the end effector to the desired linear path.

In this Chapter both planar and spatial configuration has been discussed. Regarding the linear trajectory planning, two different approaches has been proposed. The first one is based on an off-line analysis to compute precautionary force bounds that has to be considered when planning the linear path. Such approach has been described using a planar configuration example.

The second approach is based on the on-line computation of the *WEC* index proposed in Chapter 3. By computing at each iteration the maximum braking force, it is possible to stop the end effector along the straight line identified by the safe point. The on-line approach

has been presented for spatial configuration but can be easily adapt to planar ones (see the case study presented in Chapter 6).

In both cases the strategy has been proven to be effective in leading the end effector inside the residual workspace by keeping positive and bounded cable tensions during the whole time.

5

RECOVERY STRATEGY BASED ON PERIODIC TRAJECTORY

The strategy proposed in this Chapter, exploits dynamically feasible trajectories firstly presented in [29] and later used as after-failure recovery trajectories in [8]. Compared to previous works, however, a single elliptical trajectory is used to steer the end-effector from the failure point to a safe pose. Further, the safe pose is selected such that the resulting recovery trajectory is not only dynamically feasible (in terms of maximum and minimum cable tensions), but also collision-free, time-optimal, and such that continuity in the trajectory of the end-effector is guaranteed up to the first time derivative.

This Chapter focuses in particular on cable suspended camera systems. This choice is based on the fact that these devices are the most common application of cable robots nowadays. In principle, after the breakage of one cable has been detected by the control system, the intact cables can be simply retracted. This intuitive strategy alone, however, does not guarantee that the end effector follows a feasible trajectory, i.e., one that avoids collisions with the environment and for which cable tensions remain positive and below a safe value.

5.1 ROBOT ARCHITECTURE

Let us consider the 3-DoF cable-suspended device shown in Fig. 5.1. This system represents the simplified model of a cable-suspended camera wherein the end effector is a lumped mass m and the four cables are regarded as massless and infinitely rigid. The winches are attached to the vertexes of a rectangular layout, whose sides are h and l. All winches are located at a distance H from the ground, and the origin of the base reference frame coincides with A_2. Measurement errors are assumed negligible (i.e., position and velocity of the camera are exactly known from forward kinematics) and feasible cable tensions are limited between $\tau_{min} = 0$ and $\tau_{max} > 0$.

The focus of this chapter consists in planning feasible recovery trajectories following the failure of *one* cable. Without loss of generality, such cable is identified with cable 4. Fig. 5.2 shows a top view of the device in Fig. 5.1, where the shaded area indicates the footprint of the after-failure *SEW*. In this new scenario, the CDPR is fully constrained,

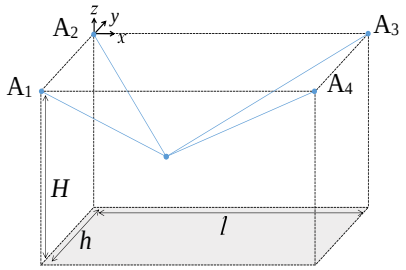

Figure 5.1: *SEW* before failure.

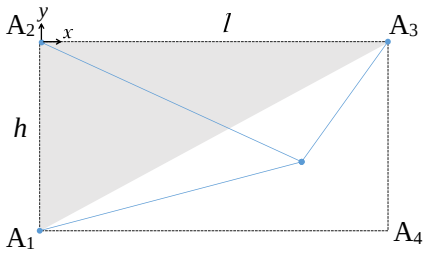

Figure 5.2: Top view of the *SEW* after failure.

with three cables controlling three DoFs. The dynamic equilibrium of the end effector can be written as:

$$\mathbf{S}\boldsymbol{\tau} + m\mathbf{g} = m\,\ddot{\mathbf{p}}, \tag{5.1}$$

where $\mathbf{S} = [\mathbf{u}_1, \mathbf{u}_2, \mathbf{u}_3] \in \mathbf{R}^{3\times3}$ is the so-called *structure matrix*, $\mathbf{u}_j$ is the unit vector along the direction of the j-th cable, pointing towards A_j, $\mathbf{g} = [0\ 0\ -g]^T$ is the gravity vector, $\boldsymbol{\tau} \in \mathbf{R}^{3\times1}$ is the vector of the cable tensions and $\ddot{\mathbf{p}} \in \mathbf{R}^{3\times1}$ is the acceleration of the end-effector, whose location is indicated as $\mathbf{p} = [x\ y\ z]^T$.

5.2 AFTER-FAILURE ELLIPTICAL TRAJECTORIES

When a cable breaks, a feasible recovering motion-law must be planned in real time to ensure positive and bounded cable tensions in the remaining active cables. To this end, globally feasible oscillatory trajectories are here exploited akin to those defined in [29], which have been proven to ensure positive cable tensions for any arbitrary amplitude, if a particular frequency ω_n is selected for the motion. In order to leverage this known result to obtain an appropriate failure recovery strategy, the end effector must lie on a sinusoidal periodic trajectory at $t = 0$, the instant of failure.

The simplest periodic trajectory that guarantees continuity of position and velocity at $t = 0$ is an elliptical trajectory in the form [44]:

$$\begin{bmatrix} x(t) \\ y(t) \\ z(t) \end{bmatrix} = \begin{bmatrix} x_c \\ y_c \\ z_c \end{bmatrix} + \begin{bmatrix} r_x \\ r_y \\ r_z \end{bmatrix} \sin\left(\omega_n t + \begin{bmatrix} \alpha_x \\ \alpha_y \\ \alpha_z \end{bmatrix}\right) \tag{5.2}$$

The centre of the ellipse $\mathbf{p}_c = [x_c \; y_c \; z_c]^T$ is the safe landing location where to steer the end effector, which must be chosen within the after-failure *SEW* and above the ground. The sinusoidal motion is defined by the amplitude vector $\mathbf{r} = [r_x \; r_y \; r_z]^T$, frequency ω_n, and phase angles $\boldsymbol{\alpha} = [\alpha_x \; \alpha_y \; \alpha_z]^T$. It can be proven that by selecting ω_n to be the natural frequency $\omega_n = \sqrt{-g/z_c}$, arbitrarily large amplitudes can be performed while ensuring positive tensions [29].

The end effector position and velocity at the instant of failure are $\mathbf{p}_f = [x_f \; y_f \; z_f]^T$ and $\dot{\mathbf{p}}_f = [\dot{x}_f \; \dot{y}_f \; \dot{z}_f]^T$, respectively. If the failure is detected with some delay, then $t = 0$, $\mathbf{p}_f$, $\dot{\mathbf{p}}_f$ indicate the time instant when a failure is *detected*, and the corresponding position and velocity of the end-effector. By imposing the conditions of continuity in position and velocity at $t = 0$, it is possible to find the elements of $\mathbf{r}$ as follows:

$$\begin{aligned} r_x &= \sqrt{\bar{x}_f^2 + (x_c - x_f)^2} \\ r_y &= \sqrt{\bar{y}_f^2 + (y_c - y_f)^2} \\ r_z &= \sqrt{\bar{z}_f^2 + (z_c - z_f)^2} \end{aligned} \tag{5.3}$$

where:

$$\begin{aligned} \bar{x}_f &= \tfrac{\dot{x}_f}{\omega_n} \\ \bar{y}_f &= \tfrac{\dot{y}_f}{\omega_n} \\ \bar{z}_f &= \tfrac{\dot{z}_f}{\omega_n} \end{aligned} \tag{5.4}$$

Then, the elements of $\boldsymbol{\alpha}$ are derived as

$$\begin{aligned} \alpha_x &= \operatorname{atan2}(\tfrac{x_f - x_c}{r_x}, \frac{\bar{x}_f}{r_x}) \\ \alpha_y &= \operatorname{atan2}(\tfrac{y_f - y_c}{r_y}, \frac{\bar{y}_f}{r_y}) \\ \alpha_z &= \operatorname{atan2}(\tfrac{z_f - z_c}{r_z}, \frac{\bar{z}_f}{r_z}) \end{aligned} \tag{5.5}$$

Once the elliptical trajectory has been defined, a fifth order polynomial-law $U(\varphi)$ [29] is added in order to progressively decrease the ampli-

tude of the oscillation and steer the end-effector to the safe location $\mathbf{p}_c$:

$$\begin{bmatrix} x(t) \\ y(t) \\ z(t) \end{bmatrix} = \begin{bmatrix} x_c \\ y_c \\ z_c \end{bmatrix} + U(\varphi) \begin{bmatrix} r_x \\ r_y \\ r_z \end{bmatrix} \sin\left(\omega_n t + \begin{bmatrix} \alpha_x \\ \alpha_y \\ \alpha_z \end{bmatrix}\right) \tag{5.6}$$

Here, φ is the normalized time parameter $\varphi = (1 - t/T)$ and T represents the time required to perform the recovery motion from $\mathbf{p}_f$ to $\mathbf{p}_c$. The coefficients of $U(\varphi)$ are chosen such that the amplitude is maximum at $t = 0$ and null at $t = T$, and the landing location $\mathbf{p}_c$ is reached with zero velocity and acceleration at $t = T$:

$$\begin{aligned} &U(0) = 0, \quad U(1) = 1, \\ &\dot{U}(0) = \dot{U}(1) = \ddot{U}(0) = \ddot{U}(1) = 0. \end{aligned} \tag{5.7}$$

These conditions lead to the following time law[29]:

$$U(\varphi) = 6\varphi^5 - 15\varphi^4 + 10\varphi^3. \tag{5.8}$$

5.2.1 *Tension constraints for the elliptical recovery trajectory*

To ensure that a trajectory is feasible, each tension τ_j must comply with:

$$0 < \tau_j < \tau_{max}, \text{ for } j = 1, 2, 3 \tag{5.9}$$

By using the definition of *pseudo-tension*, first introduced in [29], τ_j can be rewritten as

$$\tau_j = \frac{-k_j \, m \, \rho_j}{h \, l \, z}, \tag{5.10}$$

where ρ_j is the length of the cable attached to A_j and k_j is the j-th pseudo-tension. For the device shown in Fig. 5.2, the pseudo-tensions are:

$$\begin{aligned} k_1 &= \ddot{y} l z - l y (\ddot{z} + g) \\ k_2 &= (\ddot{z} + g)(hl - hx + ly) - \ddot{y} l z + \ddot{x} h z \\ k_3 &= hx(\ddot{z} + g) - \ddot{x} h z. \end{aligned} \tag{5.11}$$

Further, for all points below the plane of the pulleys, conditions (5.9) can be equivalently rewritten as

$$0 < k_j < \frac{h l \tau_{max} \cos\beta_j}{m}, \quad \text{for } j = 1, 2, 3, \tag{5.12}$$

where $\beta_j = \cos^{-1}\left(-\rho_j / z\right)$ is the inclination of the *j-th* cable. The upper bound in (5.12) is position-dependent, but can be simplified by setting an appropriate maximum height z_{max} that the end-effector is allowed to reach or, equivalently, a worst-case inclination angle β_{max},

the derivation of which is described in Section 5.3.2. This leads to the following *sufficient* conditions:

$$0 < k_j < \frac{hl\tau_{max}\cos\beta_{max}}{m}, \quad \text{for } j = 1,2,3, \tag{5.13}$$

which will be used in place of (5.12) in the following sections.

5.2.2 *Minimum time for the elliptical recovery trajectory*

The trajectory in (5.6) and its time derivatives are substituted into (5.11) to find the general constraints for the elliptical trajectory [44]:

$$k_j = F_{j1} + UF_{j2}\omega_n^2 + \frac{2\dot{U}\omega_n}{T}(F_{j3} + UF_{j4}) + \frac{\ddot{U}}{T^2}F_{j5}, \quad j = 1,2,3 \tag{5.14}$$

where:

$$\begin{aligned}
F_{11} &= -gly_c;\\
F_{12} &= lr_z y_c \sin(\omega_n t + \alpha_z);\\
F_{13} &= lr_y z_c \cos(\omega_n t + \alpha_y) - r_z y_c l\cos(\omega_n t + \alpha_z);\\
F_{14} &= -lr_y r_z \sin(\alpha_y - \alpha_z);\\
F_{15} &= lr_y z_c \sin(\omega_n t + \alpha_y) - lr_z y_c \sin(\omega_n t + \alpha_z));\\
\\
F_{21} &= -F_{11} - F_{31} + ghl;\\
F_{22} &= -F_{12} - F_{32} - hlr_z \sin(\omega_n t + \alpha_z);\\
F_{23} &= -F_{13} - F_{33} + hlr_z \sin(\omega_n t + \alpha_z);\\
F_{24} &= -F_{14} - F_{34};\\
F_{25} &= -F_{15} - F_{35} + hlr_z \sin(\omega_n t + \alpha_z);\\
\\
F_{31} &= ghx_c;\\
F_{32} &= -hr_z x_c \sin(\omega_n t + \alpha_z);\\
F_{33} &= -hr_x z_c \cos(\omega_n t + \alpha_x) + r_z x_c h\cos(\omega_n t + \alpha_z);\\
F_{34} &= hr_x r_z \sin(\alpha_x - \alpha_z);\\
F_{35} &= -hr_x z_c \sin(\omega_n t + \alpha_x) + hr_z x_c \sin(\omega_n t + \alpha_z)).
\end{aligned} \tag{5.15}$$

To ensure that all cable tensions are feasible over the trajectory, each pseudo-tension k_j must satisfy (5.13) for $t \in [0, T]$. The lower bound in (5.13) is equivalent to imposing that the minimum value of k_j over $[0, T]$ must be non negative. Similarly, its maximum value must be lower than the upper bound in (5.13). From (5.3) and (5.5), it is clear that the parameters $\mathbf{r}$ and $\boldsymbol{\alpha}$ are functions of the failure state $(\mathbf{p}_f\ ,\ \dot{\mathbf{p}}_f)$ and of the landing point $\mathbf{p}_c$ (indeed, ω_n depends solely on z_c). Hence, if the position and velocity of the end-effector at the instant of failure are known, (5.14) depends on the coordinates of the safe location $\mathbf{p}_c$ and on the trajectory time T. If the safe location is fixed, it is possible to numerically compute the minimum and maximum values that each

k_j takes in $[0, T]$. The scalar functions q_j and q_j^* representing these values are defined as:

$$q_j\big|_{\mathbf{p}_f, \dot{\mathbf{p}}_f}(T) = \min_{t \in [0,\, T]} \left(k_j\left(\mathbf{p}_f,\, \dot{\mathbf{p}}_f,\, T,\, t\right)\right), \text{ for } j = 1, 2, 3 \tag{5.16a}$$

$$q_j^*\Big|_{\mathbf{p}_f, \dot{\mathbf{p}}_f}(T) = \max_{t \in [0,\, T]} \left(k_j\left(\mathbf{p}_f,\, \dot{\mathbf{p}}_f,\, T,\, t\right)\right), \text{ for } j = 1, 2, 3. \tag{5.16b}$$

These functions are shown in Fig. 5.3 for a representative design and illustrative failure conditions.

To ensure that each pseudo-tension k_j is kept positive and bounded in the whole trajectory for a chosen trajectory time T, it would be sufficient to check that $q_j(T)$ and $q_j^*(T)$ comply with the the lower and upper bounds of (5.13), respectively. However, as noted in [44], available numerical methods to solve (5.16a) and (5.16b) are not suitable for real-time applications. Thus, interval mathematics can be applied to find the minimum and maximum values that the pseudo-tension k_j can possibly take in $[0, T]$, which leads to time-independent functions that approximate (5.16). In the interval $[0, T]$, (5.14) takes its extreme values for $U = 1$; $\dot{U} = 15/8$; $\ddot{U} = (10\sqrt{3})/3$. Moreover, considering that the trigonometric functions sine and cosine are bounded, the minimum and maximum value that k_j can possibly take are given by

$$e_j(T) = a_j + \frac{b_j}{T} + \frac{c_j}{T^2}, \text{ for } j = 1, 2, 3, \tag{5.17a}$$

$$e_j^*(T) = a_j^* + \frac{b_j^*}{T} + \frac{c_j^*}{T^2}, \text{ for } j = 1, 2, 3, \tag{5.17b}$$

where $e_j(T)$ and $e_j^*(T)$ represent conservative lower and upper bounds for k_j.The coefficients are:

$$
\begin{aligned}
a_1 &= -gly_c + lr_z\omega_n^2 y_c \\
b_1 &= 2\omega_n \frac{15l}{8}(r_y z_c + r_z y_c - r_y r_z) \\
c_1 &= \frac{10\sqrt{3}}{3} l(r_y z_c + r_z y_c) \\
a_1^* &= -gly_c - lr_z\omega_n^2 y_c \\
b_1^* &= -b_1 \\
c_1^* &= -c_1
\end{aligned}
$$

$$
\begin{aligned}
a_2 &= -a_1 - a_3 + ghl + lr_z\omega_n^2 y_c - hr_z x_c\omega_n^2 \\
b_2 &= b_1 + b_3 - 2\omega_n \frac{15l}{8} hlr_z \\
c_1 &= c_1 + c_3 - \frac{10\sqrt{3}}{3} hlr_z \\
a_2^* &= -gly_c + ghx_c + ghl - lr_z y_c\omega_n^2 + hr_z x_c\omega_n^2 + hlr_z \\
b_2^* &= -b_2 \\
c_2^* &= -c_2
\end{aligned}
\tag{5.18}
$$

$$
\begin{aligned}
a_3 &= -a_1 - a_3 + ghl + lr_z\omega_n^2 y_c - hr_z x_c\omega_n^2 \\
b_3 &= 2\omega_n \frac{15l}{8}(r_x z_c - r_z x_c - r_x r_z) \\
c_3 &= \frac{10\sqrt{3}}{3} l(r_x z_c - r_z x_c) \\
a_3^* &= ghx_c + hr_z x_c\omega_n^2 \\
b_3^* &= -b_3 \\
c_3^* &= -c_3
\end{aligned}
$$

As stated in [29], it is always possible to find a large enough T such that $e_j > 0$, indeed

$$
\lim_{T\to+\infty} e_j(T) = a_j, \tag{5.19}
$$

and it can be proved that each a_j is positive if the trajectory stays below the pulley's plane as follows:

1. $a_1 > 0 \Leftrightarrow -gly_c + lr_z\omega_n^2 y_c > 0$. Given that X_C belongs to the new *SEW* (i.e., $y_c < 0$) and that $\omega_n = \sqrt{-g/z_c}$, the previous condition can be written as $r_z < -z_c$.

2. $a_2 > 0 \Leftrightarrow g(hl + ly_c - hx_c) - r_z\omega_n^2(hl + ly_c - hx_c) > 0$. As above, if X_c belongs to the new *SEW* (i.e., $hl + ly_c - hx_c > 0$), the previous condition yields $r_z < -z_c$

3. $a_3 > 0 \Leftrightarrow ghx_c - hr_z\omega_n^2 x_c > 0$. Again, if X_C belongs to the new *SEW* (i.e., $x_c > 0$), this condition leads to $r_z > -z_c$.

Moreover, by studying the sign of c_j, one can further determine the behavior of e_j as it approaches 0, indeed:

1. $c_1 > 0 \Leftrightarrow r_y z_c + r_z y_c > 0$. Given that z_c and y_c are negative by definition, the previous condition is always false and hence $c_1 < 0$.

2. $c_3 > 0 \Leftrightarrow r_x z_c - r_z x_c > 0$. Given that x_c is positive and z_c is negative by definition, the previous condition is always false and hence $c_3 < 0$.

3. $c_2 > 0 \Leftrightarrow -r_z(ly_c - hx_c + hl) + z_c(lr_y + hr_x) > 0$. Given that $z_c < 0$ and $(ly_c - hx_c + hl) > 0$ when the landing location $\mathbf{p}_c$ is inside the new *SEW*, the previous condition is always false proving that $c_2 < 0$.

Because c_1, c_2, and c_3 are negative, we conclude the following:

$$\lim_{T \to 0^+} e_j(T) = \text{sign}(c_j) \cdot \infty = -\infty. \tag{5.20}$$

Given (5.19) and (5.20), it is clear that function e_j intersects the x-axis at least once. Moreover, by studying the derivative of e_j

$$\frac{de_j}{dT} = -\frac{2c_j + b_j T}{T^3}, \tag{5.21}$$

it can be easily inferred that e_j is monotonic for $T > 0$ and hence this intersection is *unique*. In summary, e_j must intersect the axis $y = 0$ only one time, and hence finding the zero $e_j = 0$ yields the (conservative) minimum feasible time that ensures positive tension in the j-th cable.

Similarly, the limit at infinity for $e_j^*(T)$ is:

$$\lim_{T \to +\infty} e_j^*(T) = a_j^* \tag{5.22}$$

Thus, to ensure that $e_j^*(T)$ complies with the upper bound of (5.13) for a large enough T, it must be $a_j^* < \frac{hl\tau_{max}\cos\beta_{max}}{m}$. This condition leads to the following constraints on $\mathbf{p}_c$:

$$a_1^* = -gly_c\left(1 - \frac{r_z}{z_c}\right) \leqslant \frac{hl\tau_{max}\cos\beta_{max}}{m} \tag{5.23a}$$

$$a_2^* = g\left(1 - \frac{r_z}{z_c}\right)(hl - hx_c + ly_c) \leqslant \frac{hl\tau_{max}\cos\beta_{max}}{m} \tag{5.23b}$$

$$a_3^* = ghx_c\left(1 - \frac{r_z}{z_c}\right) \leqslant \frac{hl\tau_{max}\cos\beta_{max}}{m} \tag{5.23c}$$

Because $1 < \left(1 - \frac{r_z}{z_c}\right) < 2$, conservative estimates of (5.23) lead to the following constraints on x_c and y_c:

$$y_c > y^*_{c,l}, \quad \text{with} \quad y^*_{c,l} = -\frac{h\tau_{max}\cos\beta_{max}}{2mg} \tag{5.24a}$$

$$ly_c - hx_c + hl < \frac{hl\tau_{max}\cos\beta_{max}}{2mg} \tag{5.24b}$$

$$x_c < x^*_{c,u}, \quad \text{with} \quad x^*_{c,u} = \frac{l\tau_{max}\cos\beta_{max}}{2mg} \tag{5.24c}$$

Moreover, following a reasoning similar to the one done for e_j, it is possible to determine the behavior of e^*_j as it approaches 0. Because $c^*_j = -c_j$, we conclude that:

$$\lim_{T\to 0^+} e^*_j(T) = sign(c^*_j)\cdot\infty = +\infty. \tag{5.25}$$

Given (5.22) and (5.23), it is clear that function e^*_j intersects the axis $y = \frac{hl\tau_{max}\cos\beta_{max}}{m}$ at least once. Again, by studying the derivative of e^*_j, one can easily prove that e^*_j is monotonic and hence this intersection is unique. Thus, finding the condition $e^*_j = \frac{hl\tau_{max}\cos(\beta_{max})}{mg}$ yields the (conservative) minimum feasible time.

It has been proved that $e_j(T)$ and $e^*_j(T)$ intersect the lower and upper bound of (5.13) only once, which are the positive solutions of the following equations:

$$a_j T^2 + b_j T + c_j = 0, \tag{5.26a}$$

$$\left(a^*_j - \frac{hl\tau_{max}\cos\beta_{max}}{m}\right) T^2 + b^*_j T + c^*_j = 0, \tag{5.26b}$$

Such solutions yield $T_{min,j}$ and $T^*_{min,j}$, approximations of the minimum trajectory time required to ensure positive and bounded cable tensions in cable *j*, respectively. An example of these approximations for cable 1 is illustrated in Fig. 5.3 .

To ensure that all cables comply with the tension constraints (5.13) during the recovery trajectory, T is chosen as follows:

$$T_{min} = \max\left\{T_{min_1}, T_{min_2}, T_{min_3}, T^*_{min_1}, T^*_{min_2}, T^*_{min_3}\right\}. \tag{5.27}$$

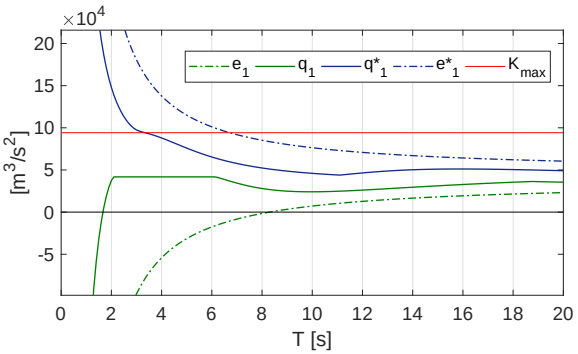

Figure 5.3: functions q_1, q_1^* and e_1, e_1^* corresponding to the following parameters: $l = 120m$, $h = 80m$, $H = 30m$, $\mathbf{p}_c = [12.3 \ -35.5 \ -16.4]^T m$, $\mathbf{p}_f = [19.6 \ -70.5 \ -16.8]^T m$ and $\dot{\mathbf{p}}_f = [-7.67 \ -4.5 \ 1.5]^T m/s$, $\tau_{max} = 12kN$ and $m = 30kg$.

5.3 FEASIBILITY OF THE ELLIPTICAL RECOVERY TRAJECTORY

The choice of the safe landing location inside the after-failure *SEW* affects the amplitude of the elliptical trajectory, the natural frequency of the system, and the minimum trajectory time (5.27) that ensures positive and bounded cable tensions. Proper limits on the amplitudes r_x, r_y and r_z must be imposed in order to: (i) keep the end-effector inside the pre-failure *SEW* and above the ground, thereby avoiding further damage, such as collisions with the physical boundaries of the workspace; (ii) ensure bounded cable tensions. The following two sections will discuss the existence of a feasible region Γ for the safe landing location $\mathbf{p}_c$, which guarantees both (i) and (ii).

5.3.1 *Collision-free path*

The following *sufficient* conditions ensure that the trajectory in (5.6) lie inside a feasible rectangular cuboid, i.e., the region of the pre-failure *SEW* included below z_{max} and above the ground:

$$(0 < x_c - r_x) \wedge (x_c + r_x < l) \tag{5.28a}$$

$$(-h < y_c - r_y) \wedge (y_c + r_y < 0) \tag{5.28b}$$

$$(-H < z_c - r_z) \wedge (z_c + r_z < z_{max}). \tag{5.28c}$$

To obtain more conservative constraints, arbitrary safety margins can be optionally added to (5.28). In (5.28a), for example, the lower and upper bounds 0 and l can be substituted with dl and $(l - dl)$, respectively, with $dl > 0$ being a desired safety margin.

Given that the parameters $\mathbf{p}_f$ and $\dot{\mathbf{p}}_f$ are fixed, it can be easily inferred from (5.3) that the amplitudes r_x, r_y and r_z are only functions of the coordinates $\mathbf{p}_c$. Hence, equations (5.28) can be rewritten in order to obtain general conditions for x_c, y_c and z_c. For example, conditions (5.28a) and (5.28b), which set boundaries on x_c and y_c, are rewritten as:

$$x_{c,l} < x_c < x_{c,u}, \text{ with } x_{c,l} = \frac{\bar{x}_f^2 + x_f^2}{2x_f},\ x_{c,u} = \frac{l^2 - \bar{x}_f^2 - x_f^2}{2(l - x_f)}, \tag{5.29a}$$

$$y_{c,l} < y_c < y_{c,u}, \text{ with } y_{c,l} = \frac{\bar{y}_f^2 + y_f^2 - h^2}{2(h + y_f)},\ y_{c,u} = \frac{\bar{y}_f^2 + y_f^2}{2y_f}. \tag{5.29b}$$

A feasible interval for x_c exists only if the upper bound in (5.29a) exceeds the corresponding lower bound. By imposing this condition, it is possible to find a feasible range for $\bar{x}_f$. The same reasoning can be applied to y_c and z_c to find similar conditions on $\bar{y}_f$ and $\bar{z}_f$:

$$\begin{aligned} \bar{x}_f^2 &< x_f\,(l - x_f) \\ \bar{y}_f^2 &< -y_f\,(h + y_f) \\ \bar{z}_f^2 &< -\,(z_f - z_{max})\,(H + z_f)\,. \end{aligned} \tag{5.30}$$

These inequalities lead to a lower limit for ω_n that must be satisfied to guarantee the existence of a feasible region for $\mathbf{p}_c$:

$$\omega_n^2 > \max\left\{ \frac{\dot{x}_f^2}{x_f(l - x_f)},\ \frac{-\dot{y}_f^2}{y_f(h + y_f)},\ \frac{-\dot{z}_f^2}{(z_f - z_{max})(H + z_f)} \right\}. \tag{5.31}$$

Not all the ω_n given by (5.31) yield a feasible elliptical trajectory, i.e., one that does not exceed the boundaries (5.28). To enforce this condition, we use (5.28c), which can be rewritten in terms of ω_n as:

$$-\frac{2g(z_f + H) + \dot{z}_f^2}{z_f^2 - H^2} < \omega_n^2 < -\frac{2g(z_f - z_{max}) + \dot{z}_f^2}{z_f^2 - z_{max}^2}. \tag{5.32}$$

This holds because there exists a one-to-one relationship between z_c and ω_n. The overall constraints on ω_n are therefore:

$$\begin{aligned} \omega_{n,min}^2 = \max\Bigg\{ &\frac{\dot{x}_f^2}{x_f(l - x_f)},\ \frac{-\dot{y}_f^2}{y_f(h + y_f)}, \\ &\frac{-\dot{z}_f^2}{(z_f - z_{max})\,(H + z_f)},\ -\frac{2g(z_f + H)\dot{z}_f^2}{z_f^2 - H^2} \Bigg\} \end{aligned} \tag{5.33a}$$

$$\omega_{n,max}^2 = -\frac{2g(z_f - z_{max}) + \dot{z}_f^2}{z_f^2 - z_{max}^2}. \tag{5.33b}$$

$$\omega_{n,max}^2 \geqslant \omega_{n,min}^2. \tag{5.33c}$$

Based on (5.33), we now derive *sufficient* conditions for a feasible range of ω_n to exist. Constraints (5.33) can be used to derive sufficient conditions on the norm of the failure velocity $v_f = \|\dot{\mathbf{p}}_f\|$, as a function of the point of failure $\mathbf{p}_f$. To evaluate v_f, polar coordinates are introduced and the failure velocity components are rewritten as: $\dot{x}_f = v_f \sin\phi\cos\vartheta$, $\dot{y}_f = v_f \sin\phi\sin\vartheta$ and $\dot{z}_f = v_f\cos\phi$. Condition (5.33a) leads to four possible cases, but only 3 of them are feasible. By imposing (5.33c) in each one of these cases, it is possible to derive $v_{f,max}$, the maximum v_f that can be accommodated in any direction using a feasible elliptical trajectory. Specifically, a scalar function $\mathbb{R}^3 \to \mathbb{R}$ can be derived which indicates, for any failure point $\mathbf{p}_f$, the magnitude of the maximum failure velocity that can be accommodated in *any* direction using an elliptical trajectory. The pre-failure *SEW* is split into 4 regions, each corresponding to one $\omega_{n,min}$ in (5.33a). The four case are discussed below.

- **Case A:** $\omega_{n,min}^2 = \frac{\dot{x}_f^2}{x_f(l-x_f)}$

  Condition (5.33c) is rewritten as: $\frac{v_f^2(\sin\phi\cos\vartheta)^2}{x_f(l-x_f)} + \frac{2g}{z_f+z_{max}} + \frac{v_f^2\cos^2\phi}{z_f^2-z_{max}^2} < 0$. Let us indicate the sum of the coefficients of the velocity-dependent terms as: $s = \frac{(\sin\phi\cos\vartheta)^2}{x_f(l-x_f)} + \frac{\cos^2\phi}{z_f^2-z_{max}^2}$. The maximum values s can take are $s_{max,1} = \frac{1}{z_f^2-z_{max}^2}$, $s_{max,2} = \frac{1}{x_f(l-x_f)}$, which yield two possible values for $v_{f,max}$:
  Case A.1: $v_{f,max}^2 = -2g(z_f-z_{max})$, for $z_f^2 + x_f^2 - lx_f - z_{max}^2 < 0$
  Case A.2: $v_{f,max}^2 = \frac{-2gx_f(l-x_f)}{z_f+z_{max}}$, for $z_f^2 + x_f^2 - lx_f - z_{max}^2 \geqslant 0$
  The two cases are delimited by a half-cylinder with radius $r = \sqrt{z_{max}^2 + l^2/4}$ and axis parallel to the y axis: $\mathbf{a}_A = [r\ \beta\ 0]^T$, $\beta \in \mathbb{R}$, as shown in Fig. 5.4.

- **Case B:** $\omega_{n,min}^2 = -\frac{\dot{y}_f^2}{y_f(h+y_f)}$

  Condition (5.33c) is rewritten as: $-\frac{v_f^2(\sin\phi\sin\vartheta)^2}{y_f(h+y_f)} + \frac{2g}{z_f+z_{max}} + \frac{v_f^2\cos^2\phi}{z_f^2-z_{max}^2} < 0$. The sum of the coefficients of the velocity-dependent terms for this case is: $s = -\frac{(\sin\phi\sin\vartheta)^2}{y_f(h+y_f)} + \frac{\cos^2\phi}{z_f^2-z_{max}^2}$. The maximum values s can take are $s_{max,1} = \frac{1}{z_f^2-z_{max}^2}$, $s_{max,2} = \frac{-1}{y_f(h+y_f)}$, which yield these possible values of $v_{f,max}$:
  Case B.1: $v_{f,max}^2 = -2g(z_f-z_{max})$, for $z_f^2 + y_f^2 + hy_f - z_{max}^2 < 0$
  Case B.2: $v_{f,max}^2 = \frac{2gy_f(h+y_f)}{z_f+z_{max}}$, for $z_f^2 + y_f^2 + hy_f - z_{max}^2 \geqslant 0$
  These two cases are delimited by a half-cylinder with radius $r = \sqrt{z_{max}^2 + h^2/4}$ and axis parallel to the x axis: $\mathbf{a}_B = [\beta\ -r\ 0]^T$, $\beta \in \mathbb{R}$, as shown in Fig. 5.4.

- **Case C:** $\omega_{n,min}^2 = -\frac{\dot{z}_f^2+2g(z_f+H)}{z_f^2-H^2}$

  Condition (5.33c) is rewritten as: $-\frac{v_f^2\cos^2\phi}{z_f^2-H^2} - \frac{2g}{z_f-H} + \frac{2g}{z_f+z_{max}} + \frac{v_f^2\cos^2\phi}{z_f^2-z_{max}^2} < 0$. The sum of the coefficients of the velocity-dependent

terms for this case is: $s = -\frac{\cos^2\phi}{z_f^2-H^2} + \frac{\cos^2\phi}{z_f^2-z_{max}^2}$. The maximum value s can take is $s_{max} = \frac{H^2-z_{max}^2}{(z_f^2-z_{max}^2)(H^2-z_f^2)}$, which leads to: $v_{f,max}^2 = -\frac{2g(z_f-z_{max})(H+z_f)}{H-z_{max}}$.

- **Case D:** $\omega_{n,min}^2 = \frac{-\dot{z}_f^2}{(z_f-z_{max})(H+z_f)}$
  For $\dot{z}_f^2 < v_{f,max}^2$, the following must hold: $-\frac{\dot{z}_f^2}{(z_f-z_{max})(z_f+H)} < -\frac{\dot{z}^2+2g(z_f+H)}{z_f^2-H^2}$. Hence, $\omega_{n,min}^2 \neq \frac{-\dot{z}_f^2}{(z_f-z_{amx})(H+z_f)}$ and we conclude that case D is not possible.

Moreover, since $-2g(z_f - z_{max}) > \frac{-2g(z_f-z_{max})(z_f+H)}{H-z_{max}}$, there are only 3 possible values for the maximum velocity, namely

$$\begin{aligned} v_{fx,lim}^2 &= \tfrac{-2gx_f(l-x_f)}{z_f+z_{max}} \\ v_{fy,lim}^2 &= \tfrac{2gy_f(h+y_f)}{z_f+z_{max}} \\ v_{fz,lim}^2 &= -\tfrac{2g(z_f-z_{max})(H+z_f)}{H-z_{max}}, \end{aligned} \tag{5.34}$$

which correspond to case A.2, B.2 and C, respectively.

For any given horizontal plane $z_f = k$, it is straightforward to find the regions of this plane wherein each of the limit velocities above is the maximum velocity. The region wherein $v_{fz,lim}^2$ is the maximum velocity is a rectangular interval (blue region in Fig. 5.5) delimited by:

$$\begin{aligned} x &= \tfrac{l}{2} \pm \sqrt{\tfrac{l^2}{4} - \tfrac{(z_f^2-z_{max}^2)(z_f+H)}{H-z_{max}}} \\ y &= -\tfrac{h}{2} \pm \sqrt{\tfrac{h^2}{4} - \tfrac{(z_f^2-z_{max}^2)(z_f+H)}{H-z_{max}}} \end{aligned} \tag{5.35}$$

The regions where $v_{fx,lim}$ and $v_{fy,lim}$ are maximum (i.e., red and green regions in Fig. 5.5, respectively) are external to the above interval and are delimited by the following hyperbola:

$$\left(x_f - \tfrac{l}{2}\right)^2 - \left(y_f + \tfrac{h}{2}\right)^2 = \tfrac{l^2}{4} - \tfrac{h^2}{4} \tag{5.36}$$

By studying the values of $v_{f,max}$ across the workspace, it is possible to gain a better understanding of its trend. Four regions can be highlighted: they are delimited by two half-cylinders, namely Ω_x : $z = -\sqrt{lx - x^2 + z_{max}^2}$ and $\Omega_y : z = -\sqrt{-hy - y^2 + z_{max}^2}$, and can be described as follows:

1. Region Υ_z: If $\mathbf{p}_f$ is inside the two half cylinders (i.e., $z < -\sqrt{lx - x^2 + z_{max}^2} \wedge z < -\sqrt{-hy - y^2 + z_{max}^2}$), then $v_{f,max} = v_{fz,lim}$.

2. Region Υ_{yz}: If $\mathbf{p}_f$ is inside Ω_x but outside Ω_y (i.e., $z < -\sqrt{lx - x^2 + z_{max}^2} \wedge z > -\sqrt{-hy - y^2 + z_{max}^2}$), then $v_{f,max} = \min\{v_{fz,lim}, v_{fy,lim}\}$.

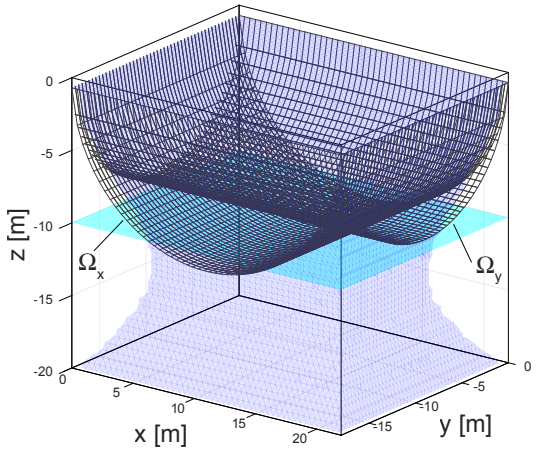

Figure 5.4: Shown in blue is the region of the *SEW* where $v_{f,max} = v_{fz,lim}$ for a representative CDPR. The half-cylinders represent the regions Ω_x and Ω_y

3. Region Υ_{xz}: If $\mathbf{p}_f$ is inside Ω_y but outside Ω_x, then $v_{f,max} = \min\{v_{fz,lim}, v_{fx,lim}\}$.

4. Region Υ_{xyz}: If $\mathbf{p}_f$ is outside both Ω_x and Ω_y, then $v_{f,max} = \min\{v_{fx,lim}, v_{fy,lim}, v_{fz,lim}\}$.

Figure 5.4 shows the region where $v_{f,max} = v_{fz,lim}$ (blue region in the plot) for a representative CDPR. The same figure also shows the two half-cylinders Ω_x and Ω_y. For any given horizontal plane $z_f = k$, it is possible to determine the regions wherein each of the limit velocities is the maximum velocity. For example, Fig. 5.5 shows the distribution of the limit velocity for the plane $z_f = -10m$, which is shown in cyan in Fig 5.4. Here, the blue area represents the region where $v_{f,max} = v_{fz,lim}$. It is worth noting that within this area the magnitude of $v_{f,max}$ remains constant. The red and green areas represent the regions wherein $v_{f,max} = v_{fx,lim}$ and $v_{f,max} = v_{fy,lim}$, respectively. The magnitude of $v_{f,max}$ varies throughout the red and green areas, as indicated by the isolines in Fig. 5.5.

In summary, if v_f is within the value of $v_{f,max}$ in the failure point $\mathbf{p}_f$, then the existence of an elliptical recovery trajectory that lies in the feasible rectangular cuboid (5.28) is guaranteed. However, if the above condition does not hold, a feasible elliptical trajectory might not exist, and transition trajectories must be planned to steer the end-effector to a different “failure" state, where a feasible elliptical trajectory exists.

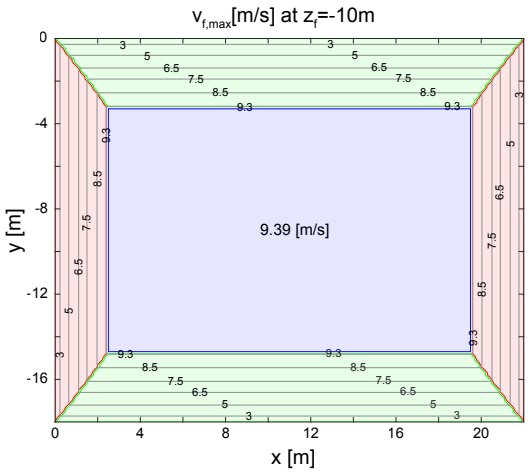

Figure 5.5: Contour plot of $v_{f,max}$ on the plane $z = -10m$, which corresponds to the cyan plane shown in Fig. 5.4

5.3.2 *Determination of the maximum height* z_{max}

In Section 5.2.1, the upper bounds in the pseudo-tensions were simplified by forcing the after-failure trajectory not to exceed a fixed height z_{max}. This approach made it possible to turn the limit in the maximum cable tension into a set of geometrical constraints on x_c and y_c described by (5.24). In this section, it is shown how to choose an appropriate z_{max}, such that constraints (5.24) are compatible with those deriving from the necessity of avoiding collisions with the physical boundaries of the workspace, described by (5.29). This procedure ensures the existence of Γ, a feasible region for the safe landing location $\mathbf{p}_c$.

First, the feasibility condition $y^*_{c,l} < y_{c,u}$ is rewritten using (5.24a) and (5.29b):

$$\frac{h\tau_{max}\cos\beta_{max}}{mg} > \frac{\bar{y}_f^2 + y_f^2}{-y_f} \tag{5.37}$$

Then, the second inequality in (5.30) is used to derive a sufficient condition on $\cos\beta_{max}$ to satisfy (5.37):

$$\cos\beta_{max} \geqslant \frac{mg}{\tau_{max}} \tag{5.38}$$

Note that the equal sign holds true because of (5.30). Starting from $x_{c,l} < x^*_{c,u}$, a similar approach can be applied to (5.24c) and (5.29a), this time using the first inequality in (5.30). This procedure leads to the same condition (5.38). Thus, the maximum z_{max} for which (5.38) holds true for any point $[x\ y\ z_{max}]^T$ within the pre-failure *SEW* is

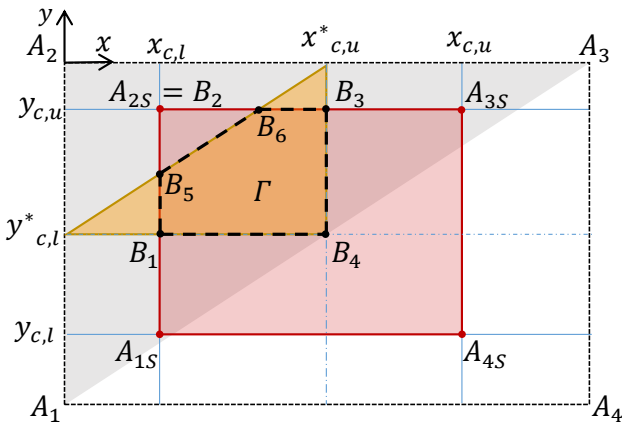

Figure 5.6: Feasible landing region Γ.

obtained by setting $\cos\beta_{max} = \frac{mg}{\tau_{max}}$, which leads to the following expression:

$$z_{max} = -\sqrt{\frac{g^2m^2\ (l^2+h^2)}{\tau_{max}^2 - g^2m^2}} \tag{5.39}$$

It is worth noting that with this convenient choice of $\cos\beta_{max}$, we obtain $y^*_{c,l} = -h/2$ and $x^*_{c,u} = l/2$. Therefore, constraints (5.24) take the simpler form:

$$x_c < \frac{l}{2}, \quad y_c > -\frac{h}{2}, \quad y_c < \frac{h}{l}x_c - \frac{h}{2} \tag{5.40}$$

It is now possible to understand the relative position of the vertex A_{2S} with respect to the straight lines $s : ly - hx + hl/2 = 0$ (delimiting the yellow region) and $r : ly - hx + hl = 0$ (delimiting the workspace) to better understand the shape of the feasible region Γ in different scenarios.

Vertex A_{2S} lies on the boundary of the red rectangle shown in Fig. 5.6, which is determined by conditions (5.29). Hence, its coordinates are $A_{2S} = [x_{c,l}\ y_{c,u}]^T$. The condition $A_{2S} \in SEW$ is equivalent to setting: $hl + ly_{c,u} - hx_{c,l} > 0$. By substituting the expressions of $y_{c,u}$ and $x_{c,l}$ from (5.29), the previous inequality is rewritten as:

$$x_f y_f \omega_n^2 (2hl - hx_f + ly_f) < hy_f \dot{x}_f^2 - lx_f \dot{y}_f^2 \tag{5.41}$$

Given that $x_f y_f < 0$ by definition and $2hl - hx_f + ly_f > 0$ (since $\mathbf{p}_f$ lies inside the pre-failure *SEW*), from (5.41) it is possible to find the values of ω_n for which A_{2S} lies inside the after-failure *SEW*:

$$\omega_n^2 > \frac{hy_f \dot{x}_f^2 - lx_f \dot{y}_f^2}{x_f y_f (2hl - hx_f + ly_f)} = \omega^2_{A_{2S}}. \tag{5.42}$$

It can be proven that, if $\omega_n^2 > \omega_{n,min}^2$, then $\omega_{A_{2S}}^2 < \omega_{n,min}^2$. Indeed, starting from equation (5.33a):

1. If $\omega_{n,min}^2 = \frac{\dot{x}_f^2}{x_f(l-x_f)}$, the condition for $\omega_{A_{2S}}^2 \leqslant \omega_{n,min}^2$ is $f = \dot{x}_f^2 y_f(h+y_f) - x_f \dot{y}_f^2 (x_f - l) \leqslant 0$, which holds because $\frac{\dot{x}_f^2}{x_f(l-x_f)} \geqslant \frac{-\dot{y}_f^2}{y_f(h+y_f)}$ if the value of $\omega_{n,min}^2$ is as stated above.

2. If $\omega_{n,min}^2 = \frac{-\dot{y}_f^2}{y_f(h+y_f)}$, the condition for $\omega_{A_{2S}}^2 \leqslant \omega_{n,min}^2$ is $f \geqslant 0$, which holds because $\frac{-\dot{y}_f^2}{y_f(h+y_f)} \geqslant \frac{\dot{x}_f^2}{x_f(l-x_f)}$ if the value of $\omega_{n,min}^2$ is as stated above.

3. If $\omega_{n,min}^2 = -\frac{2g(z_f+H)+\dot{z}_f^2}{z_f^2-H^2}$, then $-\frac{2g(z_f+H)+\dot{z}_f^2}{z_f^2-H^2} \geqslant \max\left\{\frac{\dot{x}_f^2}{x_f(l-x_f)}, \frac{-\dot{y}_f^2}{y_f(h+y_f)}\right\}$. Thus, it must be one of the following:

   a) if $\max\left\{\frac{\dot{x}_f^2}{x_f(l-x_f)}, \frac{-\dot{y}_f^2}{y_f(h+y_f)}\right\} = \frac{\dot{x}_f^2}{x_f(l-x_f)}$ and $f \leqslant 0$, it can be inferred from case 1 that $\omega_{A_{2S}}^2 \leqslant \frac{\dot{x}_f^2}{x_f(l-x_f)}$. Hence, $-\frac{\dot{z}_f^2+2g(z_f+H)}{z_f^2-H^2} \geqslant \frac{\dot{x}_f^2}{x_f(l-x_f)} \geqslant \omega_{A_{2S}}^2$. Conversely, if $f \geqslant 0$, from case 2 it can be inferred that $\omega_{A_{2S}}^2 \leqslant \frac{-\dot{y}_f^2}{y_f(h+y_f)} \leqslant \frac{\dot{x}_f^2}{x_f(l-x_f)} \leqslant \omega_{n,min}^2$.

   b) if $\max\left\{\frac{\dot{x}_f^2}{x_f(l-x_f)}, \frac{-\dot{y}_f^2}{y_f(h+y_f)}\right\} = \frac{-\dot{y}_f^2}{y_f(h+y_f)}$ and $f \geqslant 0$, it can be inferred from case 2 that $\omega_{A_{2S}}^2 \leqslant \frac{-\dot{y}_f^2}{y_f(h+y_f)}$. Hence, $-\frac{\dot{z}_f^2+2g(z_f+H)}{z_f^2-H^2} \geqslant \frac{-\dot{y}_f^2}{y_f(h+y_f)} \geqslant \omega_{A_{2S}}^2$. Conversely, if $f \leqslant 0$, from case 1 it can be inferred that $\omega_{A_{2S}}^2 \leqslant \frac{\dot{x}_f^2}{x_f(l-x_f)} \leqslant \frac{-\dot{y}_f^2}{y_f(h+y_f)} \leqslant \omega_{n,min}^2$.

It is possible to conclude that the condition $\omega_{A_{2S}}^2 < \omega_{n,min}^2$ is always satisfied for $\omega_n^2 > \omega_{n,min}^2$ and consequently A_{2S} lies inside the new *SEW*. A similar reasoning can be applied to prove that A_{4S} lies outside the after-failure *SEW* when $\omega_n^2 > \omega_{n,min}^2$.

Given that A_{2S} belongs to the after-failure SEW, condition $A_{2S} \in \Gamma$ is fulfilled when A_{2S} lies below the straight line $s: \; ly - hx - hl/2 = 0$. Using (5.29), such condition is written as:

$$(ly_f - hx_f) + \left(l\frac{\dot{y}_f^2}{y_f} - h\frac{\dot{x}_f^2}{x_f}\right) \leqslant -hl \tag{5.43}$$

Any failure point $\mathbf{p}_f$ that does not belong to the after-failure *SEW* satisfies the inequality $ly_f - hx_f \leqslant -hl$. Additionally, given (5.30), the expression inside the second parenthesis is strictly negative. Thus, if the failure occurs outside the new *SEW*, (5.43) holds true and it must be $A_{2S} \in \Gamma$.

5.4 SELECTING THE SAFE LANDING LOCATION

In this section, the boundaries of the feasible region Γ for the landing point $\mathbf{p}_c$ are derived, given the failure conditions on $\mathbf{p}_f$ and $\dot{\mathbf{p}}_f$. For

any z_c, conditions (5.28a) and (5.28b) identify the region to which $\mathbf{p}_c$ must belong to in order to avoid collisions with the physical boundaries of the workspace. This region is illustrated in Fig. 5.6 with a red rectangle whose vertexes are indicated as A_{iS}. Moreover, conditions (5.40) identify additional constraints on $\mathbf{p}_c$ to comply with the maximum cable tension τ_{max}. This second region corresponds to the yellow triangle shown in Fig. 5.6. The intersection between the two regions yields the feasible polygon Γ, whose vertexes are indicated as B_i. It can be proven that, if condition (5.31) is satisfied, vertexes A_{2S} and A_{4S} lie inside and outside the new *SEW*, respectively (see Appendix C). Moreover, from (5.40) it can be inferred that the vertex B_4 is the midpoint of the diagonal segment delimiting the new *SEW*. Hence, for any z_c, *a feasible polygon* Γ *always exists.*

Once the conditions for the existence of a feasible region Γ for the landing point $\mathbf{p}_c$ have been identified, the most convenient landing point within Γ, i.e., the one yielding the shorter landing time T, can be determined. Given the failure conditions $\mathbf{p}_f$ and $\dot{\mathbf{p}}_f$, the approximate minimum trajectory time T_{min} given by (5.27) only depends on the chosen safe landing location. Hence, finding $\mathbf{p}_c$ that minimizes T_{min} corresponds to solving a constrained non-linear optimization problem in the variables x_c, y_c and z_c:

$$\min_{\mathbf{p}_c} \ (T_{min}) \qquad \text{subject to: } \begin{cases} \omega_{n,min} < \omega_n < \omega_{n,max} \\ [x_c \ y_c]^T \in \Gamma(\omega_n), \end{cases} \tag{5.44}$$

where $\omega_{n,min}$ and $\omega_{n,max}$ are defined by (5.33) and T_{min} is selected as in (5.27). Since this numerical optimization must be performed in real-time immediately after a failure, solving a multi-variable, non-linear constrained optimization problem might not be feasible. We therefore propose to reduce (5.44) to a lower-dimension optimization problem, following one of these approximate strategies:

1. *Barycenter*: a first intuitive choice is to select the centroid of Γ. This represents a reasonable choice because the resulting trajectory will be far from the borders. The polygon Γ can have 4 or 5 vertexes, depending on the position of A_{2S} relative to the straight line $s: \ y = \frac{h}{l}x - \frac{h}{2}$ (see Appendix C). Those vertexes are known in closed-form for a given ω_n. Therefore, computing the barycenter of Γ is straightforward. With this approach, x_c and y_c are uniquely identified by ω_n, and (5.44) is thus approximated by a scalar optimization problem.

2. *Heuristic method*: an alternative choice consists in selecting x_c and y_c along the segment of the straight line A_2A_{2S} that belongs to Γ. If $A_{2S} \notin \Gamma$, a close approximation of the optimum pair (x_c, y_c) for given ω_n is found along this segment, leading to two nested scalar optimization problems, which are solved

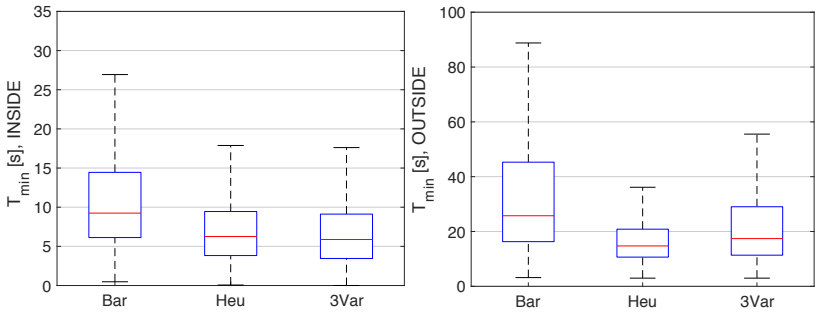

(a) Failure inside residual workspace (b) Failure outside residual workspace

Figure 5.7: Minimum Trajectory Time

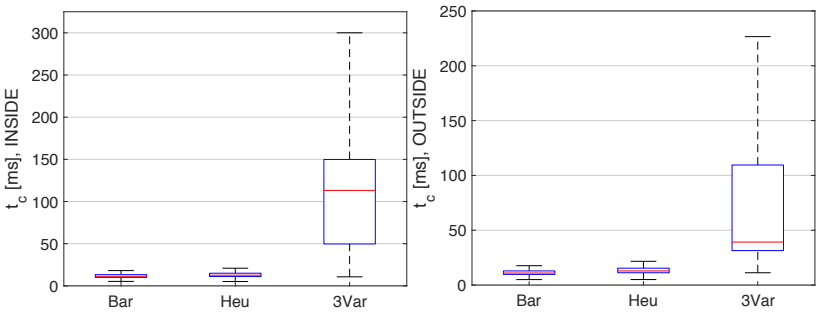

(a) Failure inside residual workspace (b) Failure outside residual workspace

Figure 5.8: Computational Time

in place of (5.44). If $A_{2S} \in \Gamma$, vertex A_{2S} yields the optimum for a given ω_n, hence (5.44) is reduced to a scalar optimization problem.

Because a sufficient condition for $A_{2S} \in \Gamma$ is that that the failure occurs outside the post-failure *SEW*, the heuristic solution yields the optimal solution with probability $> 50\%$.

Two benchmark tests were conducted to compare the performance of the strategies described above for failure points lying inside and outside the after-failure *SEW*, as shown in Fig. 5.7 and 5.8 using the following parameters: l=120m, h=80m, H=30m, m=30kg, τ_{max}=12kN.. Within each test, N=10,000 uniformly distributed random points inside (or outside) the after-failure *SEW* were tested. For each random point, Nv=100 random failure velocities were considered (with $\varphi \in [0,\ 2\pi]$, $\theta \in [0,\ 2\pi]$ and $v_f \in [0,\ v_{r,max}]$). In each point, three separate optimizations were conducted: (1) scalar optimization based on barycenter, yielding T_{Bar}; (2) heuristic method, yielding T_{Heu}; (3) multi-variable constrained optimization (5.44), yielding T_{3Var}. Tests were conducted on a 3.50 GHz Intel Xeon E5-1620 v3 using MATLAB (The Mathworks, MA, USA).

Figure 5.7 and 5.8show box plots of the optimized minimum trajectory time T_{min} and of the computational time t_c respectively. De-

		Bar	Heu	3Var
IN	Tmin [s]	11.55 (9.61)	7.34 (4.95)	7.03 (5.64)
	tc [ms]	13.86 (12.67)	17.38 (21.79)	136.42 (127.71)
OUT	Tmin [s]	43.87 (75.56)	17.04 (9.23)	26.76 (38.81)
	tc [ms]	13.71 (13.35)	17.23 (19.70)	65.09 (43.42)

Table 3: Mean and standard deviation of T_{min} and t_c for the three optimization strategies.

scriptive statistics are reported in Tab. 3. In both benchmark tests, the *Heuristic method* guaranteed a computational time that is comparable to the *Barycenter* strategy, while also leading to a better approximation of T_{min}. The optimal T_{min} yielded by the heuristic method was only slightly above T_{3Var} when the failure occurred inside the after-failure *SEW*. Interestingly, in the second benchmark test the average T_{Heu} was even smaller than T_{3Var}. This might be due to the fact that the multivariate method, unlike the other two methods, was not always able to find a good approximation of the optimum within the allowed number of iterations (which was the same for all three methods). Because choosing $\mathbf{p}_c$ at the boundary of Γ implies that the resulting elliptical trajectory might be tangent to the boundaries of the pre-failure *SEW* (as described by (5.28)), more conservative constraints should be imposed on the trajectory amplitudes, if the heuristic method is selected. In terms of computational time, both approximated methods clearly outperformed the multivariate approach in both benchmark tests (Tab. 3). Also, their performances were less affected by the location of the failure (i.e. either inside or outside the after-failure *SEW*). In summary, because these two methods can reduce both the average value and the variability in t_c, they represent a more desirable choice than the multivariate approach for real-time applications.

5.5 NUMERICAL VALIDATION

In this section, results from numerical simulations are presented to validate the proposed recovery strategy. The CDPR considered in the simulations is dimensionally comparable to a typical cable camera for football stadiums, whose layout is described by these parameters: $l = 120m$, $h = 80m$ and $H = 30m$. The mass of the camera and the maximum tension are set to $m = 30kg$ and $\tau_{max} = 12kN$, respectively. Based on these values, the maximum height resulting from (5.39) is: $z_{max} = -3.54m$.

A failure is assumed to takes place in the cable attached to vertex A_4, while the end effector is moving along a linear path from $\mathbf{p}_s = [24\ -24\ -6]^T$ m to $\mathbf{p}_e = [96\ -64\ -15]^T$ m. The failure occurs at $t_f = 10.5$ s, when the position of the end effector is $\mathbf{p}_f = [84.26\ -57.48\ -13.53]^T$ m and the magnitude of the velocity vector is $v_f = 7.31$ m/s.

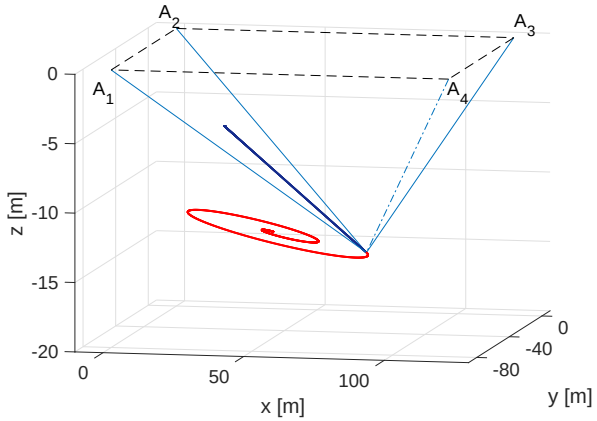

Figure 5.9: 3D view of the recovery trajectory using the heuristic strategy

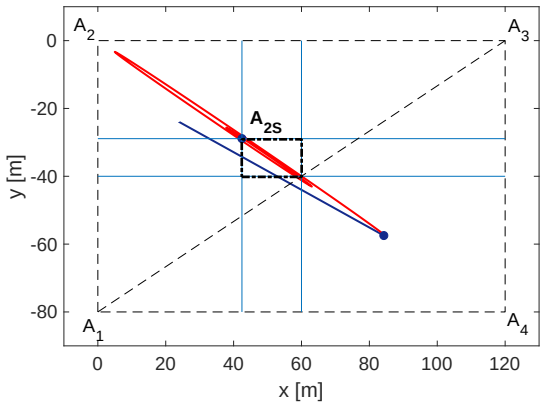

Figure 5.10: top view of the recovery trajectory using the heuristic strategy.

In this point, the maximum acceptable velocity is $v_{f,max} = 12.43$ m/s, thus, a feasible recovery trajectory of the type described in Section 3 exists.

In the first simulation, the safe landing location $\mathbf{p}_c$ was selected using the heuristic approach. This optimization yielded $\mathbf{p}_c = [42.52 \ -28.89 \ -13.33]$ m, which corresponds to a minimum trajectory time $T = 14.47$ s. Optimality of this result was confirmed by using multivariable constrained optimization, which was conducted with the embedded MATLAB function *fmincon*.

Figure 5.2 shows the initial trajectory (blue line) along with the recovery trajectory (red line) terminating at point $\mathbf{p}_c$. In Fig. 5.10, the bold dashed lines indicate the boundary of the the feasible region Γ. The light blue lines delimiting Γ represent the constraints on x and y given by (5.24a) and (5.24c), (5.28a), (5.28b).

A second simulation was conducted starting from the same failure state, this time using the barycenter strategy to determine the safe landing point $\mathbf{p}_c$. This method yielded $\mathbf{p}_c = [51.23 \ -34.44 \ -13.32]$ m and the minimum trajectory time $T = 22.92$ s. The resulting trajectory

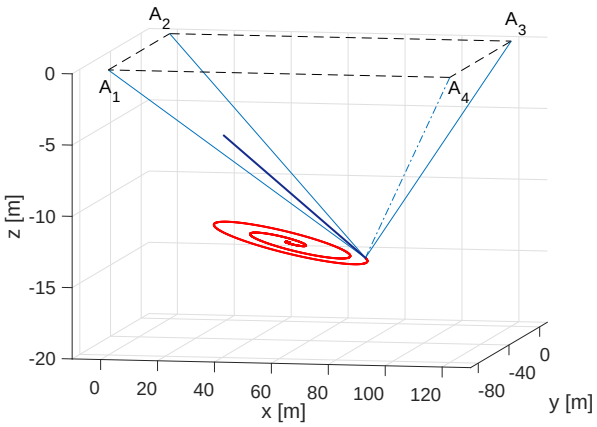

Figure 5.11: 3D view of the recovery trajectory using the barycenter strategy.

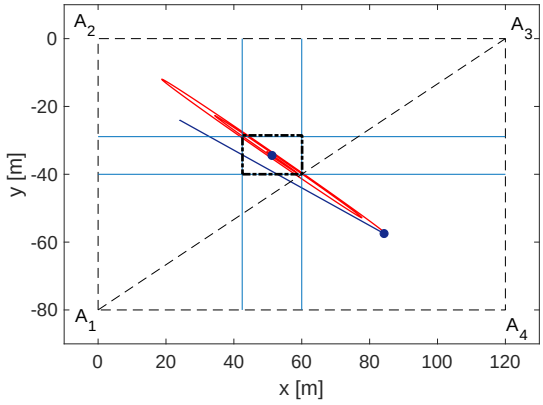

Figure 5.12: top view of the recovery trajectory using the barycenter strategy.

is illustrated in Fig. 5.11 and 5.12. As expected, the barycenter strategy resulted in a much longer landing time compared to the vertex strategy. However, the trajectory resulting from the barycenter strategy is more conservative, since it involves smaller amplitudes and is far away from the boundaries of the pre-failure *SEW*.

The tension configurations for the first and second simulations are shown in Fig. 5.13 and 5.14, respectively. In both cases, the tension in cable 4 becomes null after the failure instant, whereas the tensions in all the other cables remain positive and significantly below τ_{max} during the whole trajectory.

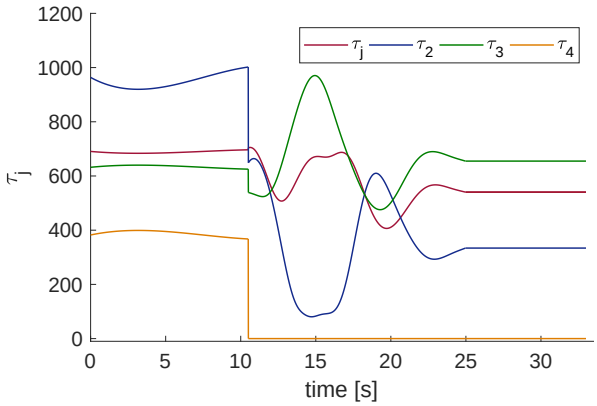

Figure 5.13: Cable tensions profiles for the vertex strategy

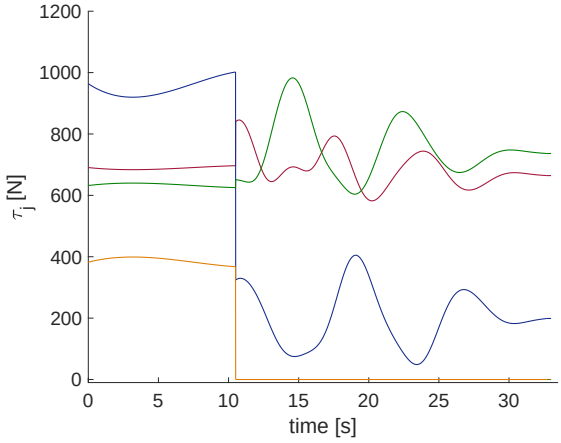

Figure 5.14: Cable tensions profiles for the barycenter strategy.

5.6 SUMMARY

In this chapter, a new method to manage the failure of cable-driven parallel robots was presented. Motivated by recent accidents involving cable-suspended camera systems, the recovery strategy was formulated for a point-mass robot suspended by four cables, assuming that the failure causes the breakage of one cable.

An after-failure oscillatory trajectory was proposed to steer the end-effector towards a safe landing location. Sufficient conditions for the existence of such trajectory were derived to guarantee positive and bounded cable tensions, as well as a collision-free path. It was shown that those conditions can be reduced to an upper limit on the norm of the end-effector velocity at the failure point and a maximum height that the camera is allowed to reach.

Additionally, two computationally efficient optimization strategies were presented to select the safe landing point among a feasible set,

with the goal of minimizing the trajectory time. Numerical simulations were carried out to validate the proposed strategies.

6

CASE STUDY: SUSPENDED 2 DOF CABLE ROBOT

In the previous chapters, a general dissertation on the possible after failure strategy approaches has been presented. In this Chapter, a peculiar robot configuration has been chosen to show the effectiveness of the proposed strategies. The chosen configuration is firstly presented and analyzed. Afterwards, an efficient adaptation of the general strategies to the case study is proposed and described.

Among all possible cable robots, a particularly challenging family is represented by suspended cable robots. Indeed, such robots must rely on gravity to keep positive cable tensions. In these manipulators, the cables can generate only forces in the positive z-direction while only the gravity can exert a pulling force in the negative z-direction. Moreover, while the force exerted by cables can be adjusted by properly controlling the actuators, the weight force has a fixed value that can not be changed. This implies a more difficult control on the end effector when compared to non-suspended configurations.

In this Chapter, among all possible suspended configurations, we study a manipulator having 3 cables and 2 degrees of freedom. Such configuration represents an useful and illustrative example since it allows applying both strategies given that:

- the after failure workspace is not-null, requirement of the first strategy
- after failure configuration is fully actuated ($m = n$), requirement of the second strategy

The robot workspace is a vertical plane in which the end effector can translate in two directions. A schematic representation of the prototype is depicted in Fig. 6.1.

Hence, after failure, the robot configuration will turn into a $n = m = 2$ and, thanks to the gravity, it will be still fully constrained. The third cable is not critical for this dissertation and hence, in our prototype, the third cable will be considered as an external force acting on the end effector that suddenly turns to zero to simulate a cable breakage.

In the following Sections, the prototype is analyzed and the actual kinematic and dynamic model is proposed.

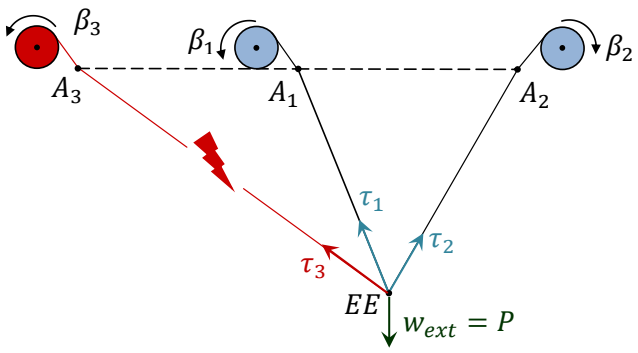

Figure 6.1: Schematic representation of the prototype

6.1 ROBOT MODEL AND CONTROL

Given that the number of degrees of freedom is the same as the number of cables, the direct kinematic position problem is simple and can be easily solved as intersection of 2 circumferences as described in Section 2.1.1. Each cable is wounded around a pulley and pass through a cable seal which represents the *attachment* point on the fixed structure.

The coordinates of the attachments points are respectively:

$$\mathbf{A}_1 = \begin{bmatrix} A_{1x} \\ A_{1y} \end{bmatrix} \qquad \mathbf{A}_2 = \begin{bmatrix} A_{2x} \\ A_{2y} \end{bmatrix} \qquad \mathbf{A}_3 = \begin{bmatrix} A_{3x} \\ A_{3y} \end{bmatrix}$$

Since the origin of the reference frame is set on the bottom left side of the workspace, in this environment all the x and y coordinates will have positive values (given that the end effector stays inside the initial workspace). The end effector is a point-mass and its coordinates will be defined as $\mathbf{x} = [x_p \; y_p]^T$.

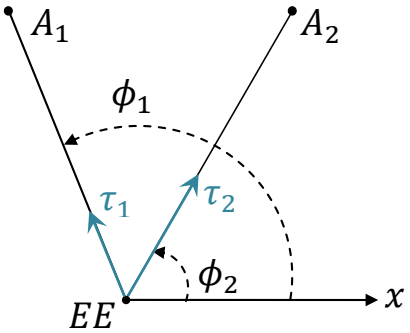

Figure 6.2: Schematic representation of ϕ_1 and ϕ_2

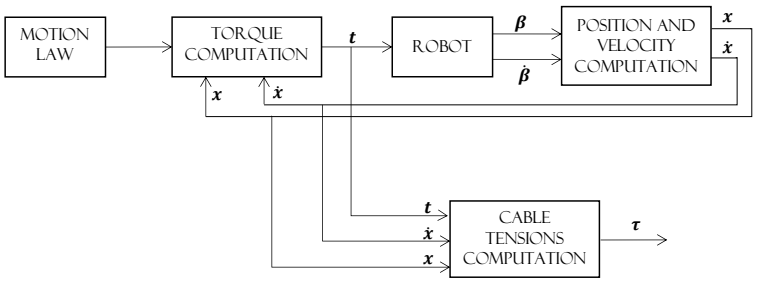

Figure 6.3: Schematic Control Scheme

The cable lengths will be referred as L_1 and L_2 respectively and will depend on the angular rotation of each pulley. The pulleys have radius r and their angular positions identify the vector $\boldsymbol{\beta} = [\beta_1 \ \beta_2]^T$.

The angles of the two cables can be counterclockwise referred to the *x-axes* with the symbols ϕ_1 and ϕ_2 as depicted in Fig. 6.2.

A schematic representation of the control scheme is given in Fig.6.3. Given a specific motion law, the first step consists in computing the torques that each motor must exert. In order to compute such torques (i.e., $\mathbf{t} = [t_1 \ t_2]^T$) it is first necessary to solve the inverse kinematic problem aimed at finding the length of each cables starting from the Cartesian coordinates of the end effector. The inverse kinematic problem can be easily solved by the following equations:

$$L_1 = \sqrt{(x_p - A_{1x})^2 + (y_p - A_{1y})^2} \tag{6.1}$$

$$L_2 = \sqrt{(x_p - A_{2x})^2 + (y_p - A_{2y})^2} \tag{6.2}$$

Similarly, it is possible to compute the angles between the cables and the *x-axis* as:

$$\phi_1 = atan2(A_{1y} - y_p, A_{1x} - x_p) \tag{6.3}$$

$$\phi_2 = atan2(A_{2y} - y_p, A_{2x} - x_p) \tag{6.4}$$

from which one can simply define the structure matrix $\mathbf{S}$ as

$$\mathbf{S} = \begin{bmatrix} \cos(\phi_1) & \cos(\phi_2) \\ \sin(\phi_1) & \sin(\phi_2) \end{bmatrix}$$

.

Given that $\mathbf{S}$ is a squared matrix, its inverse can be easily inferred as follows:

$$\mathbf{S}^{-1} = \frac{1}{\det(\mathbf{S})} \begin{bmatrix} \sin(\phi_2) & -\cos(\phi_2) \\ -\sin(\phi_1) & \cos(\phi_1) \end{bmatrix} \tag{6.5}$$

where $\det(\mathbf{S}) = \cos(\phi_1)\sin(\phi_2) - \cos(\phi_2)\sin(\phi_1)$.

It is now possible to compute the Jacobian matrix in order to solve the kinematic velocity problem ($\dot{\boldsymbol{\beta}} = \mathbf{J}\dot{\mathbf{x}}$). Given L_1 and L_2, it is possible to rewrite the angles β_i as:

$$\beta_1 = \frac{L_{10} - L_1}{r} + \beta_{10} \tag{6.6}$$

$$\beta_2 = \frac{L_{20} - L_2}{r} + \beta_{20} \tag{6.7}$$

where L_{i0} and β_{i0} represent the initial length and angular position of the *i*-th cable. By deriving the previous expressions, it is possible to obtain the angular velocity β_i:

$$\dot{\beta_1} = -\frac{\dot{L_1}}{r} \tag{6.8}$$

$$\dot{\beta_2} = -\frac{\dot{L_2}}{r} \tag{6.9}$$

Such equations describe the relationship between the angular velocity of the pulley and the difference in the length of the cable. If $\dot{\beta}_i > 0$, the length of the *i*-th cable is decreasing and hence the cable is wounding around the pulley (Fig. 6.4). Conversely, the pulley is releasing the cable if $\dot{\beta}_i < 0$ by increasing its length.

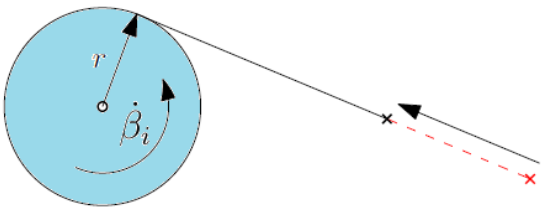

Figure 6.4: Wounding of the cable around the pulley

Starting form (6.1) and (6.2), it is possible to rewrite the inverse kinematic position problem as:

$$\begin{cases} L_1^2 = (x_p - A_{1x})^2 + (y_p - A_{1y})^2 \\ L_2^2 = (x_p - A_{2x})^2 + (y_p - A_{2y})^2 \end{cases}$$

$$\begin{cases} L_1^2 = x_p^2 + A_{1x}^2 - 2x_p A_{1x} + y_p^2 + A_{1y}^2 - 2y_p A_{1y} \\ L_2^2 = x_p^2 + A_{2x}^2 - 2x_p A_{2x} + y_p^2 + A_{2y}^2 - 2y_p A_{2y} \end{cases}$$

and the first order derivative can be obtained straightforwardly as:

$$\begin{cases} 2L_1\dot{L_1} = 2x_p\dot{x_p} - 2A_{1x}\dot{x_p} + 2y_p\dot{y_p} - 2A_{1y}\dot{y_p} \\ 2L_2\dot{L_2} = 2x_p\dot{x_p} - 2A_{2x}\dot{x_p} + 2y_p\dot{y_p} - 2A_{2y}\dot{y_p} \end{cases}$$

which can be rewritten in a more compact form as:

$$\begin{bmatrix} 2L_1 & 0 \\ 0 & 2L_2 \end{bmatrix} \begin{bmatrix} \dot{L_1} \\ \dot{L_2} \end{bmatrix} = \begin{bmatrix} 2(x_p - A_{1x}) & 2(y_p - A_{1y}) \\ 2(x_p - A_{2x}) & 2(y_p - A_{2y}) \end{bmatrix} \begin{bmatrix} \dot{x_p} \\ \dot{y_p} \end{bmatrix} \tag{6.10}$$

By substituting (6.8) and (6.9) in (6.10) we obtain :

$$\begin{bmatrix} -2L_1 r & 0 \\ 0 & -2L_2 r \end{bmatrix} \begin{bmatrix} \dot{\beta_1} \\ \dot{\beta_2} \end{bmatrix} = \begin{bmatrix} 2(x_p - A_{1x}) & 2(y_p - A_{1y}) \\ 2(x_p - A_{2x}) & 2(y_p - A_{2y}) \end{bmatrix} \begin{bmatrix} \dot{x_p} \\ \dot{y_p} \end{bmatrix} \tag{6.11}$$

from which is possible to compute the angular velocity vector $\dot{\boldsymbol{\beta}}$:

$$\begin{bmatrix} \dot{\beta_1} \\ \dot{\beta_2} \end{bmatrix} = \begin{bmatrix} \frac{A_{1x} - x_p}{rL_1} & \frac{A_{1y} - y_p}{rL_1} \\ \frac{A_{2x} - x_p}{rL_2} & \frac{A_{2y} - y_p}{rL_2} \end{bmatrix} \begin{bmatrix} \dot{x_p} \\ \dot{y_p} \end{bmatrix} \tag{6.12}$$

Such expression represents the Jacobian matrix $\mathbf{J}$:

$$\mathbf{J} = \begin{bmatrix} \frac{\partial \beta_1}{\partial x_p} & \frac{\partial \beta_1}{\partial y_p} \\ \frac{\partial \beta_2}{\partial x_p} & \frac{\partial \beta_2}{\partial y_p} \end{bmatrix} = \begin{bmatrix} \frac{A_{1x} - x_p}{rL_1} & \frac{A_{1y} - y_p}{rL_1} \\ \frac{A_{2x} - x_p}{rL_2} & \frac{A_{2y} - y_p}{rL_2} \end{bmatrix} \tag{6.13}$$

The angular acceleration vector $\ddot{\boldsymbol{\beta}}$, can be expressed by deriving equation $\dot{\boldsymbol{\beta}} = \mathbf{J}\dot{\mathbf{x}}$:

$$\ddot{\boldsymbol{\beta}} = \dot{\mathbf{J}}\dot{\mathbf{x}} + \mathbf{J}\ddot{\mathbf{x}} = \frac{d}{dt}\frac{\partial \boldsymbol{\beta}}{\partial \mathbf{x}}\dot{\mathbf{x}} + \frac{\partial \boldsymbol{\beta}}{\partial \mathbf{x}}\ddot{\mathbf{x}} \tag{6.14}$$

where:

$$\dot{\mathbf{J}} = \frac{d}{dt}\frac{\partial \boldsymbol{\beta}}{\partial \mathbf{x}} = \begin{bmatrix} \frac{d}{dt}\frac{\partial \beta_1}{\partial x_p} & \frac{d}{dt}\frac{\partial \beta_1}{\partial y_p} \\ \frac{d}{dt}\frac{\partial \beta_2}{\partial x_p} & \frac{d}{dt}\frac{\partial \beta_2}{\partial y_p} \end{bmatrix} = \begin{bmatrix} \dot{J}_{11} & \dot{J}_{12} \\ \dot{J}_{21} & \dot{J}_{22} \end{bmatrix} \tag{6.15}$$

Each term of $\dot{\mathbf{J}}$ can be expressed as follows:

$$\dot{J}_{11} = \frac{d}{dt}\frac{\partial \beta_1}{\partial x_p} = \frac{-\dot{x_p}\,(rL_1) - r\dot{L}_1\,(A_{1x} - x_p)}{r^2 L_1^2} = \frac{-\dot{x_p} L_1 - \dot{L}_1\,(A_{1x} - x_p)}{r L_1^2} \tag{6.16}$$

The term $\dot{L}_1$ can be found from equation (6.10) as:

$$\dot{L}_1 = \left(\frac{x_p - A_{1x}}{L_1}\right)\dot{x_p} + \left(\frac{y_p - A_{1y}}{L_1}\right)\dot{y_p} \tag{6.17}$$

By substituting (6.17) in (6.16), it is possible to rewrite $\dot{J}_{11}$ as:

$$\dot{J}_{11} = \frac{-\dot{x_p} L_1 - \left[\left(\frac{x_p - A_{1x}}{L_1}\right)\dot{x_p} + \left(\frac{y_p - A_{1y}}{L_1}\right)\dot{y_p}\right](A_{1x} - x_p)}{r L_1^2} \tag{6.18}$$

A similar reasoning can be applied to the other three components of $\dot{\mathbf{J}}$:

$$\dot{J}_{12} = \frac{-\dot{y_p} L_1 - \left[\left(\frac{x_p - A_{1x}}{L_1}\right)\dot{x_p} + \left(\frac{y_p - A_{1y}}{L_1}\right)\dot{y_p}\right](A_{1y} - y_p)}{r L_1^2} \tag{6.19}$$

$$\dot{J}_{21} = \frac{-\dot{x_p} L_2 - \left[\left(\frac{x_p - A_{2x}}{L_2}\right)\dot{x_p} + \left(\frac{y_p - A_{2y}}{L_2}\right)\dot{y_p}\right](A_{2x} - x_p)}{r L_2^2} \tag{6.20}$$

$$\dot{J}_{22} = \frac{-\dot{y_p} L_2 - \left[\left(\frac{x_p - A_{2x}}{L_2}\right)\dot{x_p} + \left(\frac{y_p - A_{2y}}{L_2}\right)\dot{y_p}\right](A_{2y} - y_p)}{r L_2^2} \tag{6.21}$$

It is now possible to derive the dynamic equation following three steps:

1. Find the dynamic equilibrium equation of the End Effector
2. Find the dynamic equilibrium equation of the pulley
3. Compute the equations found in 1 and 2 and find the overall dynamic equilibrium equation

Given that the end effector is considered as a point-mass, its dynamic equilibrium can be expressed as:

$$\mathbf{M}\ddot{\mathbf{x}} = \mathbf{w}_c + \mathbf{w}_{ext} \tag{6.22}$$

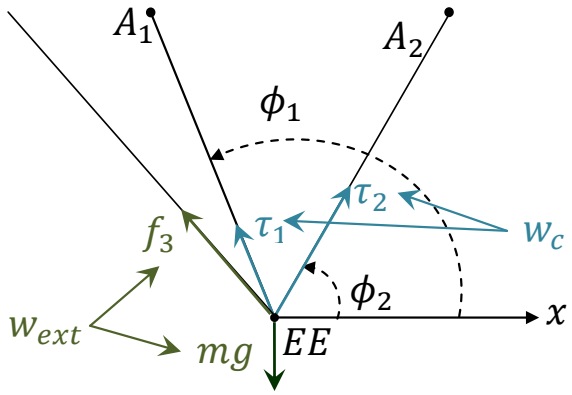

Figure 6.5: Dynamic equilibrium of the end effector

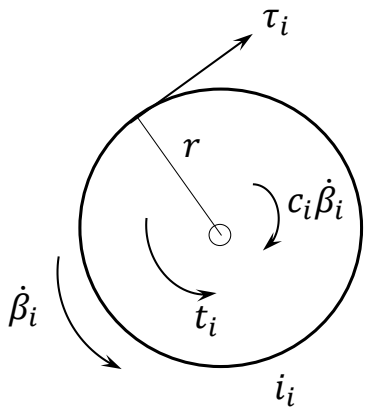

Figure 6.6: Dynamic equilibrium of the pulley

where $\mathbf{M}$ is the diagonal mass matrix expressed as:

$$\mathbf{M} = \begin{bmatrix} m & 0 \\ 0 & m \end{bmatrix}$$

Th vector $\mathbf{w}_c = \mathbf{S}\boldsymbol{\tau}$ represents the wrench exerted by cables while $\mathbf{w}_{ext}$ the overall contribution of the external forces. In particular, $\mathbf{w}_{ext}$ is the sum of the weight force and the external force $\mathbf{f}_3$ which represents the effect of the third cable before failure (as previously introduced, in our analysis we focus on the after failure approach, so the third cable is here considered as a constant force applied to the end effector before failure):

$$\mathbf{w}_{ext} = \mathbf{f}_{ext} = \begin{bmatrix} 0 \\ -mg \end{bmatrix} + \mathbf{f}_3 \tag{6.23}$$

The dynamic equilibrium of the end effector can be finally expressed

as

$$\mathbf{M}\ddot{\mathbf{x}} = \mathbf{S}\boldsymbol{\tau} + \mathbf{w}_{ext} \tag{6.24}$$

On the other hand, the dynamic equilibrium of the pulley can be expressed as:

$$\mathbf{t} = \mathbf{I}_m\ddot{\boldsymbol{\beta}} + \mathbf{C}_m\dot{\boldsymbol{\beta}} + \boldsymbol{\tau}r \tag{6.25}$$

where $\mathbf{I}_m$ is the inertia matrix of the actuators:

$$\mathbf{I}_m = \begin{bmatrix} i_1 & 0 \\ 0 & i_2 \end{bmatrix}$$

and $\mathbf{C}_m$ is the matrix of viscous damping coefficients:

$$\mathbf{C}_m = \begin{bmatrix} c_1 & 0 \\ 0 & c_2 \end{bmatrix}$$

It is now possible to put together the relations describing the dynamic equilibrium of the end effector and the one of the pulley to obtain a general formulation:

$$\mathbf{t} = \mathbf{I}_m\left(\dot{\mathbf{J}}\dot{\mathbf{x}} + \mathbf{J}\ddot{\mathbf{x}}\right) + \mathbf{C}_m\mathbf{J}\dot{\mathbf{x}} + \boldsymbol{\tau}r \tag{6.26}$$

Starting form (6.26), it is possible to compute $\boldsymbol{\tau}$ as:

$$\boldsymbol{\tau} = \frac{1}{r}\left(\mathbf{t} - \mathbf{I}_m\left(\dot{\mathbf{J}}\dot{\mathbf{x}} + \mathbf{J}\ddot{\mathbf{x}}\right) - \mathbf{C}_m\mathbf{J}\dot{\mathbf{x}}\right) \tag{6.27}$$

By substituting (6.27) into (6.24), the following equation can be obtained:

$$r\mathbf{M}\ddot{\mathbf{x}} = \mathbf{S}\mathbf{t} - \mathbf{S}\mathbf{I}_m\dot{\mathbf{J}}\dot{\mathbf{x}} - \mathbf{S}\mathbf{I}_m\mathbf{J}\ddot{\mathbf{x}} - \mathbf{S}\mathbf{C}_m\mathbf{J}\dot{\mathbf{x}} + r\mathbf{w}_{ext} \tag{6.28}$$

which can be rewritten as:

$$r\mathbf{M}\ddot{\mathbf{x}} + \mathbf{S}\mathbf{I}_m\mathbf{J}\ddot{\mathbf{x}} + \mathbf{S}\left(\mathbf{I}_m\dot{\mathbf{J}}\dot{\mathbf{x}} + \mathbf{C}_m\mathbf{J}\dot{\mathbf{x}}\right) = \mathbf{S}\mathbf{t} + r\mathbf{w}_{ext} \tag{6.29}$$

Such expression can be rewritten in a more compact form as:

$$\mathbf{M}_{eq}(x)\ddot{\mathbf{x}} + \mathbf{N}(x, \dot{x}) = \mathbf{S}\mathbf{t} + r\mathbf{w}_{ext} \tag{6.30}$$

where the equivalent mass matrix $\mathbf{M}_{eq}(\mathbf{x})$ and the matrix containing the non-linear terms $\mathbf{N}(\mathbf{x})$ are respectively:

$$\begin{aligned}\mathbf{M}_{eq}(x) &= r\mathbf{M} + \mathbf{S}\mathbf{I}_m\mathbf{J} = \begin{bmatrix} rm & 0 \\ 0 & rm \end{bmatrix} + \\ &+ \begin{bmatrix} \cos(\phi_1) & \cos(\phi_2) \\ \sin(\phi_1) & \sin(\phi_2) \end{bmatrix} \begin{bmatrix} i_1 & 0 \\ 0 & i_2 \end{bmatrix} \begin{bmatrix} \frac{A_{1x}-x_p}{rL_1} & \frac{A_{1y}-y_p}{rL_1} \\ \frac{A_{2x}-x_p}{rL_2} & \frac{A_{2y}-y_p}{rL_2} \end{bmatrix}\end{aligned} \tag{6.31}$$

$$\begin{aligned}\mathbf{N}(x,\dot{x}) &= \mathbf{S}\left(\mathbf{I}_m\dot{\mathbf{J}}\dot{\mathbf{x}} + \mathbf{C}_m\mathbf{J}\dot{\mathbf{x}}\right) = \begin{bmatrix} \cos(\phi_1) & \cos(\phi_2) \\ \sin(\phi_1) & \sin(\phi_2) \end{bmatrix} \cdot \\ &\cdot \left(\begin{bmatrix} i_1 & 0 \\ 0 & i_2 \end{bmatrix} \begin{bmatrix} \dot{J}_{11} & \dot{J}_{12} \\ \dot{J}_{21} & \dot{J}_{22} \end{bmatrix} \dot{\mathbf{x}} + \begin{bmatrix} c_1 & 0 \\ 0 & c_2 \end{bmatrix} \begin{bmatrix} \frac{A_{1x}-x_p}{rL_1} & \frac{A_{1y}-y_p}{rL_1} \\ \frac{A_{2x}-x_p}{rL_2} & \frac{A_{2y}-y_p}{rL_2} \end{bmatrix} \dot{\mathbf{x}} \right)\end{aligned} \tag{6.32}$$

From (6.30), it is possible to obtain the inverse dynamic equation as:

$$\mathbf{t} = \mathbf{S}^{-1}\left(\mathbf{M}_{eq}(x)\ddot{\mathbf{x}} + \mathbf{N}(x,\dot{x}) - r\mathbf{w}_{ext} - r\mathbf{f}_3\right) \tag{6.33}$$

It is worth noticing that, once the third cable breaks, the component $\mathbf{f}_3$ will be set equal to zero. The value of $\mathbf{f}_3$ before failure able to guarantee the static equilibrium can be found as follows:

$$\phi_3 = atan2(A_{3y} - y_p, A_{3x} - x_p) \tag{6.34}$$

$$\mathbf{f}_3 = \begin{bmatrix} \tau_3\cos(\phi_3) \\ \tau_3\sin(\phi_3) \end{bmatrix} \tag{6.35}$$

where τ_3 represent the tension of the third cable which in this example is considered constant before failure, while ϕ_3 has the same meaning previously given for ϕ_1 and ϕ_2.

Starting from equation (6.33), is it possible to estimate the acceleration of the end effector by exploiting the direct dynamic equation:

$$\ddot{\mathbf{x}} = \mathbf{M}_{eq}^{-1}(x)\left(-\mathbf{N}(x,\dot{x}) + \mathbf{S}\mathbf{t} + r\mathbf{w}_{ext} + r\mathbf{f}_3\right) \tag{6.36}$$

Once that the torque signal is given to the actuators, the end effector starts to move. A good estimation of the position and velocity of the end effector can be obtain by exploiting the angular velocity and position of the pulleys to solve the direct kinematic problem. For what concerns the velocity, the following relation holds:

$$\dot{\mathbf{x}} = \mathbf{J}^{-1}\dot{\boldsymbol{\beta}} \tag{6.37}$$

where the inverse of the Jacobian Matrix can be computed straightforwardly since $\mathbf{J}$ is a squared matrix.

The position of the end effector can be computed as:

$$x_p = \frac{A_{1x}^2 - A_{2x}^2 - L_1^2 + L_2^2}{2\left(A_{1x} - A_{2x}\right)} \tag{6.38}$$

$$y_p = \frac{1}{2}\left(2A_{1y} - 2\sqrt{K}\right) \tag{6.39}$$

$$\tag{6.40}$$

where

$$\begin{aligned} K = L_1^2 - A_{1x}^2 + \frac{A_{1x}\left(A_{1x}^2 - A_{2x}^2 - L_1^2 + L_2^2\right)}{A_{1x} - A_{2x}} - \\ - \frac{\left(A_{1x}^2 - A_{2x}^2 - L_1^2 + L_2^2\right)^2}{4\left(A_{1x} - A_{2x}\right)^2} \end{aligned} \tag{6.41}$$

Such values of position and velocity are used as feedback for the torque computation.

Finally, the cable tensions can be estimated starting from (6.24) as:

$$\boldsymbol{\tau} = \mathbf{S}^{-1}\left(\mathbf{M}\ddot{\mathbf{x}} - \mathbf{w}_{ext}\right) \tag{6.42}$$

Such value can be used to check the cable tension values in order to prove the effectiveness of the strategy of keeping bounded and positive cable tensions.

6.2 LINEAR STRATEGY APPROACH FOR THE CASE STUDY

Considering that the configuration of this prototype is particularly simple, a further analysis has been carried out to optimize the efficiency of the proposed algorithm for the considered case study.

During the connecting path, the algorithm generates a tension configuration aimed at minimizing the undesired velocity component v_o. The two main characteristics of the force exerted by cables would be:

1. Having a positive component along the *d-axis* in order to "push" the end effector towards the safe point: $f_d > 0$.
2. Having f_o in the opposite direction of v_o to exert a braking effect on the undesired velocity component.

The solution of this problem leads to a configuration in which the tensions are all at their maximum or minimum values. Having a configuration with only 2 cables, it is possible to analyze in which scenario each cable is supposed to get its maximum or minimum value depending on the angular position taken by the cable in the rotated reference frame *d-o*. Indeed, the new and ever changing reference frame identifies four quadrants: the cables lying in the first and fourth quadrants (depicted in green in Fig. 6.7) will exert a force directed towards the safe point, i.e. their projection on the *d-axis* will be positive ($f_d > 0$). Conversely, the cables lying in the second and third quadrant will have $f_d < 0$. Since they do not satisfy condition 1, their tension will be set at their minimum possible value. Regarding the condition number 2, only two quadrants will guarantee a component f_o that opposes the velocity v_o. The cables lying in those two quadrants are depicted in blue in Fig. 6.8. The cables lying outside these two quadrants do not guarantee condition 2 and hence their value will be kept to a minimum.

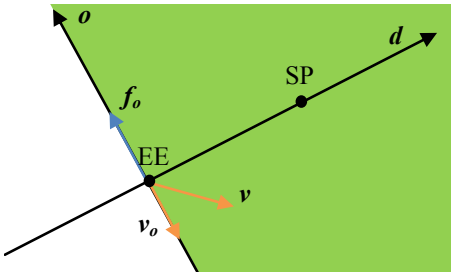

Figure 6.7: Example for quadrants with $f_d > 0$

By considering the previous analysis, only one quadrant will satisfy condition 1 and 2, and only one quadrant will not satisfy neither of the two conditions. The remaining two quadrants will satisfy only one condition at a time. The quadrant that satisfies both conditions is depicted in pink in Fig.6.9 and the cable lying in this quadrant will

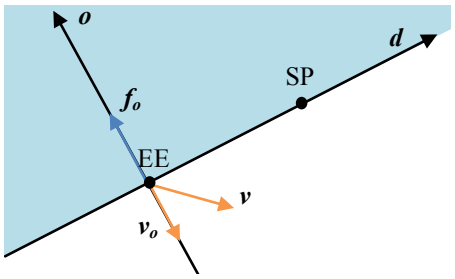

Figure 6.8: Example of quadrants having f_o that opposes v_o

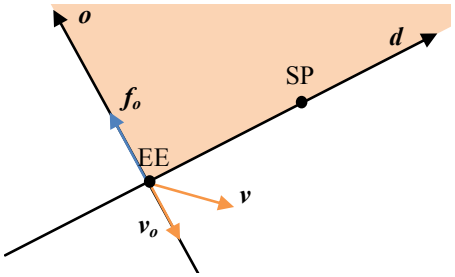

Figure 6.9: Example of a quadrant that satisfies both conditions

be set to a maximum value while all the other cables will be set to their minimum value.

However, it is possible that more than one cable lies in the chosen quadrant. In this case, the algorithm selects the one with maximum projection on the *o-axes*, i.e. the one having the maximum braking effect on the desired velocity component. An example is given in Fig.6.10 for a suspended cable robot with three cables: in this case both cables 2 and 3 lies in the desired quadrant. However, the projection of $\mathbf{f}_2$ on the *o-axis* is bigger than the one of $\mathbf{f}_3$. Hence, the algorithm will set cable 2 at its maximum tension value while all the other cables will be set to their minimum values.

Conversely, it can happen that none of the cables lie in the desired quadrant. In this case, the algorithm selects the one having a braking effect on v_o, even if $f_d < 0$. Indeed, by selecting this cable it is possible to minimize v_o by having the minimum impact on f_d.

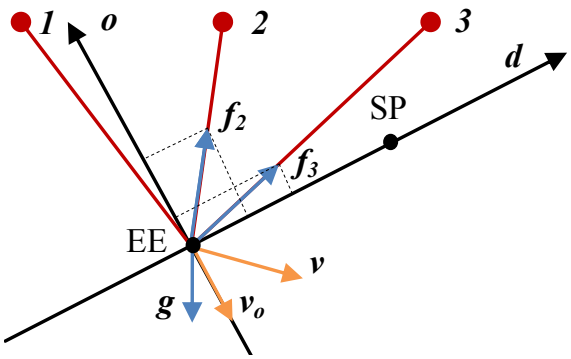

Figure 6.10: Cable selection for a suspended CDPR with 3 cables

It is worth noticing that the weight force is considered as a cable with constant tension and orientation. Hence, when the algorithm selects the weight vector, its braking effect is fixed and can not be controlled. On the other hand, when an actual cable is selected, its braking effect can be carefully changed by imposing a tension lower than its actual maximum possible value. Indeed, it could be worth reducing the braking effect by exerting a force f_o proportional to the velocity of the end effector at the failure instant. This could be helpful in those cases in which the velocity of the end effector is small and hence the algorithm would apply an exaggerated force on the end effector to brake a small velocity component while generating an undesired high acceleration. The desired braking force can be computed as:

$$f_{o,des} = f_{o,max} \frac{|\mathbf{v}_f|}{v_{max}} \tag{6.43}$$

where $f_{0,max}$ is braking force exerted if the cable tension is set equal to τ_{max}, and v_{max} is the maximum velocity that the end effector can reach inside the workspace (usually it is a parameter given form the retailer of the robot). The main advantage of this method is that it ensures that the exerted force has a braking effect on the undesired velocity component v_o, which would not be ensured if the proportion is done directly on the tension τ of the selected cable. Given the desired braking force $f_{o,des}$, it is possible to computed the tension of the selected cable (imposing all the other cable tensions at their minimum value).

Once that all the cable tensions are know, it is possible to compute the acceleration that will represent the acceleration reference in our control scheme:

$$\ddot{\mathbf{x}} = \mathbf{M}^{-1}\mathbf{W}\begin{bmatrix}\boldsymbol{\tau}\\ 1\end{bmatrix} \tag{6.44}$$

For what concerns the straight line path, considering that the configuration is simple, for this example we decided to use the strategy based on the on-line *WEC* index computation. As explained in Section 4.3.2, it is possible to exploit the geometry-based algorithm to compute the actual maximum braking effect on the end effector once the direction of motion has changed. Indeed, at the end of the connecting path, the component v_o is negligible and the velocity vector should be aligned with the *d-axes*. The block diagram in Fig. 6.11 summarizes the whole after failure approach. The Algorithm is divided into 2 phases:

1. *Phase 1*. Immediately after failure, it is possible that an actual braking force (i.e., a force F_v that opposes the velocity vector $\mathbf{v}$) exists. In this case, the braking force is applied until the end effector velocity is reduced to zero. If a braking force is not available, the connecting path is executed until the undesired velocity component v_o reaches a suitable small value.

2. *Phase 2*. When the velocity vector is directed towards the safe point (or when the end effect is instantly steady), the straight line motion can begin. If the end effector at this point already lies inside the residual workspace (i.e., it is possible to exert a force in any direction), an actual braking force F_v that opposes the motion can be exerted to stop the end effector. If the end effector is outside the the residual workspace, a minimum force towards the safe point is applied in order to lead the end effector inside the residual SEW. The cycle is iterated until the end effector reaches a velocity close to zero inside the workspace. At this point, the algorithm computes and applies the tension configuration aimed at maintaining static equilibrium.

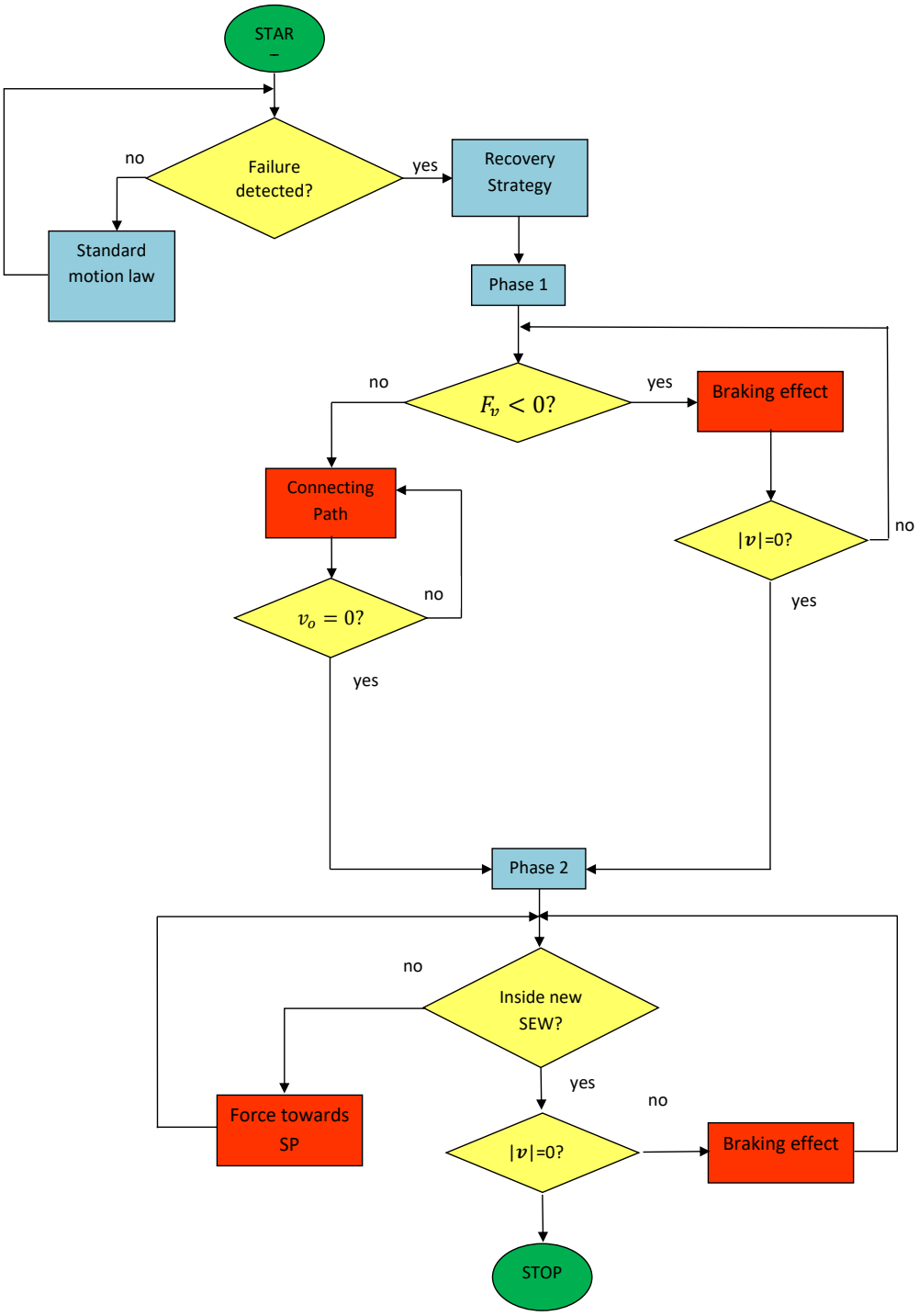

Figure 6.11: flow chart of the recovery strategy

6.3 PERIODIC TRAJECTORY APPROACH FOR THE CASE STUDY

For the case study in exam, all the reasoning done for the spatial cable robot in Section 5 can be applied almost straightforwardly with some minor changes. To simplify the equations, it is worth considering the coordinates of the attachments points as follows, considering the origin of the reference frame in the upper- left vertex of the fixed structure:

$$\mathbf{A}_1 = \begin{bmatrix} a \\ 0 \end{bmatrix} \qquad \mathbf{A}_2 = \begin{bmatrix} b \\ 0 \end{bmatrix} \qquad \mathbf{A}_3 = \begin{bmatrix} 0 \\ 0 \end{bmatrix}$$

The pseudo-tensions for the considered configuration are:

$$k_1 = \ddot{x}y + (\ddot{y} + g)(b - x) \tag{6.45}$$

$$k_2 = -\ddot{x}y - (\ddot{y} + g)(a - x) \tag{6.46}$$

and each cable tension can be referred to the corresponding pseudo-tension as $\tau_i = -\frac{\rho_i}{my(a-b)} k_i$.

The trajectory is the same elliptical trajectory as the one defined in Section 5 where only the coordinates x and y are considered. The y coordinate represent the vertical displacement in our case study.

The upper and lower bound of k_i have the same expressions as (5.17a) and (5.17b), with the following coefficients:

$$\begin{aligned}
a_1 &= g(b - x_c) - r_y(b - x_c)\omega_n^2 \\
b_1 &= -2\omega_n \frac{15}{8}(r_x y_c + r_y(b - x_c) + r_y r_x) \\
c_1 &= \frac{10\sqrt{3}}{3} l(r_x(H - y_c) + r_y(b - x_c) \\
a_1^* &= g(b - x_c) + r_y(b - x_c)\omega_n^2 \\
b_1^* &= -b_1 \\
c_1^* &= -c_1 \\
\\
a_2 &= g(x_c - a) - r_y\omega_n^2(x_c - a)\omega_n^2 \\
b_2 &= -2\omega_n \frac{15}{8}(r_x H - y_c + r_y(x_c - a) + r_y r_x) \\
c_2 &= \frac{10\sqrt{3}}{3}(r_x(H - y_c) + r_y(x_c - a) \\
a_2^* &= g(x_c - a) + r_y(x_c - a)\omega_n^2 \\
b_2^* &= -b_2 \\
c_2^* &= -c_2
\end{aligned} \tag{6.47}$$

It is straightforward to prove that a_1 and a_2 are positive given that in this case $\omega_n = \sqrt{-g/y_c}$ and that the trajectory must lie below a maximum height and above the ground. Hence that it is always

possible to find a trajectory time big enough to ensure positive cable tensions.

For what concern the constraint $\tau_i < \tau_{max}$ it must be:

$$a_j^* \leqslant K_{max} = \frac{\tau_{max}(b-a)\cos(\beta_{max})}{m} \tag{6.48}$$

Given that $1 < 1 - \frac{r_y}{y_c} < 2$, the constraints to ensure (6.48) are:

$$x_c \geqslant 2a - \frac{K_{max}}{2g} = x_{c,l}^* \tag{6.49}$$

$$x_c \leqslant a + \frac{K_{max}}{2g} = x_{c,u}^* \tag{6.50}$$

which can be resumed as

$$x_{c,l}^* \leqslant x_c \leqslant x_{c,u}^* \tag{6.51}$$

Moreover, for a feasible interval to exists, it must be $x_{c,l}^* \leqslant x_{c,u}^*$, which is always true if :

$$\cos\beta_{max} \geqslant \frac{mg}{\tau_{max}} \tag{6.52}$$

which recalls (5.38).

We also want to ensure a collision free path; hence, the following relations must hold:

$$(0 < x_c - r_x) \wedge (x_c + r_x < b) \tag{6.53a}$$

$$(y_c - r_y > -H) \wedge (y_c + r_y < y_{max}). \tag{6.53b}$$

Equation (6.53a) lead to the following constraints on x_c:

$$x_{c,l} < x_c < x_{c,u}, \text{ with } x_{c,l} = \frac{\bar{x}_f^2 + x_f^2}{2x_f},\ x_{c,u} = \frac{b^2 - \bar{x}_f^2 - x_f^2}{2(b - x_f)}, \tag{6.54}$$

By imposing the existence of a feasible interval for x_c, it is possible to find a range for $\bar{x}_f$. The same reasoning can be applied to y_c to find similar conditions on $\bar{y}_f$:

$$\begin{aligned} &\bar{x}_f^2 < x_f\,(b - x_f) \\ &\bar{y}_f^2 < (y_r + H)(y_{max} - y_r). \end{aligned} \tag{6.55}$$

These inequalities lead to a lower limit for ω_n :

$$\omega_n^2 \geqslant \max\left\{ \frac{\dot{x}_f^2}{x_f(b - x_f)},\ \frac{\dot{y}_f^2}{(y_r + H)(y_{max} - y_r)} \right\}. \tag{6.56}$$

Moreover, (6.53b) can be rewritten in terms of ω_n as:

$$-\frac{2g(y_f+H)+\dot{y}_f^2}{y_f^2-H^2} \leqslant \omega_n^2 \leqslant -\frac{2g(y_f-y_{max})+\dot{y}_f^2}{y_f^2-y_{max}^2}. \tag{6.57}$$

The constraints in 6.56 and 6.57 leads to an interval for ω_n:

$$\omega_{n,min} \leqslant \omega_n \leqslant \omega_{n,max} \tag{6.58}$$

$$\omega_{n,min}^2 = \max\left\{\frac{\dot{x}_f^2}{x_f(b-x_f)}, \frac{\dot{y}_f^2}{(y_r+H)(y_{max}-y_r)}, -\frac{2g(y_f+H)+\dot{y}_f^2}{y_f^2-H^2}\right\} \tag{6.59}$$

$$\omega_{n,max}^2 = -\frac{2g(y_f-y_{max})+\dot{y}_f^2}{y_f^2-y_{max}^2} \tag{6.60}$$

By imposing $\omega_{n,min} \leqslant \omega_{n,max}$, it is possible to derive constraints on the maximum feasible velocity at the failure instant. In order to simplify this task, we use polar coordinates, namely $\dot{x} = v_f\cos(\theta)$ and $\dot{y} = v_f\sin(\theta)$. We can separately study 3 cases:

- **Case A:** $\omega_{n,min}^2 = \frac{\dot{x}_f^2}{x_f(b-x_f)}$
  Condition (5.33c) is rewritten as: $\frac{v_f^2\cos^2\vartheta}{2(b-x_f)} + \frac{v_f^2\sin^2(\vartheta)}{y_f^2-y_{max}^2} + \frac{2g(y_f-y_{max})}{y_f^2-y_{max}^2}$.
  Let us indicate the sum of the coefficients of the velocity-dependent terms as: $s = \frac{\cos^2\vartheta}{2(b-x_f)} + \frac{\sin^2\vartheta}{y_f^2-y_{max}^2}$. The maximum values s can take are $s_{max,1} = \frac{1}{y_f^2-y_{max}^2}$, $s_{max,2} = \frac{1}{x_f(b-x_f)}$, which yield two possible values for $v_{f,max}$:
  Case A.1: $v_{f,max}^2 = -2g(y_f-y_{max})$, for $y_f^2+x_f^2-bx_f-y_{max}^2 < 0$
  Case A.2: $v_{f,max}^2 = \frac{-2gx_f(b-x_f)}{y_f+y_{max}}$, for $y_f^2+y_f^2-ly_f-y_{max}^2 \geqslant 0$
  The two cases are delimited by a half-circumferences with radius $r = \sqrt{y_{max}^2+b^2/4}$ and center in : $\left[\frac{b}{2}\ 0\right]^T$.

- **Case B:** $\omega_{n,min}^2 = -\frac{\dot{y}_f^2+2g(y_f+H)}{y_f^2-H^2}$
  Condition (5.33c) is rewritten as: $v_f^2\sin^2\vartheta \leqslant \frac{2g(y_f-y_{max})(H+y_f)}{y_{max}-H}$, which leads directly to to: $v_{f,max}^2 = \frac{2g(y_f-y_{max})(H+y_f)}{y_{max}-H}$.

- **Case C:** $\omega_{n,min}^2 = \frac{-\dot{y}_f^2}{(y_f-y_{max})(H+y_f)}$
  For $\dot{y}_f^2 < v_{f,max}^2$, the following must hold: $-\frac{\dot{y}_f^2}{(y_f-y_{max})(y_f+H)} < -\frac{\dot{y}^2+2g(y_f+H)}{y_f^2-H^2}$. Hence, $\omega_{n,min}^2 \neq \frac{-\dot{y}_f^2}{(y_f-y_{max})(H+z_f)}$ and we conclude that case C is not possible.

Hence, the possible values that v_{max} can possibly take are:

$$\begin{aligned} v_{fx,lim}^2 &= \frac{2gx_f(b-x_f)}{y_f+y_{max}} \\ v_{fy,lim}^2 &= -\frac{2g(y_f-y_{max})(H+y_f)}{H-y_{max}} \end{aligned} \tag{6.61}$$

The maximum velocity throughout the workspace can be find in Fig.6.12.

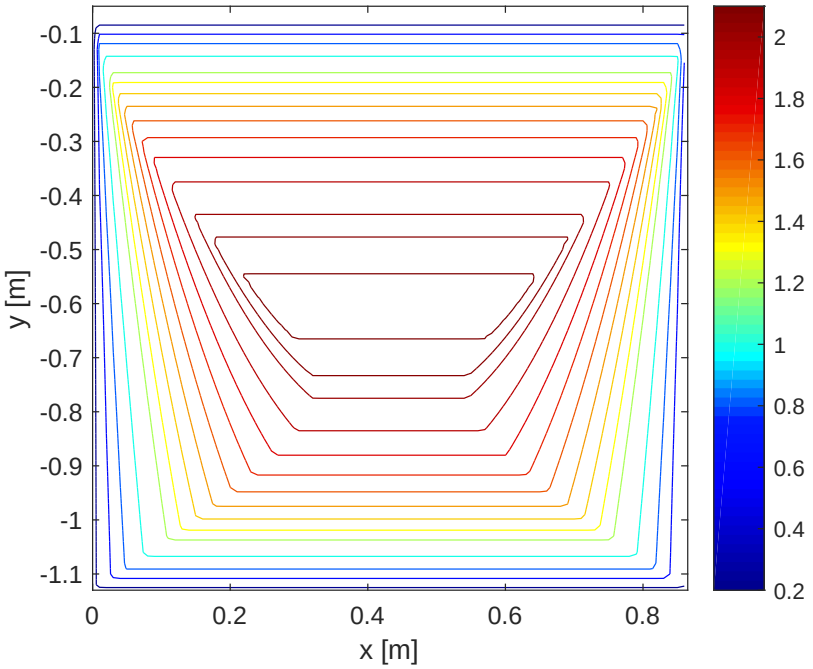

Figure 6.12: Maximum admissible velocity

In order to have have a feasible region for the safe landing location, it essential to check if the conditions on x_c in (6.54) are compatible with the one in (6.50). In order to have a feasible interval for x_c it must be:

1. $x^*_{c,u} \geqslant x_{c,l}$
2. $x^*_{c,l} \leqslant x_{c,u}$

It is easy it easy to prove that the first condition is always guaranteed (when considering the constraints given in (6.55) and (6.52)). The second condition requires a further constraint to be always satisfied, which leads to a new definition of β_{max}:

$$\cos(\beta_{max}) \geqslant 2\frac{mg}{\tau_{max}} \tag{6.62}$$

If this condition holds, it can be easily proved that a feasible interval for x_c always exists.

It is also important to stress that the safe landing location must belong to the residual SEW, i.e. $a \leqslant x_c \leqslant b$. Moreover, if β_{max} is chosen at its minimum value (see equation 6.62), it is straightforward to prove that $x^*_{c,u} = b$. Indeed, recalling 6.50, $x^*_{c,u} = a + \frac{\tau_{max}(b-a)\cos(\beta_{max})}{2mg}$. Given 6.62, the minimum value that $x^*_{c,u}$ can pos-

sibly take is exactly b. Following the same reasoning, it can be proved that the maximum value that $x^*_{c,l}$ can possibly take is exactly a.

Hence, the final feasible interval for x_c is: $[\max(a, x_{c,l}); \min(x_{c,u}, b)]$.

6.4 SUMMARY

This Chapter presented a case study based on a planar suspended cable robot with 3 cables and 2 translational degrees of freedom. The analysis focuses on the after failure control in case of 1 cable breaks. As a consequence, the resulting configuration is an under-actuated suspended cable robot. A general overview of the kinematic and dynamic analysis for the studied configuration is given in the beginning of the Chapter.

Afterwards, the two recovery approaches presented respectively in Chapter 4 and 5 are adapted and optimized for the studied configuration. The recovery approaches are tested on a real prototype and the related experimental results will be discussed in Chapter 7.

7

EXPERIMENTAL SETUP

This Chapter is dedicated to the description of the experimental set-up used to test the proposed strategies. Firstly, an overview of the hardware and software implementation is discussed. The prototype used for the tests is presented and described in details. Finally, experimental results regarding both the recovery approaches based on the linear trajectory and the one based on the periodic trajectory are presented and discussed

The prototype is controlled through a target PC connected to a host PC. The softwares used both in simulation and the real application are MATLAB® and Simulink® , and specifically Simulink Real-Time™for the actual implementation.

Fig. 7.1 shows the screen of the Target PC during the execution of the tests while picture of the studied cable robot is shown in Fig. 7.2

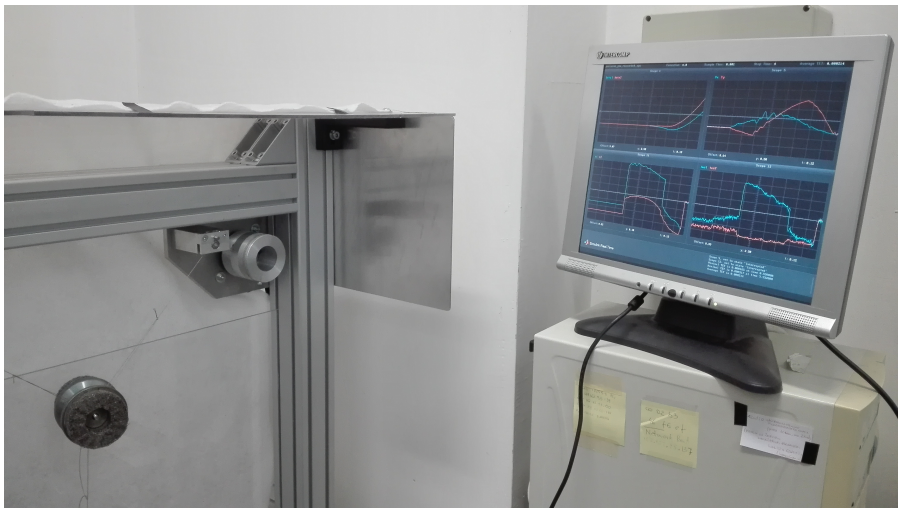

Figure 7.1: Target PC screen

The prototype used to test the proposed recovery strategies is shown in Fig.7.2. A detail of the end effector is shown in Fig. 7.3: it is realized by two equal metallic discs connected in the center with a screw. The end effector can freely move throughout the workspace defined by the fixed structure which dimensions are 1016 $mm \times 1164$ mm. The cables 2 cables (Dyneema®, Young module $E \approx 100$ GPa, yield tension $\sigma_s \approx 3$ GPa) are wounded around two actuated pulleys and pass through two connection points that represent the attachment points in the proposed model.

Figure 7.2: Prototype of the 2DoF cable robot

Figure 7.3: End Effector detail

The end effector can translate in the x-y plane and no rotations can be induced. Moreover, to avoid unwanted rotational motion, a PVC panel has been added behind the end effector.

For our purpose, only two cable must be active, while one represents only the additional force applied before failure. The active cables are attached to the point A_1 and A_2 on the upper part of the fixed structure and wounded around actuated pulleys, as shown in Fig.7.4. The third cable is attached to a small mass m_3 visible in Fig.7.5. The mass m_3 is hold up by an electromagnet that will simulate a cable breakage when the current is interrupt. Hence, the third cable has a fixed tension value equal to $\tau_3 = m_3 g$ which will exert a force on the end effector constant in module but variable in direction.

This setup allowed us to simulate the cable breakage an undefined number of times and in total safety, considering that the cable breakage command is given remotely, outside of the actual work area of the robot. Moreover, thanks to this design, it is immediate to recreate the initial condition before failure without dealing with the actual set-up of a new cable in substitution of the broken one.

The pulleys to which the active cables are wounded, are attached directly to two Siemens brushless motors (Nominal Torque $2,15\ \mathrm{Nm}$, maximum Torque $10\ \mathrm{Nm}$, nominal velocity $3000\ \mathrm{rpm}$) with two Simodrive 611U actuators.

Both digital and analog signals are managed by the software SimoComU, through which it is possible to decide the control mode of the actuators. For this case study, torque control represents the most suitable choice.

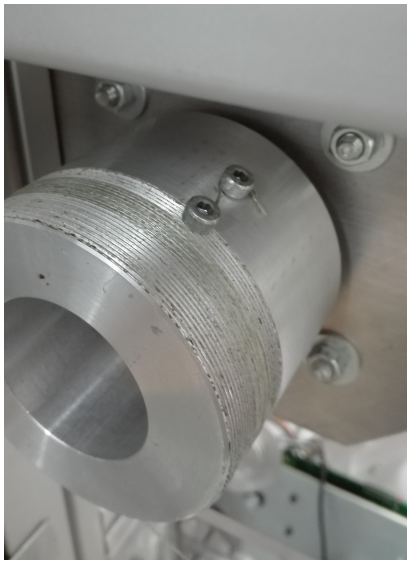

Figure 7.4: Detail of the actuated pulley

Figure 7.5: Third cable connected to the electromagnet

From the encoders inside the two actuators it is possible to receive a feedback in position (β) and velocity ($\dot{\beta}$). The initial angular position is set to zero:

$$\beta_0 = \begin{bmatrix} \beta_{10} \\ \beta_{20} \end{bmatrix} = \begin{bmatrix} 0 \\ 0 \end{bmatrix}$$

which will represent also the starting point to compute the initial length of the two active cables L_{10} and L_{20}.

The signal acquisition and generation is managed by the following I/O boards:

- PCIM-DDA06/16 (Measurement Computing) with 6, 16bit analog output channels for the brake and electromagnet control.
- PCI-QUAD04 (Measurement Computing) with 4 channels compatible with typical encoders, for the position feedback signals.
- PCI-6024E (National Instruments) with 16, 12bit analog input, for the velocity and torque control of the 2 actuators.

Finally, the main kinematic and inertial properties of characteristics of the cable robot are reported in table 4

Parameter	Value	Unit of measure
A_{1x}	0.43	m
A_{1y}	1.13	m
A_{2x}	0.865	m
A_{2y}	1.13	m
A_{3x}	0.035	m
A_{3y}	0.87	m
r_i (i=1,2)	0.03825	m
i_i (i=1,2)	$6.8414 \cdot 10^{-4}$	$kg \cdot m^2$
c_i (i=1,2)	$5 \cdot 10^{-3}$	$N \cdot m \cdot s$
m	1.036	kg
m_3	0.513	kg
τ_{max}	20	N
τ_{min}	1	N
SP	[0.65 ; 0.85]	m
v_{max}	1.5	m/s

Table 4: Characteristics of the prototype

where:

- A_{ix} is the x coordinate od the *i-th* attachment point

- A_{iy} is the y coordinate od the *i-th* attachment point
- r_i *i-th* the radius of the pulley
- i_i is the *i-th* concentrate inertia,including the motor and brake inertia
- c_i is the *i-th* dumping coefficient
- m is the mass of the end effector
- $m_3$is the mass attached to the electromagnet
- τ_{max} maximum cable tension set for this application
- τ_{min} minimum cable tension set for this application
- SP is the Safe Point
- v_{max} maximum velocity of the end effector

7.1 EXPERIMENTAL RESULTS: LINEAR STRATEGY

In this section the experimental results for the linear strategy are reported. The strategy have been tested in many different scenarios, and here are reported four representative examples that resume different possible failure conditions. In each of the four examples, the force before failure has been chosen in order to have a velocity vector having four completely different orientations. Indeed, the strategy adapts depending on the difference in orientation between the desired direction (unit vector $\boldsymbol{d}$ towards the safe Point) and the actual direction of motion ($\boldsymbol{v}$).

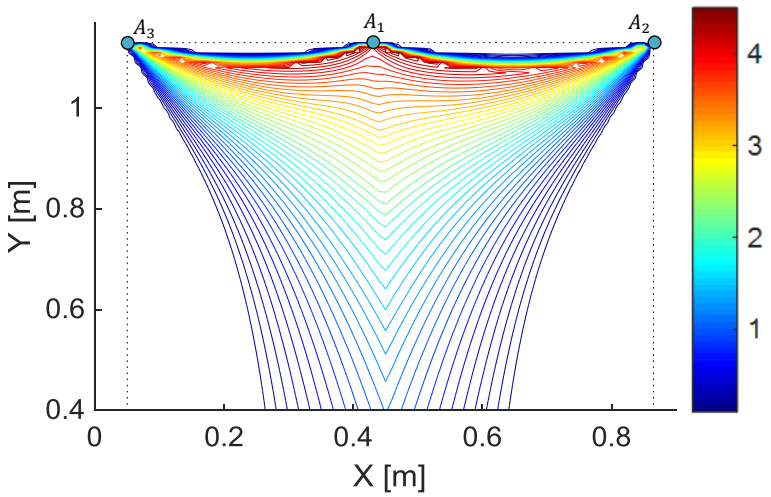

Figure 7.6: Minimum guaranteed force in any direction before failure

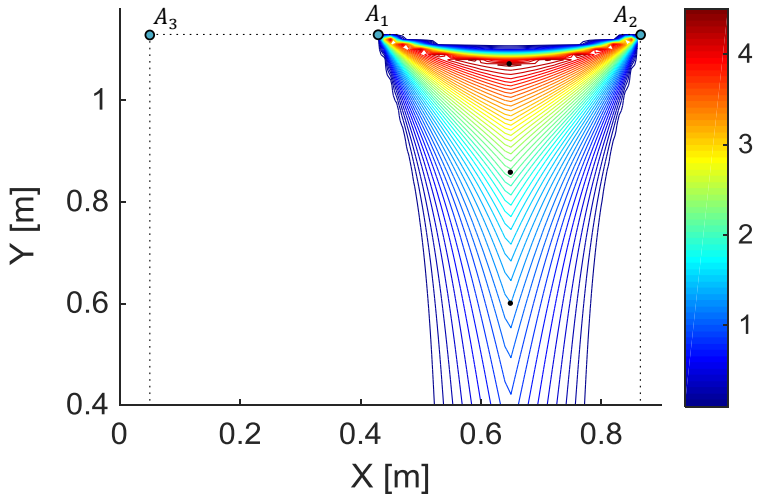

Figure 7.7: Minimum guaranteed force in any direction after failure

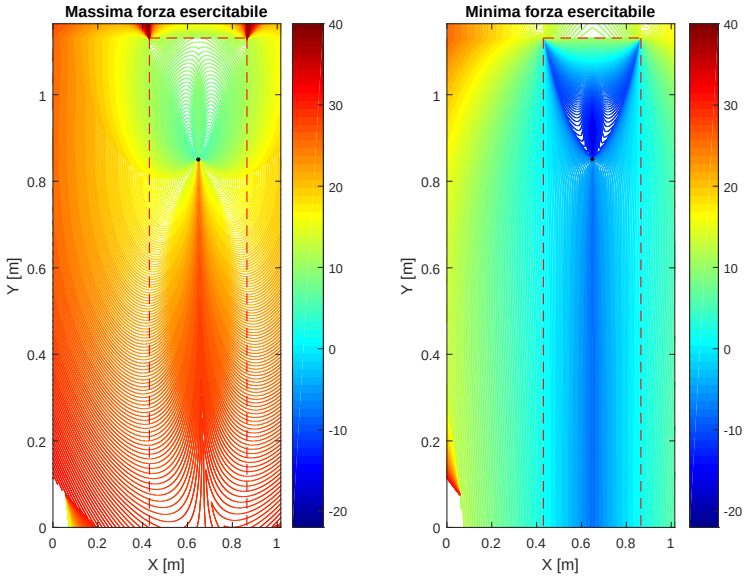

Figure 7.8: Maximum and Minimum exertable force in the direction of the safe point

In order to choose a proper Safe Point, an analysis has been carried out to appraise the minimum guaranteed force in any direction before and after failure. The results are shown in Fig.7.6 for the robot configuration before failure and in Fig.7.7 for the after failure configuration. It is clear that the best performance after failure is in the upper part of the workspace, very close to the attachments point: the point with maximum performance has coordinates $x = 0.65m$, $y = 1.7$. However, a second issue to consider is that the safe point represents a reference during the after failure trajectory and in general it does not represent the actual ending point. Hence, from a precautionary

point of view, it would be better to choose the safe point as fas as possible from the physical boundaries of the cable robot to reduce the risk of possible collisions. In order to ensure good performance after failure and reducing the risk of collisions, a good choice for the safe point is between the maximum performance point and the safest point. The chosen safe point has coordinates $x = 0.65m$, $y = 0.85$. Finally, an overall appraisal of the minimum and maximum force in the direction of the chosen safe point is given in Fig.7.8.

In the first two tests, the velocity is directed in the 4^{th} quadrant, with different orientations. The path of the end effector is shown in Fig.7.9 for test A and in Fig.7.10 for test B. It can be noticed as, especially in test B, the choice of a safe point far from the boundaries avoided a possible collision with the upper part of the fixed structure. In both cases, the red cross represents the position of the end effector at which the recovery strategy begins. At the same instant, the velocity vector is depicted with a red arrow. The red points represent the attachment point of the active cables, while the black point represents the Safe Point. With a small green dot is also depicted the end of the first phase of the strategy.

In both these tests, the cable chosen by the algorithm is the one attached to A_1, which is set to its maximum acceptable value (considering the proportion with the velocity of the end-effector at the failure instant as explained in Chapter 6.

In test C, the velocity vector lies on the 1^{st} quadrant; in this case the preferred cable is the weight force. Hence, both the active cables are set to their minimum value and the weight force is the one responsible of changing the direction of motion of the end effector. The path of the end effector is shown in Fig. 7.12. Finally, in test D, the velocity vector at the failure instant is directed in the 3^{rd} quadrant. In this case, the velocity is oriented in the opposite direction of the residual workspace; hence, it is possible to exert directly a braking force that opposes the velocity immediately after failure and it is not necessary to perform a connecting path in the first part of the strategy.

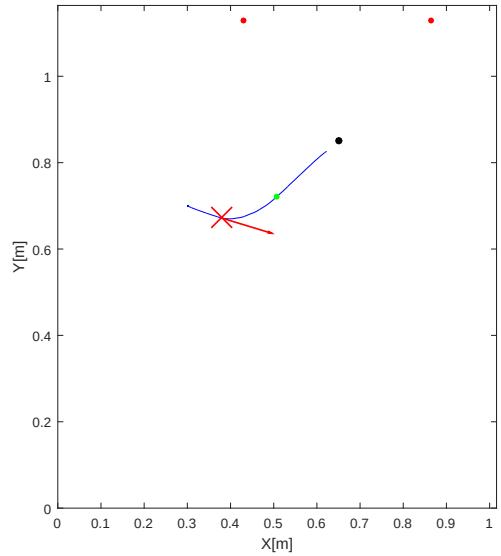

Figure 7.9: End effector path:test A

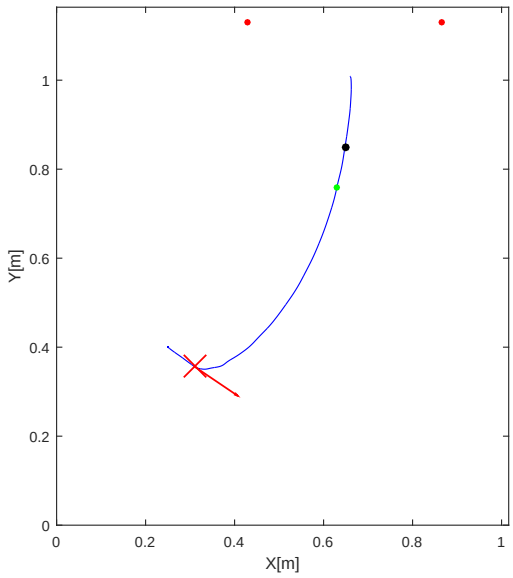

Figure 7.10: End Effector path: test B

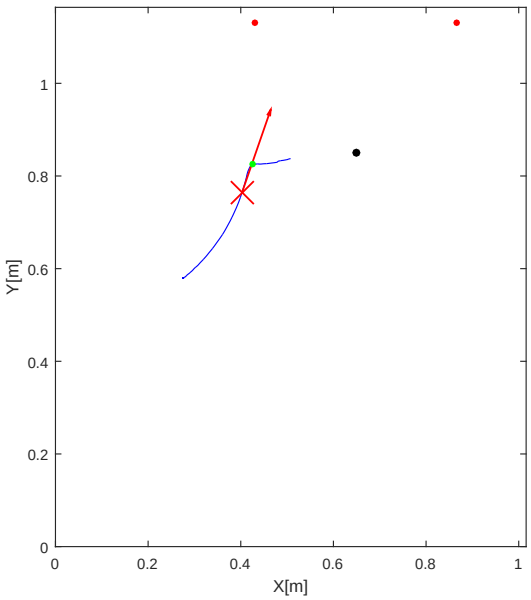

Figure 7.11: End effector path: test C

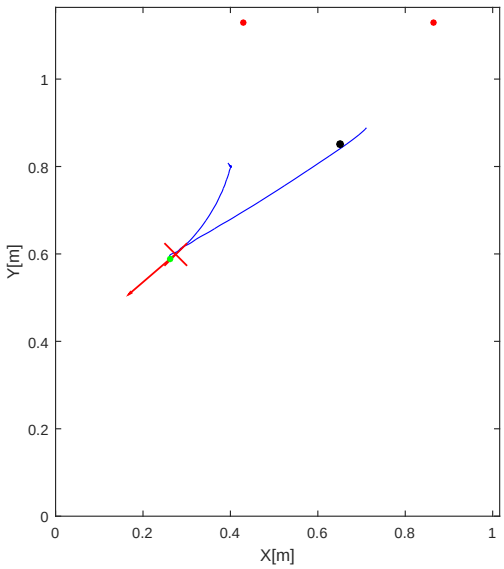

Figure 7.12: end effector path: test D

It can be shown that in all the four tests the tension limits are satisfied. Moreover, by a deeper analysis, it is possible to recognize the different phases. In the first two cases (Fig.7.13 and Fig.7.14), the first cable reaches the maximum value while the second cable is set to its minimum value. The third case (Fig.7.15) is the one in which the weight force is responsible of changing the direction of motion of the end effector, and hence both cables are set to their minimum values.

Finally, in the last case (Fig.7.16), both cables have variable tensions since the exerted force is the one aimed at braking the velocity immediately after failure.

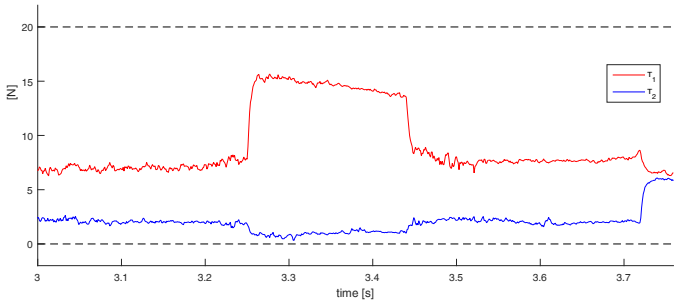

Figure 7.13: Cable tensions: test A

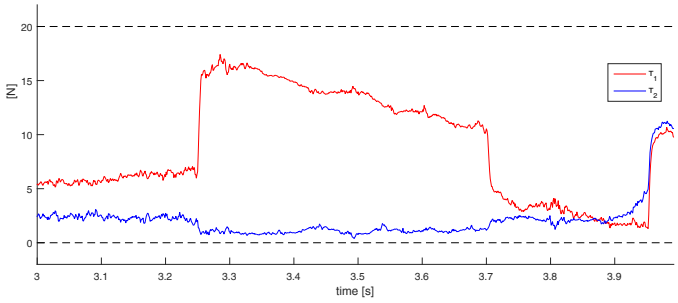

Figure 7.14: Cable tensions: test B

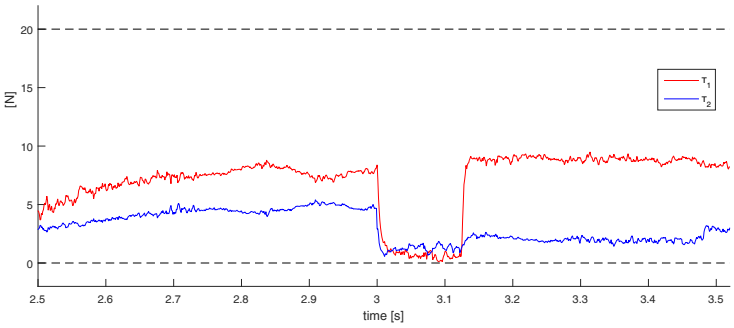

Figure 7.15: Cable tensions: test C

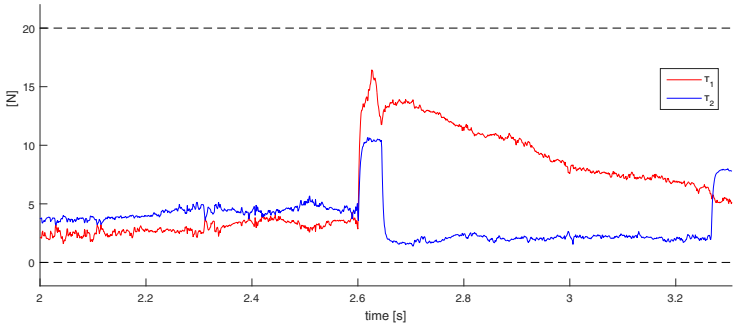

Figure 7.16: Cable tensions: test D

In order to avoid repetitions, in the following paragraphs test A is deeper analyzed (even if the same applies to test B, C and D).

The time line starts at $t = 3s$, time at which the end effector starts moving. The strategy algorithm starts with a delay of $0.2s$ in order to let the end effector reach a velocity different from zero.

In Fig.7.17 are shown the angular position of the motors: the dashed lines represent the values obtained during the simulation while the continuous ones represent the data obtained by the position feedback. The angular velocity are give in Fig.7.18.

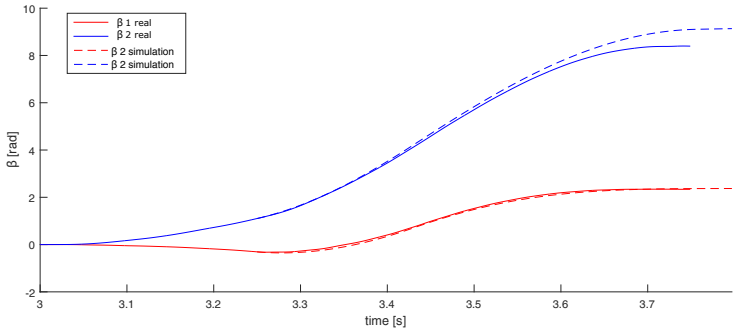

Figure 7.17: Angular position

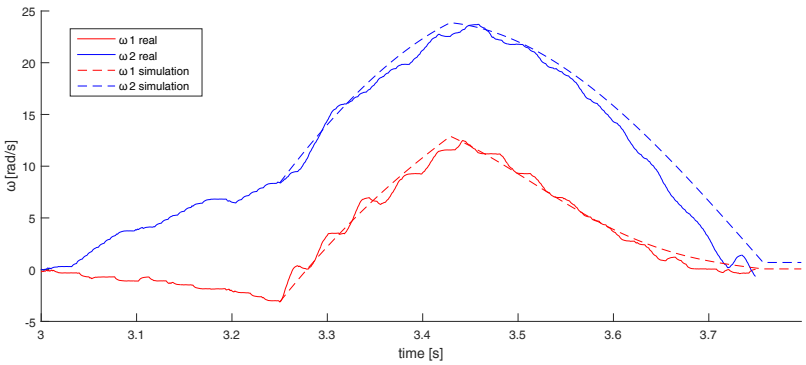

Figure 7.18: Angular velocity

The corresponding Cartesian velocity and position of the end effector are shown in Fig.7.19 and Fig.7.20, respectively. These values are obtained by β and $\dot{\beta}$ by exploiting the direct kinematics.

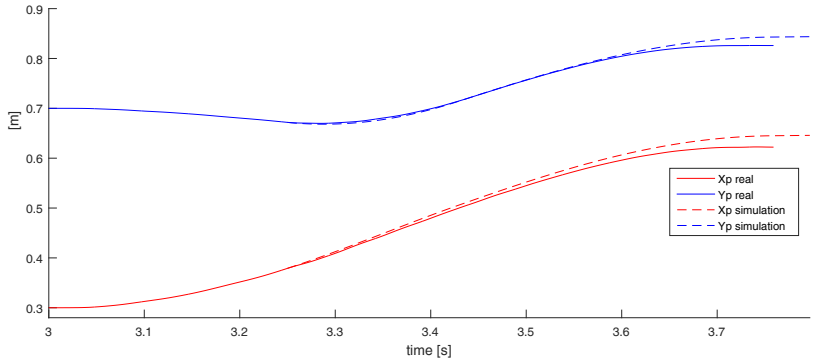

Figure 7.19: End effector position

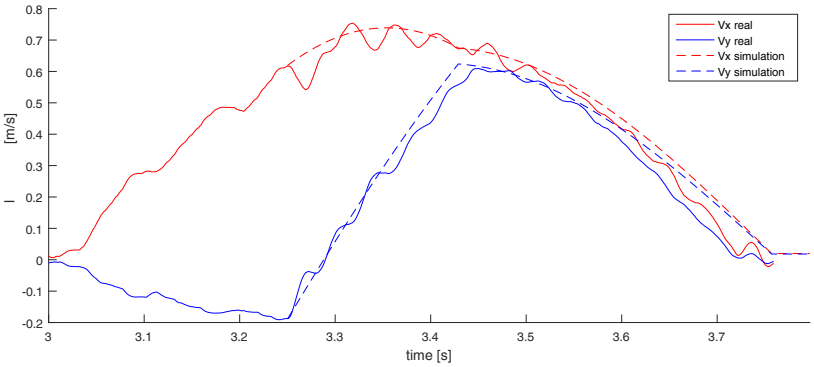

Figure 7.20: End Effector velocity

The position of the end effector and the difference between the simulation and the real test are shown also in Fig.7.21 in the Cartesian plane.

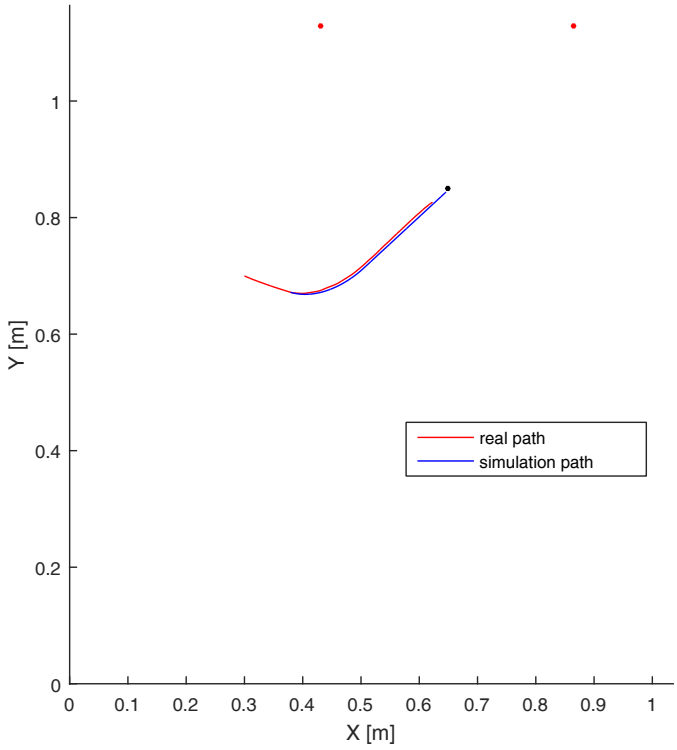

Figure 7.21: Comparison between real path and predicted path

Fig.7.22 represents the torque of the two motors, again in dashed line the simulated one and in continuous lines the real ones.

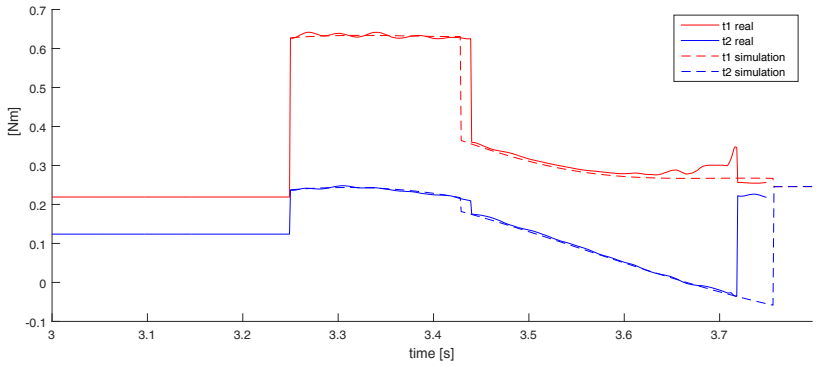

Figure 7.22: Motor Torques

It is worth noticing that the objective of the experiment in this case is not to follow the simulated or predicted trajectory, since the algorithm computes at each iteration the tensions (and hence the torques) that each cable must exert to obtain the desired result.

The cable tensions and the applied force are depicted in Fig.7.23 and Fig.7.24 respectively. It is possible to notice that the predicted

tension and the actual one are comparable, proving the accuracy of the model.

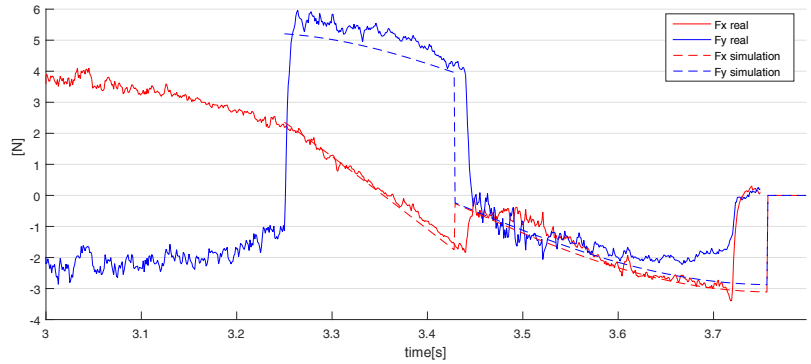

Figure 7.23: Forces exerted on the end effector

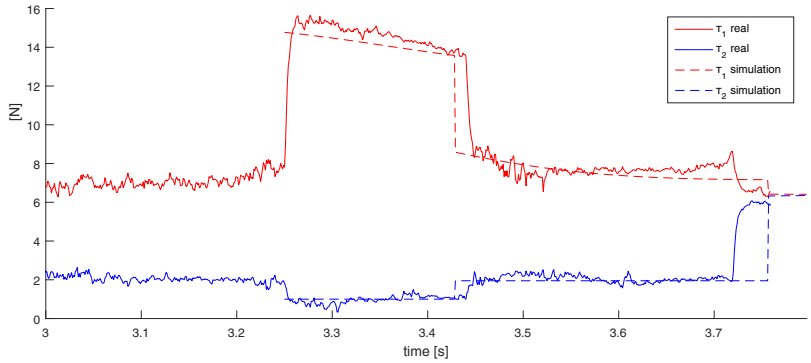

Figure 7.24: Cable Tensions

The velocity of the end effector in the rotated reference frame *d-o* is depicted in Fig.7.25. Here, it is possible to notice how the undesired velocity component is reduced to a suitable small value during the Connecting path while the residual velocity component is reduced during the second part of the strategy.

The exerted force is also depicted in blue arrows in Fig.7.26 along the path of the end effector. It is easy to recognize the 3 phases of motion: the beginning, when the recovery algorithm is not working yet and the force is directed along the motion; the first phase where the connecting path is performed and the exerted force is the one able to change the direction of motion of the end effector. Finally, when the velocity is directed towards the safe point, the second part of the strategy begins. In the beginning the end effectors still lies outside the residual workspace and it is not possible to generate a braking force. Hence, the exerted force is the one in the direction of the safe point causing a minimum acceleration on the end effector. Once the end effector enters the residual workspace, the algorithm computes the force able to decelerate the motion and finally stop the end effector.

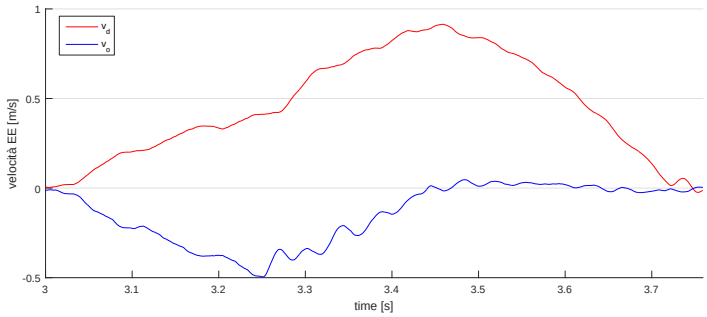

Figure 7.25: Velocity components in the rotated reference frame

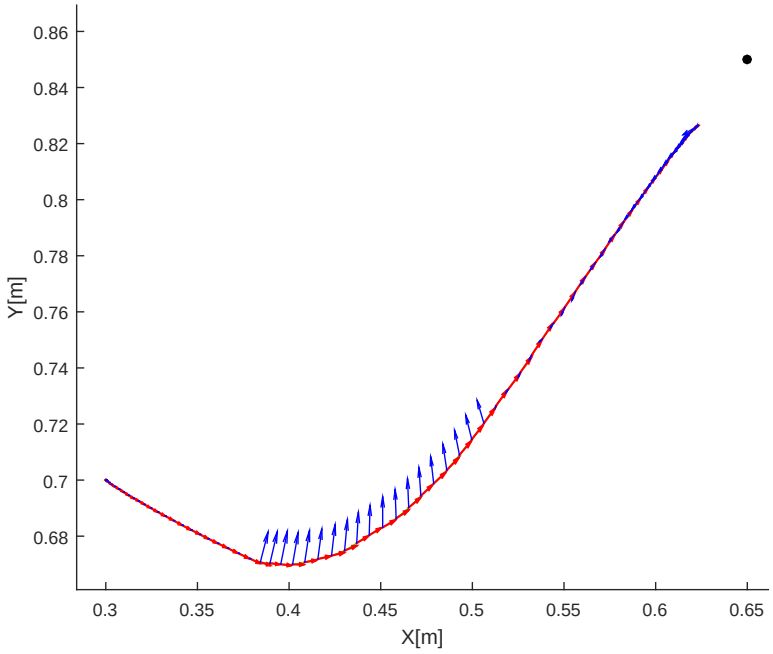

Figure 7.26: Path followed by the end effector

7.2 EXPERIMENTAL RESULTS: PERIODIC TRAJECTORY

This Section provides some experimental results to prove the effectiveness of the periodic trajectories based approach.

The strategy imposes to set a maximum height that the end effector can reach in order to ensure the possibility of setting a maximum cable tension limit. The experimental set up uses cables with a nominal maximum resistance of 39 kg.

In real applications, e.g. cable suspended camera systems, cables can withstand more than 10x the force occurring during normal operation. In our case study, cable tensions stay below 20N (maximum cable tension during normal operations). Hence, the maximum cable tension has been set equal to 200N, more than 10x the force required during normal operation and compatible with the given maximum resistance of the used cables.

We chose to set $\cos \beta_{max} = \frac{2mg}{\tau_{max}}$, which lead to a maximum height of $y_{max} = -0.09m$.

As for the linear approach, the strategy has been tested in four different failure scenarios to prove its effectiveness. The cable breaks at instant $t = 3s$ and after a short delay the strategy computes the trajectory to follow in order to stop the end effector in a safe landing location. Such location is computed taking into account the constraints given in Section 6.3 to guarantee positive and bounded cable tensions and avoid collisions with the fixed structure.

For each test, the trajectory followed by the end effector is here reported in Fig.7.27, 7.28, Fig.7.29 and Fig.7.30. The blue dot represents the chosen landing location while the red diamond represents the position at which the recovery approach intervenes. The two red dots at the top of the workspace represent the attachment points of the two active cables.

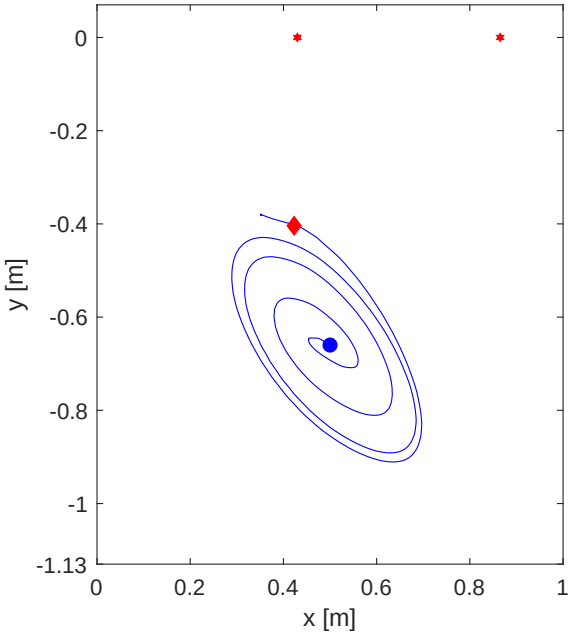

Figure 7.27: End effector path: test E

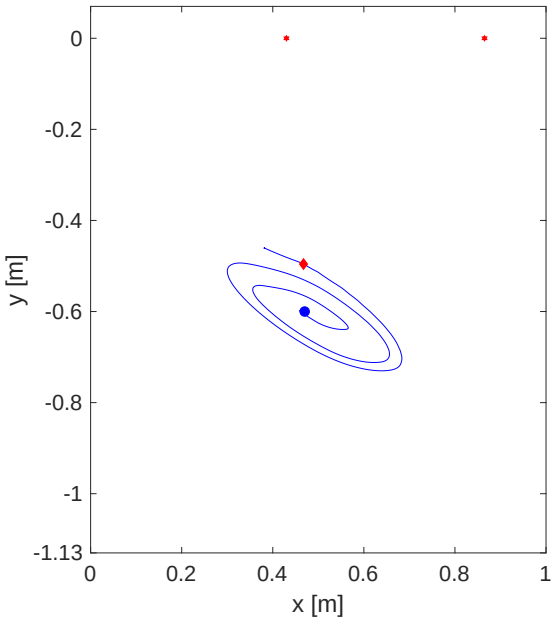

Figure 7.28: End effector path: test F

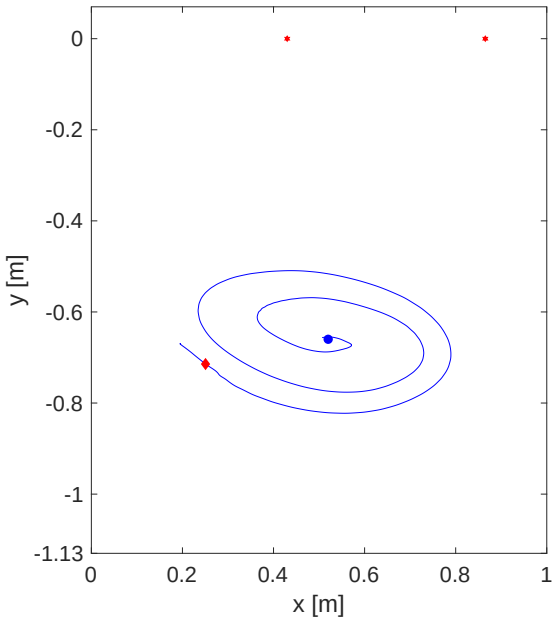

Figure 7.29: End effector path: test G

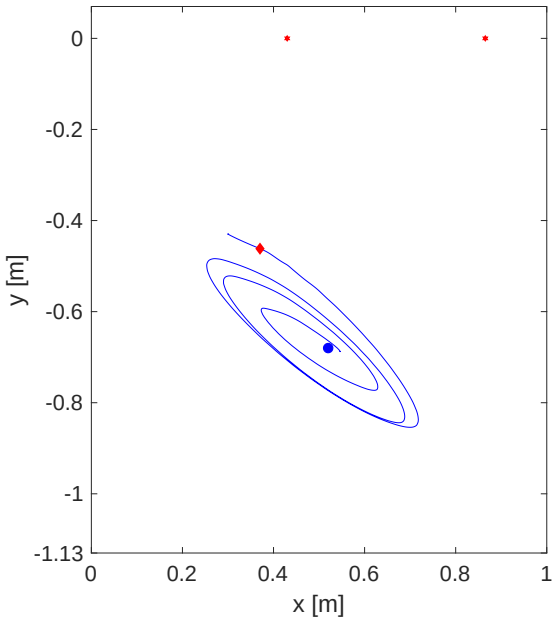

Figure 7.30: End effector path: test H

The corresponding tension configurations are plotted in Fig.7.31, Fig.7.32, Fig.7.33 and Fig.7.34. It can be noticed that in each test the tensions in the active cables are mantained positive and bounded, far below the maximum limit of 200N and under the normal functioning limit of 20N.

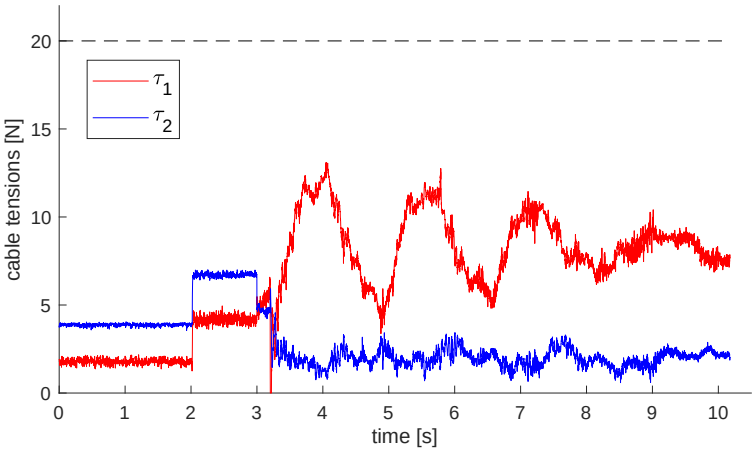

Figure 7.31: Cable tensions: test E

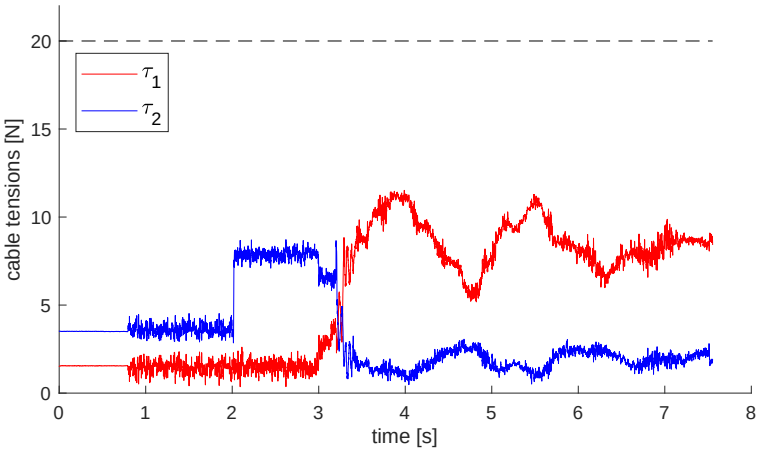

Figure 7.32: Cable tensions: test F

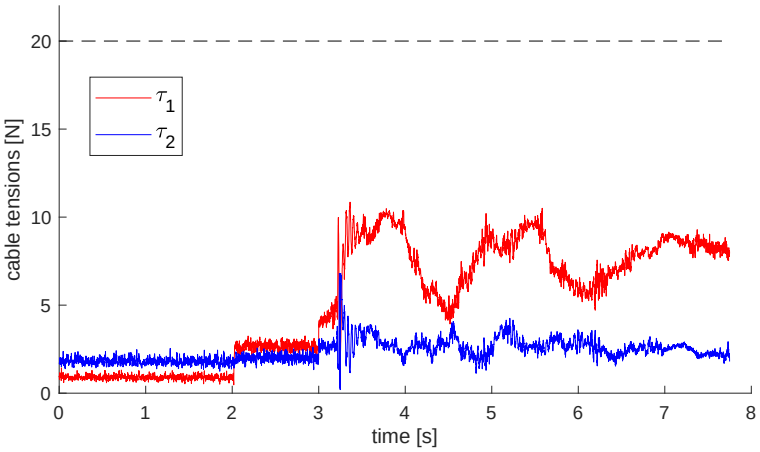

Figure 7.33: Cable tensions: test G

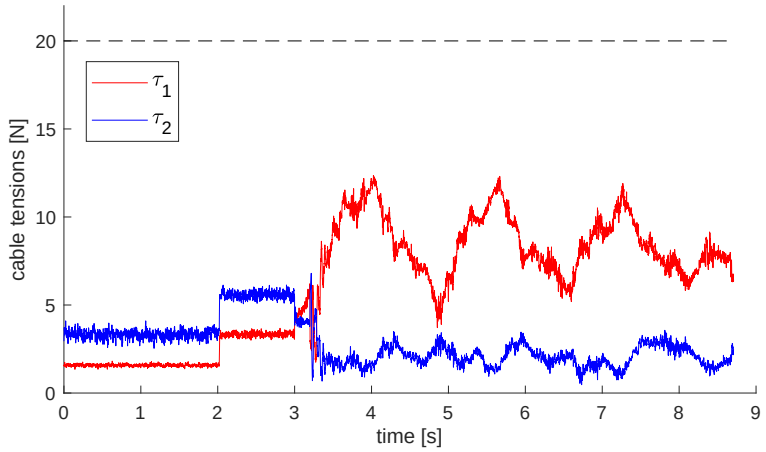

Figure 7.34: Cable tensions: test H

As for the linear approach, only one case is deeply analyzed in detail, which correspond to case F. Such test has the same starting point of Case A, so it will be possible to compare the results of the two strategies starting from the same failure scenario.

The motor angular position and velocity are plotted in Fig.7.35 and Fig.7.36 respectively.

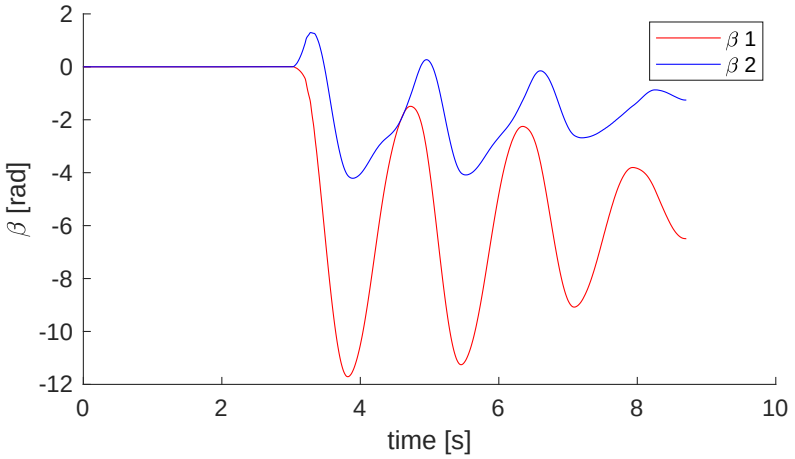

Figure 7.35: Angular position

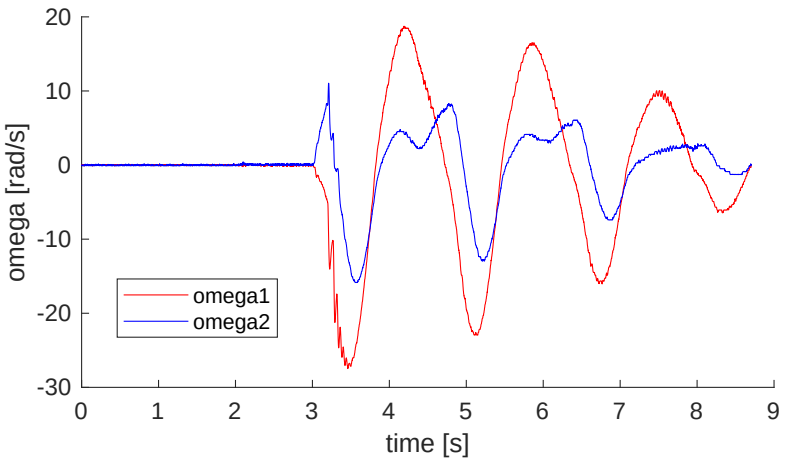

Figure 7.36: Angular velocity

The corresponding end effector position and velocity are plotted in Fig.7.37 and Fig.7.38 respectively. It can be noticed that the velocity is gradually reduced until zero following a periodic law.

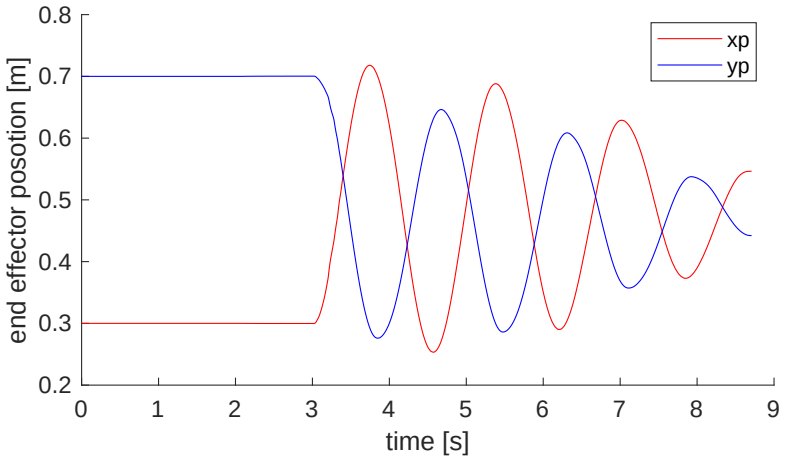

Figure 7.37: End Effector position

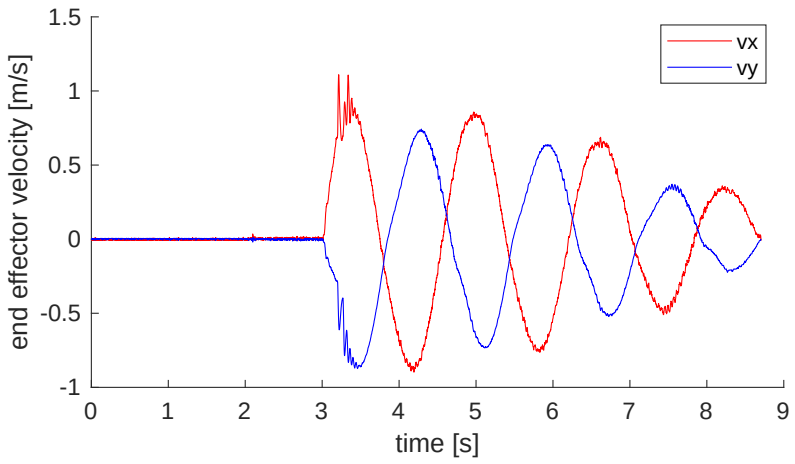

Figure 7.38: End Effector velocity

Finally, the motor torques corresponding to the tension configuration in Fig.7.34 are depicted in Fig.7.39.

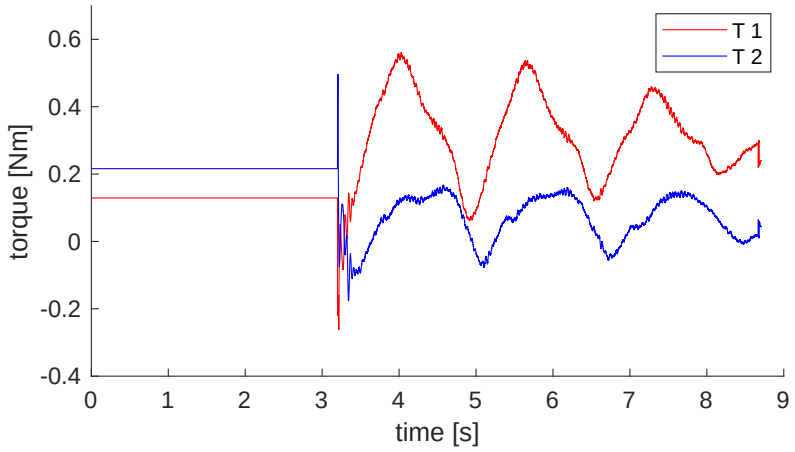

Figure 7.39: Motor Torques

7.3 FINAL REMARKS

It can be noticed how both strategies are effective when considering the requirement of keeping positive and bounded cable tensions during the whole trajectory.

With a deeper focus on test A and test F (having the same initial condition), it can be noticed that the periodic trajectory approach requires a significantly longer time to perform the task. Indeed, all the examples given for the linear trajectory approach take less than 1s from the moment at which the failure is detected to the moment at which the end effector reaches a steady position. The periodic trajectory takes around 9s to actually reach the safe landing location. However, the second strategy guarantees full control on the trajectory,

ensuring a collision-free path. Indeed, the second approach generates an actual path to follow while the first approach generates a tension configuration aimed at exerting a braking force. Moreover, generating the maximum braking force leads to more extreme cable tensions, close to acceptable limits, and more rough changes between such values. On the other hand, the periodic approach (excluding a slight disturbance in the failure instant), guarantees a smoother tension profile, reducing the risk of instability.

To conclude, both strategies represent an effective approach to maintain control over the end effector after failure and make it reach a safe landing position. Pros and cons are present in each strategy and could be further investigated in future works. The suitability of each strategy depends also on the studied application and on the desired after failure performance.

8

CONCLUSIONS

The main contribution of this thesis consists in providing a novel approach for managing failure in cable driven robots. Nowadays, cable driven robots are widely involved in the broadcasting field and for rehabilitation/home assistance, as discussed in Chapter 1. However, even if they work close to or even in contact with humans, an efficient emergency stop is not yet available. In this work, thanks to a deep understanding of cable robot performance before and after failure, two different strategies to apply in case of emergency are proposed.

In order to obtain feasible and efficient after failure motion, it is essential to study the performance of the manipulator and in particular how its force exertion capability is afflicted due to a cable breakage. The performance evaluation for cable driven robots has been presented in Chapter 3. In particular, a local performance index called *WEC* (Wrench Exertion Capability) has been investigated. Indeed, the *WEC* allows computing the maximum exertable force in a desired direction of interest while keeping null all the other wrench components. This information can be directly translated in dynamic constraints to plan a feasible motion along a specific direction. In order to be bale to exploit such index on-line, immediately after failure, a new geometry based method to compute the *WEC* has been proposed. The new algorithm takes advantage of the polytope description of the available wrench set and it is highly preferable to the linear programming approach initially proposed. Indeed, the new method is deterministic and non-iterative which makes it suitable for real-time applications.

The idea of exploiting the *WEC* index to plan after failure feasible trajectories is described in Chapter 4. Indeed, the objective after failure is to lead the end effector towards a safe configuration in a time that should be kept to a minimum. The easiest and shortest path would be a straight line from the position at which failure takes place towards the chosen safe configuration (referred as safe point in this work). The *WEC* index can be used at this stage to immediately appraise the residual force exertion capability and plan a feasible linear trajectory ending in the safe point. A connecting path is often necessary to change the direction of motion of the end effector to align its velocity with the desired direction of interest.

A second approach is presented in Chapter 5. This strategy takes advantage of recent works on dynamically feasible periodic trajectories. Such trajectories are ensured to be feasible for any amplitude if a particular frequency is chosen. Starting from this result, the proposed

trajectory is planned to ensure positive and bounded cable tensions and to avoid collisions with the physical boundaries of the workspace during the recovery path. This approach focuses in particular on cable suspended camera systems since they represent the most common application of cable driven robots. However, the strategy can be applied to different designs provided that the configuration after failure is fully constrained. This approach usually needs more time than the linear trajectory one but ensures a better control on the actual path tracked by the end effector after failure.

Both strategies have been adapted and tested on a prototype having 3 cables and 2 degrees of freedom. The description and optimization of the recovery approaches for the considered case study are provided in Chapter 6 where the fully actuated after failure configuration is analyzed. Experimental results are given in Chapter 7 to prove the effectiveness of the proposed strategies and to appraise the pros and cons of the two approaches.

The studies on safety for cable driven robots are far from being over. The need for an emergency stop is essential in order to spread the usage of these interesting and promising devices in many other fields, including industries. Future works will focus on further testing the proposed recovery strategies to different configurations and improve the computational efficiency of the involved algorithms. Nonetheless, new perspectives can still be discovered and investigated since different configurations might take advantage from different emergency strategies depending on the desired after failure performance.

BIBLIOGRAPHY

[1] Saeed Abdolshah, Damiano Zanotto, Giulio Rosati, and Sunil K Agrawal. "Optimizing stiffness and dexterity of planar adaptive cable-driven parallel robots." In: *Journal of Mechanisms and Robotics* 9.3 (2017), p. 031004.

[2] Saeed Abdolshah, Damiano Zanotto, Giulio Rosati, and Sunil Agrawal. "Performance evaluation of a new design of cable-suspended camera system." In: *Robotics and Automation (ICRA), 2017 IEEE International Conference on*. IEEE. 2017, pp. 3728–3733.

[3] James Albus, Roger Bostelman, and Nicholas Dagalakis. "The NIST robocrane." In: *Journal of Field Robotics* 10.5 (1993), pp. 709–724.

[4] L Barbazza, F Oscari, S Minto, and G Rosati. "Trajectory planning of a suspended cable driven parallel robot with reconfigurable end effector." In: *Robotics and Computer-Integrated Manufacturing* 48 (2017), pp. 1–11.

[5] C Bradford Barber, David P Dobkin, and Hannu Huhdanpaa. "The quickhull algorithm for convex hulls." In: *ACM Transactions on Mathematical Software (TOMS)* 22.4 (1996), pp. 469–483.

[6] Guillaume Barrette and Clément M Gosselin. "Determination of the dynamic workspace of cable-driven planar parallel mechanisms." In: *Journal of mechanical design* 127.2 (2005), pp. 242–248.

[7] Saeed Behzadipour and Amir Khajepour. "Time-optimal trajectory planning in cable-based manipulators." In: *IEEE Transactions on Robotics* 22.3 (2006), pp. 559–563.

[8] Alessandro Berti, Marc Gouttefarde, and Marco Carricato. "Dynamic recovery of cable-suspended parallel robots after a cable failure." In: *Advances in Robot Kinematics 2016*. Springer, 2018, pp. 331–339.

[9] Alessandro Berti, Jean-Pierre Merlet, and Marco Carricato. "Solving the direct geometrico-static problem of 3-3 cable-driven parallel robots by interval analysis: Preliminary results." In: *Cable-Driven Parallel Robots*. Springer, 2013, pp. 251–268.

[10] Per Henrik Borgstrom, Brett L Jordan, Gaurav S Sukhatme, Maxim A Batalin, and William J Kaiser. "Rapid computation of optimally safe tension distributions for parallel cable-driven robots." In: *IEEE Transactions on Robotics* 25.6 (2009), pp. 1271–1281.

[11] Paolo Boscariol, Alessandro Gasparetto, and Renato Vidoni. "Planning continuous-jerk trajectories for industrial manipulators." In: *ASME 2012 11th Biennial Conference on Engineering Systems Design and Analysis*. American Society of Mechanical Engineers. 2012, pp. 127–136.

[12] Giovanni Boschetti, Chiara Passarini, and Alberto Trevisani. "A Strategy for Moving Cable Driven Robots Safely in Case of Cable Failure." In: *Advances in Italian Mechanism Science*. Springer, 2017, pp. 203–211.

[13] Giovanni Boschetti and Alberto Trevisani. "Performance evaluation for cable direct driven robot." In: *ASME 2014 12th Biennial Conference on Engineering Systems Design and Analysis*. American Society of Mechanical Engineers. 2014, V003T17A014–V003T17A014.

[14] Giovanni Boschetti and Alberto Trevisani. "On the use of the wrench exertion capability as a performance index for cable driver robot." In: *Proceedings of ECCOMAS thematic conference on multibody dynamics*. 2015, pp. 375–384.

[15] Giovanni Boschetti and Alberto Trevisani. "Cable Robot Performance Evaluation by Wrench Exertion Capability." In: *Robotics* 7.15 (2018): *Kinematics and Robot Design*.

[16] Paul Bosscher and Imme Ebert-Uphoff. "Wrench-based analysis of cable-driven robots." In: *Robotics and Automation, 2004. Proceedings. ICRA'04. 2004 IEEE International Conference on*. Vol. 5. IEEE. 2004, pp. 4950–4955.

[17] Paul Bosscher, Andrew T Riechel, and Imme Ebert-Uphoff. "Wrench-feasible workspace generation for cable-driven robots." In: *IEEE Transactions on Robotics* 22.5 (2006), pp. 890–902.

[18] Samuel Bouchard, Clément Gosselin, and Brian Moore. "On the Ability of a Cable-Driven Robot to Generate a Prescribed Set of Wrenches." In: *Journal of Mechanisms and Robotics* 2 (2010), p. 011010.

[19] Marco Carricato and Jean-Pierre Merlet. "Stability analysis of underconstrained cable-driven parallel robots." In: *IEEE Transactions on Robotics* 29.1 (2013), pp. 288–296.

[20] Jean-François Collard and Philippe Cardou. "Computing the lowest equilibrium pose of a cable-suspended rigid body." In: *Optimization and Engineering* 14.3 (2013), pp. 457–476.

[21] Lawrence L Cone. "Skycam-an aerial robotic camera system." In: *Byte* 10.10 (1985), p. 122.

[22] Xiaowei Dai, Yuru Zhang, Dangxiao Wang, and Jian Song. "Structural Characteristics of Force/Moment Polytopes of Cable Driven Parallel Mechanisms." In: *Advances in Reconfigurable Mechanisms and Robots II*. Springer, 2016, pp. 1482–1493.

[23] Pascal Dion-Gauvin and Clément Gosselin. "Trajectory planning for the static to dynamic transition of point-mass cable-suspended parallel mechanisms." In: *Mechanism and Machine Theory* 113 (2017), pp. 158–178.

[24] Claudio Fanin, Paolo Gallina, Aldo Rossi, Umberto Zanatta, and Stefano Masiero. "Nerebot: a wire-based robot for neurorehabilitation." In: *ICORR'03*. HWRS-ERC. 2003, pp. 23–27.

[25] Flavio Firmani, Alp Zibil, Scott B Nokleby, and Ron P Podhorodeski. "Wrench capabilities of planar parallel manipulators. Part I: Wrench polytopes and performance indices." In: *Robotica* 26.06 (2008), pp. 791–802.

[26] Flavio Firmani, Alp Zibil, Scott B Nokleby, and Ron P Podhorodeski. "Wrench capabilities of planar parallel manipulators. Part II: Redundancy and wrench workspace analysis." In: *Robotica* 26.06 (2008), pp. 803–815.

[27] Paolo Gallina and Giulio Rosati. "Manipulability of a planar wire driven haptic device." In: *Mechanism and Machine Theory* 37.2 (2002), pp. 215–228.

[28] Asim Ghaffar and Mahir Hassan. "Failure Analysis of Cable Based Parallel Manipulators." In: *Applied Mechanics & Materials* 736 (2014).

[29] Clément Gosselin. "Global planning of dynamically feasible trajectories for three-DOF spatial cable-suspended parallel robots." In: *Cable-Driven Parallel Robots*. Springer, 2013, pp. 3–22.

[30] Clement Gosselin and Simon Foucault. "Dynamic point-to-point trajectory planning of a two-DOF cable-suspended parallel robot." In: *IEEE Transactions on Robotics* 30.3 (2014), pp. 728–736.

[31] Clément Gosselin, Ping Ren, and Simon Foucault. "Dynamic trajectory planning of a two-DOF cable-suspended parallel robot." In: *Robotics and Automation (ICRA), 2012 IEEE International Conference on*. IEEE. 2012, pp. 1476–1481.

[32] Marc Gouttefarde and Clément M Gosselin. "Analysis of the wrench-closure workspace of planar parallel cable-driven mechanisms." In: *IEEE Transactions on Robotics* 22.3 (2006), pp. 434–445.

[33] Branko Grünbaum. *Convex polytopes, volume 221 of Graduate Texts in Mathematics*. 2003.

[34] Carl S Holland and David J Cannon. *Cable array robot for material handling*. US Patent 6,826,452. 2004.

[35] Qimi Jiang and Vijay Kumar. "The direct kinematics of objects suspended from cables." In: *ASME 2010 international design engineering technical conferences and computers and information in engineering conference*. American Society of Mechanical Engineers. 2010, pp. 193–202.

[36] Xiaoling Jiang and Clément Gosselin. "Dynamically feasible trajectories for three-DOF planar cable-suspended parallel robots." In: *ASME Paper No. DETC2014-34419* (2014).

[37] Xiaoling Jiang and Clément Gosselin. "Dynamic point-to-point trajectory planning of a three-DOF cable-suspended parallel robot." In: *IEEE Transactions on Robotics* 32.6 (2016), pp. 1550–1557.

[38] Xin Jin, Xiang Cui, and Sunil K Agrawal. "Design of a cable-driven active leg exoskeleton (c-alex) and gait training experiments with human subjects." In: *Robotics and Automation (ICRA), 2015 IEEE International Conference on*. IEEE. 2015, pp. 5578–5583.

[39] Johann Lamaury and Marc Gouttefarde. "A tension distribution method with improved computational efficiency." In: *Cable-driven parallel robots*. Springer, 2013, pp. 71–85.

[40] Jhon Freddy Rodríguez León, Giuseppe Carbone, Daniele Cafolla, Matteo Russo, Marco Ceccarelli, and Eduardo Castillo Castañeda. "Experiences and Design of a Cable-Driven Assisting Device for Arm Motion." In: *ROMANSY 22–Robot Design, Dynamics and Control*. Springer, 2019, pp. 94–101.

[41] Wen Bin Lim, Guilin Yang, Song Huat Yeo, and Shabbir Kurbanhusen Mustafa. "A generic force-closure analysis algorithm for cable-driven parallel manipulators." In: *Mechanism and Machine Theory* 46.9 (2011), pp. 1265–1275.

[42] Lars Mikelsons, Tobias Bruckmann, Manfred Hiller, and Dieter Schramm. "A real-time capable force calculation algorithm for redundant tendon-based parallel manipulators." In: *Robotics and Automation, 2008. ICRA 2008. IEEE International Conference on*. IEEE. 2008, pp. 3869–3874.

[43] Giovanni Mottola, Clement Gosselin, and Marco Carricato. "Dynamically Feasible Periodic Trajectories for Generic Spatial 3-DOF Cable-Suspended Parallel Robots." In: *Journal of Mechanisms and Robotics* (). In press.

[44] Giovanni Mottola, Clément Gosselin, and Marco Carricato. "Dynamically-Feasible Elliptical Trajectories for Fully Constrained 3- DOF Cable-Suspended Parallel Robots." In: *Cable-Driven Parallel Robots*. Springer, 2018, pp. 219–230.

[45] Rendong Nan. "Five hundred meter aperture spherical radio telescope (FAST)." In: *Science in China series G* 49.2 (2006), pp. 129–148.

[46] Scott B Nokleby, R Fisher, Ron P Podhorodeski, and Flavio Firmani. "Force capabilities of redundantly-actuated parallel manipulators." In: *Mechanism and machine theory* 40.5 (2005), pp. 578–599.

[47] Leila Notash. "Failure recovery for wrench capability of wire-actuated parallel manipulators." In: *Robotica* 30.6 (2012), pp. 941–950.

[48] Leila Notash. "Wrench recovery for wire-actuated parallel manipulators." In: *Proceedings of robot design, dynamics and control, Romansy* 19 (2013), pp. 201–208.

[49] So-Ryeok Oh and Sunil Kumar Agrawal. "Cable-suspended planar parallel robots with redundant cables: Controllers with positive cable tensions." In: *IEEE International Conference on Robotics and Automation*. Vol. 3. IEEE; 1999. 2003, pp. 3023–3028.

[50] Cong Bang Pham, Song Huat Yeo, Guilin Yang, and I-Ming Chen. "Workspace analysis of fully restrained cable-driven manipulators." In: *Robotics and Autonomous Systems* 57.9 (2009), pp. 901–912.

[51] Andreas Pott, Christian Meyer, and Alexander Verl. "Large-scale assembly of solar power plants with parallel cable robots." In: *Robotics (ISR), 2010 41st International Symposium on and 2010 6th German Conference on Robotics (ROBOTIK)*. VDE. 2010, pp. 1–6.

[52] Andreas Pott, Hendrik Mutherich, Werner Kraus, Valentin Schmidt, Philipp Miermeister, Thomas Dietz, and Alexander Verl. "Cable-driven parallel robots for industrial applications: The ipanema system family." In: *Robotics (ISR), 2013 44th International Symposium on*. IEEE. 2013, pp. 1–6.

[53] Jason Pusey, Abbas Fattah, Sunil Agrawal, and Elena Messina. "Design and workspace analysis of a 6–6 cable-suspended parallel robot." In: *Mechanism and machine theory* 39.7 (2004), pp. 761–778.

[54] Rodney G Roberts, Todd Graham, and Thomas Lippitt. "On the inverse kinematics, statics, and fault tolerance of cable-suspended robots." In: *Journal of Field Robotics* 15.10 (1998), pp. 581–597.

[55] G Rosati, Paolo Gallina, A Rossi, and S Masiero. "Wire-based robots for upper-limb rehabilitation." In: *International Journal of Assistive Robotics and Mechatronics* 7 (2006), pp. 3–10.

[56] Giulio Rosati and Damiano Zanotto. "A novel perspective in the design of cable-driven systems." In: *ASME 2008 International Mechanical Engineering Congress and Exposition*. American Society of Mechanical Engineers. 2008, pp. 617–625.

[57] Giulio Rosati, Damiano Zanotto, and Sunil K Agrawal. "On the design of adaptive cable-driven systems." In: *Journal of mechanisms and robotics* 3.2 (2011), p. 021004.

[58] Giulio Rosati, Paolo Gallina, Stefano Masiero, and Aldo Rossi. "Design of a new 5 dof wire-based robot for rehabilitation." In: *Rehabilitation Robotics, 2005. ICORR 2005. 9th International Conference on*. IEEE. 2005, pp. 430–433.

[59] Giulio Rosati, Riccardo Secoli, Damiano Zanotto, Aldo Rossi, and Giovanni Boschetti. "Planar robotic systems for upper-limb post-stroke rehabilitation." In: *ASME 2008 International Mechanical Engineering Congress and Exposition*. American Society of Mechanical Engineers. 2008, pp. 115–124.

[60] Giulio Rosati, Stefano Cenci, Giovanni Boschetti, Damiano Zanotto, and Stefano Masiero. "Design of a single-dof active hand orthosis for neurorehabilitation." In: *Rehabilitation Robotics, 2009. ICORR 2009. IEEE International Conference on*. IEEE. 2009, pp. 161–166.

[61] L Stocco, Septimiu E Salcudean, and Farrokh Sassani. "Mechanism design for global isotropy with applications to haptic interfaces." In: *ASME Symposium on Haptic Interfaces for Virtual Environment and Teleoperator Systems, Dallas, TX, Nov*. 1997, pp. 15–21.

[62] Alberto Trevisani. "Underconstrained planar cable-direct-driven robots: A trajectory planning method ensuring positive and bounded cable tensions." In: *Mechatronics* 20.1 (2010), pp. 113–127.

[63] Alberto Trevisani. "Planning of dynamically feasible trajectories for translational, planar, and underconstrained cable-driven robots." In: *Journal of Systems Science and Complexity* 26.5 (2013), pp. 695–717.

[64] Alberto Trevisani, Paolo Gallina, and Robert L Williams. "Cable-direct-driven robot (CDDR) with passive SCARA support: theory and simulation." In: *Journal of Intelligent and Robotic Systems* 46.1 (2006), pp. 73–94.

[65] Vineet Vashista, SK Mustafa, and Sunil K Agrawal. "Experimental studies on the human gait using a tethered pelvic assist device (t-pad)." In: *Rehabilitation Robotics (ICORR), 2011 IEEE International Conference on*. IEEE. 2011, pp. 1–6.

[66] Robert L Williams Ii and Paolo Gallina. "Translational planar cable-direct-driven robots." In: *Journal of Intelligent and Robotic systems* 37.1 (2003), pp. 69–96.

[67] Tsuneo Yoshikawa. "Manipulability of robotic mechanisms." In: *The international journal of Robotics Research* 4.2 (1985), pp. 3–9.

[68] Damiano Zanotto, Giulio Rosati, Simone Minto, and Aldo Rossi. "Sophia-3: a semiadaptive cable-driven rehabilitation device with a tilting working plane." In: *IEEE Transactions on Robotics* 30.4 (2014), pp. 974–979.

[69] Alp Zibil, Flavio Firmani, Scott B Nokleby, and Ron P Podhorodeski. "An explicit method for determining the force-moment capabilities of redundantly actuated planar parallel manipulators." In: *Journal of mechanical design* 129.10 (2007), pp. 1046–1055.

PUBLICATIONS

Some ideas and figures have appeared previously in the following publications:

[1] Boschetti, G., Passarini, C., & Trevisani, A. (2017). A recovery strategy for cable driven robots in case of cable failure. *International Journal of Mechanics and Control* 18, 41-48.

[2] Boscariol, P., Boschetti, G., Gallina, P., & Passarini, C. (2017). Spring Design for Motor Torque Reduction in Articulated Mechanisms. *International Conference on Robotics in Alpe-Adria Danube Region*, pp. 557-564. Springer, Cham.

[3] Boschetti, G., Passarini, C., & Trevisani, A. (2017). A strategy for moving cable driven robots safely in case of cable failure. *Advances in Italian Mechanism Science*, pp. 203-211. Springer, Cham.

[4] Boschetti, G., Passarini, C., Trevisani, A., & Zanotto, D. (2018). A Fast Algorithm for Wrench Exertion Capability Computation. *Cable-Driven Parallel Robots*, pp. 292-303. Springer, Cham.

[5] Boschetti, G., Carbone, G., & Passarini, C. (2018). A Fail-Safe Operation Strategy for LAWEX (LARM Wire Driven EXercising Device).*IFToMM Symposium on Mechanism Design for Robotics*, pp. 424-431. Springer, Cham.

[6] Boschetti, G., Passarini, C., & Trevisani, A. (2018). A Recovery Approach for Spatial Cable Robots After Cable Failure. *The International Conference of IFToMM ITALY*, pp. 457-464. Springer, Cham.

[7] Passarini, C., Zanotto, D., & Boschetti, G. (2018). Dynamic Trajectory Planning for Failure Recovery in Cable-Suspended Camera Systems. *International Journal of Mechanisms and Robotics*, Advance online publication doi:10.1115/1.4041942

RINGRAZIAMENTI

Questi tre anni sono stati un'incredibile avventura e hanno rappresentato un percorso di crescita professionale e personale. Voglio ringraziare il mio surpervisore Prof. Giovanni Boschetti per aver creduto in me fin dall'inizio e per avermi dato questa incredibile opportunità. Senza il suo costante supporto questo lavoro non sarebbe stato possibile. Voglio inoltre ringraziare tutti i membri del gruppo di Meccanica Applicata del Dipartimento di Tecnica e Gestione dei Sistemi Industriali di Vicenza per i suggerimenti e l'aiuto ricevuto in questi anni.

Un grande ringraziamento va a tutti i miei amici, in Italia o all'estero. Grazie per l'amicizia che mi avete dimostrato a prescindere dalla distanza. Riempite ogni giorno la mia vita di allegria e risate. Un ringraziamento speciale va inoltre al mio fidanzato Anthony, per la costante pazienza, supporto ed affetto.

Infine, ma non per importantanza, vorrei ringraziare la mia famiglia ed in particolare i miei genitori. Siete stati e sarete sempre il mio costante punto di riferimento. Senza il vostro supporto non avrei mai iniziato questo percorso e non sarei qui ora a scrivere questa tesi. Grazie dal profondo del cuore per il vostro affetto.

ACKNOWLEDGMENTS

These past three years have been an incredible adventure with a mix of personal and professional growth. I want to thank my supervisor, Professor Giovanni Boschetti for this opportunity. He has trusted me and believed in me since the beginning. Without his support, this work, would not have been possible. I also want to thank all the members of the Applied Mechanics group at the department of Management and Engineering in Vicenza (Padova University) for all the helpful suggestions and support during these three years.

A big thanks goes also to all my friends, at home and abroad, for the emotional support, no matter if close or far. Thank you for filling my life with love and laughs. Especially my fiancée Anthony for his constant love, help and patience. I am looking forward to beginning this new chapter of my life and seeing where the future will take us.

Last but absolutely not least, I want to thank my family. They have been my constant point of reference and they have been there for me no matter what obstacles I faced through all my studies. They gave me the push I needed to undertake the PhD program. Without their help and support I would not be here writing this thesis. Thank you, from the bottom of my heart for everything.

Learning never exhausts the mind

— Leonardo da Vinci